New Insights into the Relation Between Coronal Mass Ejections and Nonthermal Radio Emissions

A Dissertation Submitted to

the Department of Physics

Addis Ababa University

In Partial Fulfillment of

the Requirement for the Attainment of the Degree of

Doctor of Philosophy in Physics

Tsega Berhane Teklu

Addis Ababa, Ethiopia

April, 2016

ADDIS ABABA UNIVERSITY

DEPARTMENT OF PHYSICS

The undersigned here by certify that they have read and recommend to the Faculty of Graduate Studies for acceptance a thesis entitled **"New Insights into the Relation between Coronal Mass Ejections and Nonthermal Radio Emissions"** by Tsega Berhane Teklu in partial fulfillment of the requirement of the requirement for the degree of Doctor of Philosophy.

Dated: April 2016

External Examinor: _____

Research Supervisors: _____

Dr. Natchimuthuk Gopalswamy

_____

Prof. Ashok Vasudeo Gholap

Examining Committee: _____

_____

_____

_____

ADDIS ABABA UNIVERSITY

Date: **April 2016**

Author: **Tsega Berhane Teklu**

Title: **New Insights into the Relation Between Coronal Mass Ejection and Nonthermal Radio Emissions**

Department: **Physics**

Degree: **Ph. D.** Convocation: **June** Year: **2016**

Permission is herewith granted to Addis Ababa University to circulate and to have copied for non-commercial purposes, at its discretion, the above title upon the request of individuals or institutions.

_____

Signature of Author

To

M. Arsema, F. Gabrial, M. Aregawi, M. Muleye and FB. Yemuney!

Acknowledgments

This thesis is the result of my long journey in receiving my Ph.D. Above all, I give special thanks to my Father, Son of God and St. Virgin Mary. As a creature of His own, His eyes are on me in good and bad times. I can see that carrying His cross is the best flavor of life I can experience in my daily life. He gave me the greatest lessons in life.

It is my great pleasure to express my gratitude to Dr. Nat Gopalswamy, my supervisor abroad, for suggesting the problems, guiding towards their solution, encouragement and the financial support in conducting the research. I can see why people say education is one and universal. He has been proving this to be the case. He is one of the most dedicated and friendly scientists in NASA Goddard Space Flight Center (GSFC). His leadership is also amazing. Colleagues and team members have special respect for him. I thank Prof. Gholap, my supervisor at home university, for all his help within the limited time he had in supporting my Ph.D. work at the Addis Ababa University (AAU). My sincere thanks are also due to Dr. P. Makela, Dr. S. Yashiro, Dr. S. Akiyama, Dr. N. Thakur and Dr. H. Xie from the Catholic University of America and NASA GSFC for their continuous help throughout my research work at NASA. I am also indebted to Dr. C. Kay for carefully reading a draft of this thesis.

I am grateful to the following individuals for their great support throughout this work: Dr. Alem M., Dr. Endawoke Y., Dr. Tilahun T., Prof. Singh, Prof. Chaubey, Dr. Mulugeta B., Dr. Fisseha , Prof. Masresha, Dr. Birhanu, Dr. Belayneh, Ms. Tsilat, Dr. Teshome S., Dr. Legesse W., Dr. Araya, Mr. Kassa, Ms. Kelem, Mr. Niqodimos, Dr. Brook, Ms. Almaz, Ms. Elisa, Dr. Wanda, Dr. Tilaye, Dr. Abebe, Dr. Kebede, Dr. Kideya, Dr. Hagos, Ms. Senait, Ms. Sara, Mr. Hagos, Ms. Meron, Ms. Selamawit and Mr. Temesgen.

I have never seen a woman scientist as great as Prof. Fetien in Ethiopia. She is one of my role models and I appreciate her moral support.

There are not enough words to describe the love and unconditional support from my mother Muleye. It is her strength and perseverance that brought me to this level despite the great loss in our personal life. I have seen heaven in Yemuney for all that he did for my development and his presence in my thoughts. My Hab Meaza and Rahel, I am grateful for having them in my life. It

gives me a great pleasure to thank them for being with me in good and bad times. I could not pass without mentioning Hiluf‟s spectacular advices he offered me. At this stage, I am so happy for Yirga‟s contribution in place of Yemuney especially to Muleye. Alik (Canaan) and Mesret beloved children of mine raise me up. They filled my gap. We climb the mountain all together hand to hand.

This wouldn‟t happen without Abba Araya‟s spectacular spiritual guidance next to God. I have seen God performing in him for me. Tiruye‟s support was unreplaceable. I thank Kesis Ayalneh and Debre Medhanit for the strengthening words and prayers. Bisrat, the best friend and special person I ever met in life, her love always shines my life. I thank Eden for all the sacrifices. I thank Tsige Berhane, Tsigereda and Arega for sharing my burden during the snow period. I am also grateful for having open hearted friend, Hadera.

I still extend my gratitude to Dr. Kidist, Genet, Dagmawit, Elisabeth, Abraham, Asfaw, Mekonen and Kinfe for stretching their hands whenever I am needy.

Abstract

Coronal Mass Ejections (CMEs) are the main space weather drivers. Studying CME kinematics and associated events is important to be able to make predications before a CME arrival and make proper arrangements. Type II bursts are signatures of energetic CMEs. By studying type II bursts, it is possible to probe the information on the associated CME remotely since they are electromagnetic waves, which arrive at Earth in ~ 8 minutes but the CME arrival time is not less than a day. In this research, we report on the complex type II radio burst of 2012 January 19 and its association with a CME. The dynamic spectrum shows a pair of type II bursts with fundamental – harmonic structures, one confined to decameter-hectometric (DH) and the other extending to kilometric (km) wavelengths. By comparing the CME and shock speeds, the coronal density obtained from white-light polarization brightness images with that inferred from the fundamental component of the type II burst, we show that the radio sources of the DH-km and the DH come from the region above the flank and near the nose of the shock, respectively. We report also on an unusual drifting feature in the radio dynamic spectrum at frequencies below 14 MHz that occurred on 2001 September 27 observed by the Radio and Plasma Waves (WAVES) experiment on board the Wind spacecraft. We call this feature a "Diffuse Interplanetary Radio Emission (DIRE)". It occurred in association with a regular type II burst. It is observed at higher frequency than the associated type II burst, with no harmonic relationship with the type II burst. We identified the source of the DIRE is the flank. Study on DIRE statistics showed DIREs have slightly larger drift rates than the regular type II bursts. Their onset is generally delayed from the onset of the regular type II bursts. DIREs are mostly associated with fast-halo and disk centered CMEs. Finally, we revisit the hierarchical relationship between the different wavelength ranges of the type II bursts from Wind/WAVES and the associated CME kinetic energy reported previously. We consider pure DH, m-DH and DH-km as separate groups, which are previously included under a single DH (DH: decameter-hectometric; m: metric; km: kilometric). We find that the kinetic energy of CMEs organizes the hierarchal relationship of type II bursts. Collectively, our results give a new way to look at nonthermal radio emission from CMEs, which can be used to improve predictions of CME travel in the interplanetary medium.

Contents

List of Figures

List of Tables

Acronyms

AIA	Atmospheric Imaging Assembly (on SDO)
ATM	Apollo Telescope Mount (on Skylab)
AU	Astronomical Unit
C2	Telescope 2 in Large Angle and Spectrometric Coronagraph (on SOHO)
C3	Telescope 3 in Large Angle and Spectrometric Coronagraph (on SOHO)
CDAW	Coordinated Data Analysis Workshop
CELIAS	Charge, Element, and Isotope Analysis System (on SOHO)
MTOF PM	Mass Time-of-Flight Proton Monitor (on SOHO)
CMD	Central Meridian Distance
CME	Coronal Mass Ejection
COR 1	Coronagraph 1 (on STEREO)
COR 2	Coronagraph 2 (on STEREO)
CULGOORA	A place in Australia where a ground-based radio telescope is located
D1 and D2	Dimming 1 and 2 in the flux rope cartoon
D	Decametric
DH	Decameter-Hectometric
DH-km	DH-kilometric wavelengths
DIRE	Diffuse Interplanetary Radio Emission
EIT	Extreme-ultraviolet Imaging Telescope (on SOHO)
EJ	Ejecta
EUV I	Extreme Ultraviolet Imager (on STEREO)
FOV	Field of View
FR	Flux Rope
GOES	Geostationary Operational Environmental Satellite
H	Hectometric
HI 1	Heliospheric Imager 1 (on STEREO)
HI 2	Heliospheric Imager 2 (on STEREO)

HiRAS	Hiraiso Radio Spectrograph
H-T	Height-Time
HXR	Hard X-rays
ICME	Interplanetary Coronal Mass Ejection
IP	Interplanetary
km	kilometric, kilometer
LASCO	Large Angle and Spectrometric Coronagraph (on SOHO)
LDB	Leblanc, Dulk and Bougeret (density model)
LE	Leading Edge
m	metric
m-DH	metric-DH
MC	Magnetic Cloud
MHD	Magnetohydrodynamic
NASA	National Aueronautics Space Administration
NOAA	National Oceanic and Atmospheric Administration
OSO-7	Seventh Orbiting Solar Observatory
PA	Position Angle
pB	Polarization Brightness
PCME	Primary Coronal Mass Ejection
PEA	Post-Eruption Arcade (flare arcade)
PIL	Polarity Inversion Line
R	Flare Ribbons
RAD1	Radio Receiver 1 (Radio and Plasma Wave Experiment on Wind)
RAD2	Radio Receiver 2 (Radio and Plasma Wave Experiment on Wind)
Rs	Solar radius
RSTN	Radio Solar Telescope Network
S/WAVES	STEREO‟s Radio and Plasma Wave Experiment
SDO	Solar Dynamic Observatory
SECCHI	Sun Earth Connection Coronal and Heliospheric Investigation
SEP	Solar Energetic Particle

SOHO	Solar and Heliospheric Observatory
MDI	Michelson Doppler Imager (on SOHO)
SSN	Sunspot Number
STEREO	Solar Terrestrial Relations Observatory
STEREO-A	STEREO Ahead
STEREO-B	STEREO Behind
SXR	Soft X-rays
SXT	Soft X-ray Telescope (on YOHKOH)
WAVES	Radio and Plasma Wave Experiment (on board Wind)
Wind	Short name for Comprehensive Solar wind Laboratory
YOHKOH	The name of a Japanese Satellite that observed the Sun in X-rays

Chapter 1

Introduction

In this chapter we introduce the basic concepts in solar physics, a short summary of the literature, and the rationale and objective of the research. We begin with the Sun, its structure, solar eruptions, and instrumentation. A brief description of the instruments used in this thesis is presented. A literature review on Coronal Mass Ejections (CMEs), Solar Radio Bursts, Solar flares, Solar Energetic Particle (SEP) events, and Solar activity cycle follows. Finally, the importance of the research undertaken is discussed.

1.1 Background

1.1.1 The Sun and its Structure

The Sun is a middle aged and sized star, our great laboratory for observing and testing many large-scale phenomena. The following summarizes some of the facts about the Sun extracted from Prialnik (2009), Foukal (2004) and Uwamahoro (2013 and references therein):

- Age = 4.6×10^9 years
- Mass = $(1.9889 \pm 0.0003) \times 10^{30}$ kg
- Radius = $(6.959 \pm 0.007) \times 10^8$ m (Solar Radius, Rs)
- Chemical composition = hydrogen (92.1%), helium (7.8%)
- Volume = 1.412×10^{27} m^3
- Luminosity = 3.86×10^{26} W
- Equatorial period of rotation ~ 27 days

The structure of the Sun can be broadly divided into two parts; the solar interior and the atmosphere. The interior consists of the core, radiation zone, and convective zone (see Figure

1.1). Its atmosphere comprises of the photosphere, chromosphere and corona. The solar atmosphere is mostly dominated by magnetic fields, which are produced in the solar interior at the base of the convection zone. Present work pertains to the solar corona where the energy is released in the form of flares and CMEs, although manifestations are found in other layers.

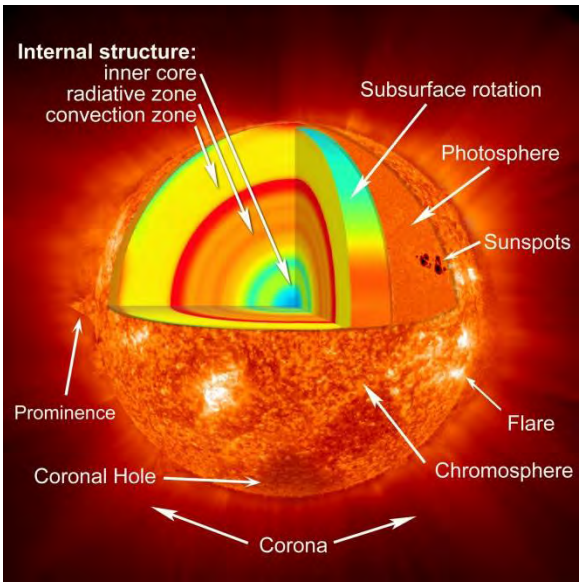

Figure 1.1. The different parts of the Sun. The internal structures (core, radiative and convective zone), solar atmosphere (photosphere, chromosphere and corona) and other structures (sunspots, coronal hole, flare and prominence) (http://sohowww.nascom.nasa.gov/data/summary/copyright.html).

Thermonuclear processes in the core are the main source of the energy in the Sun. The core extends up to 0.25 Rs and has a temperature and pressure of 1.5×10^7 K and $> 2.5 \times 10^{16}$ pascal (Pa), respectively. The radiative zone is part of the Sun, where energy transfer is dominated by radiative process. It extends from 0.25–0.70 Rs, where the temperature ranges from $(7–2) \times 10^6$ K. A transition zone, called the tachocline, exists between the radiative and convective zone above it. The tachocline is most likely the location where the solar magnetic field is created (Petrovay and Christensen 2010). The convective zone is the outer layer of the solar interior,

where energy is transferred outwards by convection and extends from 0.7–1 Rs. It is less dense than the core and the radiative zone, which allows the easy upward motion of the plasma and heat to the photosphere. The material cools at the photosphere and drops back to the upper edge of the radiative zone, which allows for the convective motion to continue. The photosphere is the visible surface layer of the Sun, because there the light is able to escape into space. The temperature of the photosphere ranges from 6400 to 4400 K. The thickness and the electron density of the photosphere are 500 km and 10^{19}–10^{21} m^{-3}, respectively. Different kinds of granulations, i.e., brighter regions separated by darker edges, are observed in the photosphere, which indicate the upward motion beneath the photosphere. Once the upward moving plasma flow reaches the photosphere, it moves horizontally, cools down and sinks back down at the edge of the granule. Typical granules may have the diameter of 1000 km with a lifetime of 5–10 minutes and thousands km s^{-1} of vertical velocities. There are also larger patterns of mesogranulation and supergranulation with diametrical size, lifetimes and speeds of 7000 km, hours, and tens of m s^{-1} and 3×10^4 km, days and 0.5 km s^{-1}, respectively. The photosphere rotates with a higher speed at the equator than at the polar region despite the rigid motion of the core and the radiative zone. The differential rotation in the convection zone twists the magnetic field lines into bundles that float upwards and emerge through the photosphere as areas of high magnetic field and cool plasma on the photosphere. Because of their cooler temperatures relative to the surrounding plasma, these areas are observed as dark regions on the photosphere and are called sunspots. Sunspots can have a size equal to the Earth and have a temperature of ~ 4000 K. They usually consist of regions of opposite magnetic polarities known as poles. Sunspots can reach magnetic field strengths of up to several Teslas. Energy stored in this magnetic field is ultimately responsible for the thermal energy in flares and kinetic energy in coronal mass ejections. Energy release can also take place in bipolar magnetic regions that do not have a spot.

The region immediately above the photosphere is the chromosphere. The separation of the photosphere and chromosphere is not clearly demarcated due to the constantly on-going up-flows, down-flows, heating, cooling and other dynamical processes in the solar atmosphere in

general. The temperature of the chromosphere ranges 4500–20,000 K. It covers a 2,000 km thick region and it has the density of 10^{16} m^{-3}. Jets with speeds of 30 km s^{-1} lasting for 5–10 minutes are observed in the chromosphere. Filaments are observed as dark features (channels) on the solar disk, while prominences are observed as bright features in the solar limb. Prominences are the same as filaments, but as seen above the limb from the side against the less dense (i.e., darker) solar atmosphere (corona), hence they appear bright. Prominences can erupt and leave the Sun. These are known as eruptive prominences. Prominences are the earliest form of mass ejections observed from the Sun since 19th century (Tandberg-Hanssen 1995).

The outer most structure of the solar atmosphere is the corona. It is tenuous (density ~ 10^{15} m^{-3} at the coronal base) and hot (temperature ~ 10^{6} K) with regions of variable electron densities and temperatures. The corona is structured by the magnetic field that permeates it. The corona can be detected in white light during total solar eclipses or by coronagraphs that artificially eclipse the much brighter solar disk. The corona can be divided into several regions called K-corona, F-corona, E-corona and T-corona. The K-corona is the region below 2 Rs, which is strongly dominated by polarized light due to Thomson scattering, i.e., photospheric light scattered off free electrons. Because of this, it is also called the true corona. The brightness of F-corona is composed of photospheric light Rayleigh-scattered from the dust particles and its continuous spectrum includes the Fraunhofer absorption lines. Therefore, it is called the false corona. The light of the E-corona contains emission lines from the visible to extreme ultraviolet due to various excited atoms and ions, quite unlike the sunlight scattered by the free electrons and the dusts in the former two coronal components. Some of the strongest emission lines are Fe $_{XIV}$ at 530.3 nm (visible), Hα at 656.3 nm (visible), and Lyman-α at 121.6 nm (UV). The T- corona is the thermal corona which is mainly due to the thermal emissions from the hot gas.

The solar temperature, density and ionization fall from the core to the chromosphere but then the temperature suddenly increases to millions of kelvin in the corona (see Figure 1.2). This sudden increase in temperature is known as the “Coronal Heating Problem”. The extension of the outer corona beyond ~3 Rs is called the interplanetary (IP) medium.

Background

Eclipse observations and solar radio emission provided early insight into the physical properties of the corona (see e.g., Newkirk 1967; Ginzburg and Zhelezniakov 1958). Different models have been developed to describe the general electron density profile in the corona (Leblanc et al. 1998; Saito et al. 1977; Dulk et al. 1998). The white light image of the corona can be inverted and the density of the corona can be measured either using the total or polarized brightness (Schuster 1870; Minnaert 1930; van de Hulst 1950; Billings 1966; Quémerais and Lamy 2002; Thernisien et al. 2006). The polarized light dominates in the inner corona. Coronagraph images are used for this purpose.

Some of the special features in the corona are active regions and coronal holes. Active regions are localized, transient volumes of the solar atmosphere that include plages, sunspots, faculae, flares, and CMEs originate. The sunspots are the photospheric signatures of active regions. Coronal holes are dark regions of the corona in extreme ultraviolet and soft X-ray images. They are regions of open magnetic fields from which the fast solar wind originates. The solar wind is the continuous flow of solar particles along the open magnetic field lines into the heliosphere. Solar wind extends all the way to the edge of the solar system. While the fast solar wind originates from coronal holes, the slow solar wind originates from the edges of coronal streamers and active regions (Cranmer 2009). The temperature of coronal holes, quiet sun region, and active region are 10^6, $(1–2) \times 10^6$ and $(2–6) \times 10^6$ K, respectively. Coronal streamers are quasi-stationary long-lived (up to months), large-scale structures observed during solar eclipses or using coronagraphs (Koutchmy and Livshits 1992). They have higher density and magnetic field than in the surrounding corona.

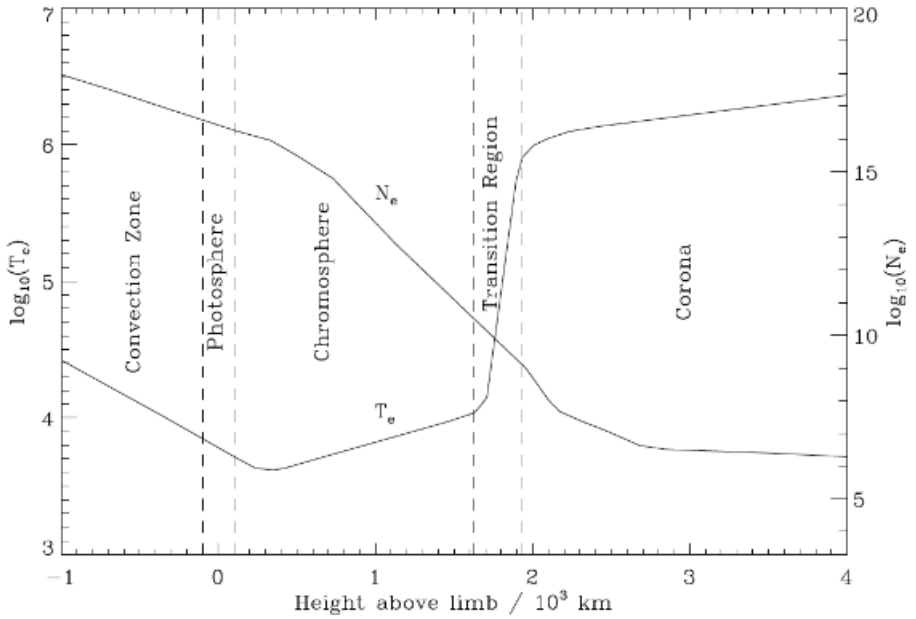

Figure 1.2. The combined plot of a one dimensional electron density and temperature profile from the convection zone to the corona. The density drops but the temperature first declines then it starts slowly growing followed by a sudden increase. Figure is from Gabriel and Mason (1982).

1.1.2 Solar Eruption

The term solar eruption refers to the sudden release of energy, in the form of flares and CMEs. The energy is stored in coronal magnetic fields and released due to some kind of a trigger, which is not fully understood. Figure 1.3 depicts the current understanding of the flare and CME eruption process (e.g., Gopalswamy 2010). It is based on the theory of flux rope formation during eruption (e.g. Longcope and Beveridge 2007). Figure 1.3 (a) shows the overall geometry of an eruption. Figure 1.3 (b) shows arcade of magnetic field lines between regions of opposite polarities separated by a polarity inversion line (PIL). The foot points of the field lines move relative to each other due to the photospheric motion, which creates shear (stress) in the magnetic field. Eventually the sheared field lines reconnect, creating the flux rope and below it the post-

eruption arcade (Figure 1.3 (c)). The arcades are formed during the reconnection, but they become bright when the evaporated hot chromospheric plasma moves upwards and fills the field lines. The insert in Figure 1.3 (c) shows an EUV image of the flare arcades. In cartoon adapted from Gopalswamy (2010) in Figure 1.3 (a), we can see that the axis of the flux rope lies along the PIL and that the flux rope connects the two opposite polarity regions (denoted as D1 and D2) across the neutral line. D1 and D2 are the dimming regions where the feet of the CME are anchored to the Sun. Associated events are also observed: post-eruption arcades (flare arcades) rooted in the opposite polarity lines of the flare ribbons (R1 and R2), which are bright sources of hard X-ray (HXR) emissions due to accelerated electrons precipitating to the chromosphere. High energy electrons trapped in closed magnetic structures produce microwave bursts (μ), whose sources typically located above the HXR sources. The energy source of the solar eruption is free magnetic energy that is accumulated due the stressed the magnetic field lines of the erupting region through the shearing motion. This stored energy is released in the form of flares and CMEs by means of magnetic reconnection. Further details of the eruption process are shown in Figure 1.4. Currently, it is believed that shock-driving CMEs have 5 distinct substructures: the core (prominence/filament), the void (or flux rope), plasma pile up (at the outer edge of the flux rope), the sheath (accumulated material ahead of the flux rope) and the shock itself (left hand panel of Figure 1.4). During magnetic reconnection particles are accelerated to high energies (Dennis and Schwartz 1989). These flare-accelerated particles either propagate along the flare loops downward in the solar atmosphere, where they interact with the lower layers of solar atmosphere resulting in X-ray and gamma rays or they escape into IP space, where they are detected as solar energetic particles (SEPs). Escaping flare-accelerated electrons can also produce enhancements of radio emission known as type III radio burst.

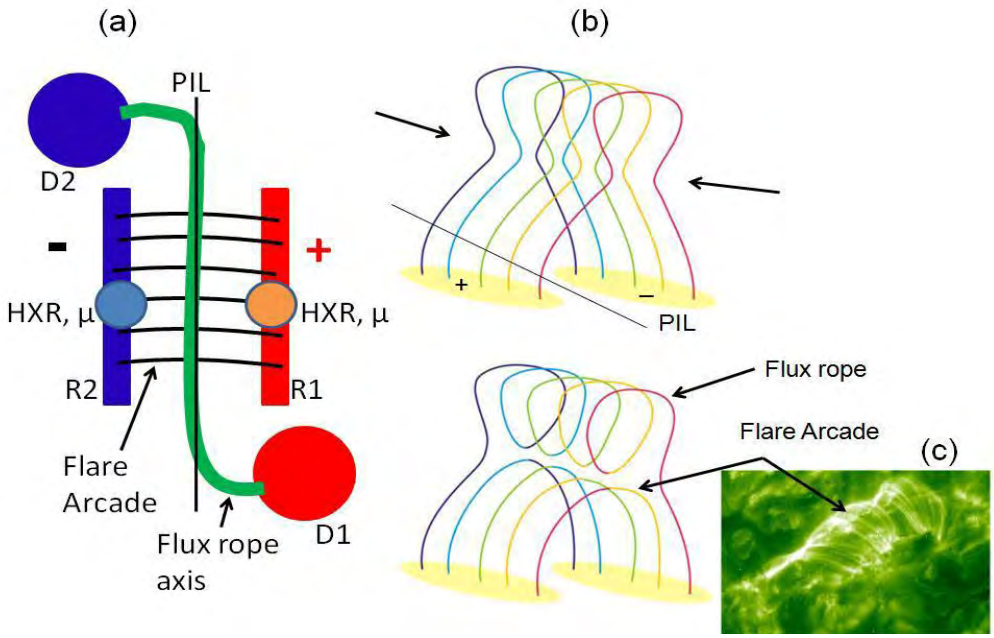

Figure 1.3. (a) A schematic picture of flux rope eruption at the Sun. The black dash and red cross are the negative and positive polarities of the magnetic field. The green is the flux rope (FR) axis showing how the FR connects across the polarity inversion line (PIL in black). D1 (red) and D2 (blue) are the feet of the FR at opposite polarities (positive and negative, respectively) called dimming 1 and 2, respectively. The two vertical blue and red lines are the flare ribbons (R1 and R2) at the two opposite polarities, respectively. Superposed to R1 and R2 are the hard x-ray (HXR) and microwave (μ) emissions due to flare-accelerated particles impinging the dense plasma at the foot points of the arcade, respectively. (b) The configuration of the magnetic field lines before and after the reconnection has occurred. (c) A schematic depiction of the post-eruption (flare) arcade and above it the FR that erupts as a CME. Figure is adapted from Gopalswamy (2010).

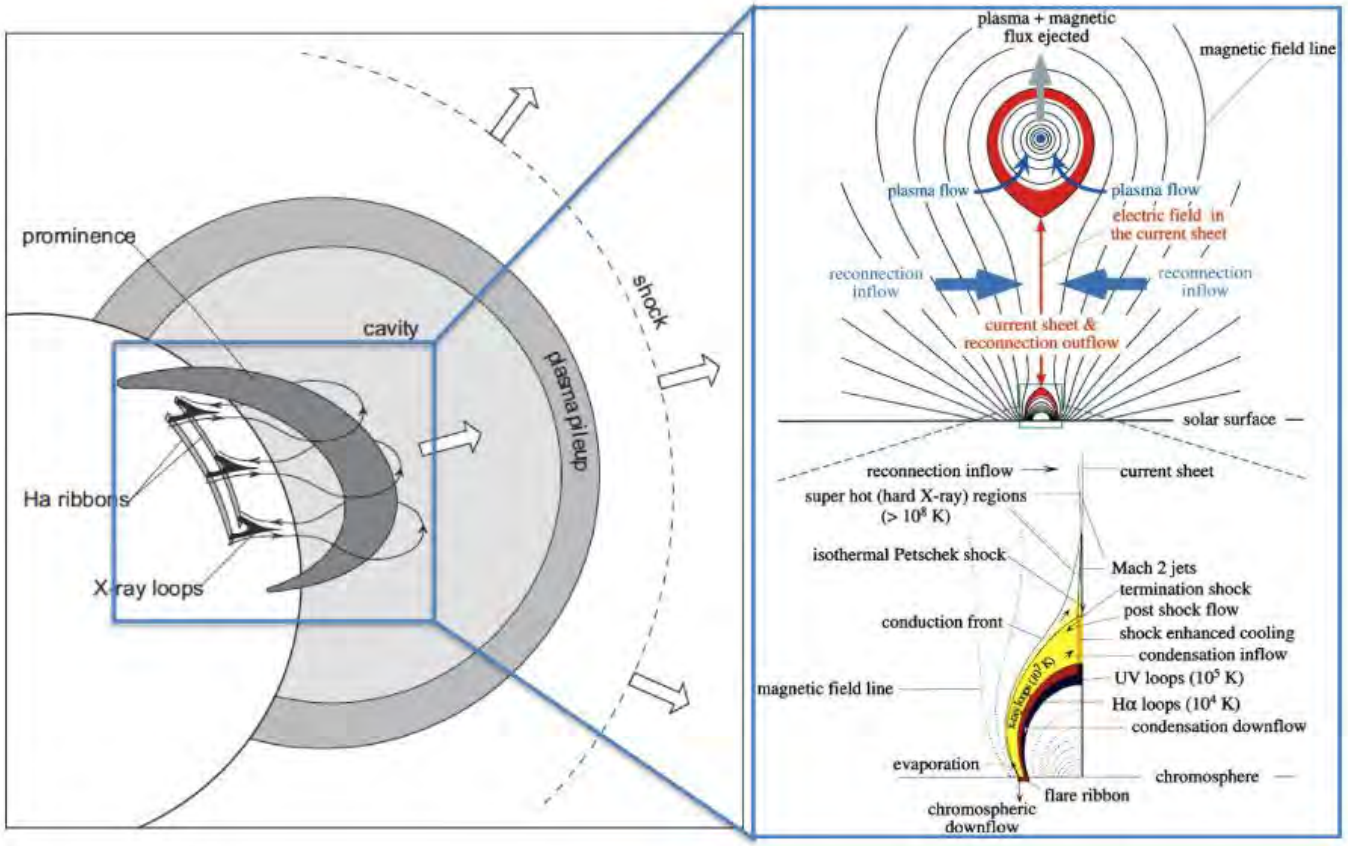

Figure 1.4. The structure of the CME with its different parts (prominence, cavity, plasma pile up and the shock) (left) and details of reconnection event including the flux rope, the current sheet, the reconnection outflows, flare loops and ribbons together with other flare associated phenomena (right). The sheath is the compressed plasma between the shock and the plasma pile up. This figure is adapted from Lin et al. (2004) (left) and Hudson et al. (2006) (right).

When CMEs are super-Alfvenic (have a much higher speed than the characteristic speed of the ambient medium) they are able to drive shocks and these shocks in turn accelerate electrons and ions (see Figure 1.5). The beams of the accelerated electrons induce Langmuir waves, which decay or interact with each other and are converted to electromagnetic waves (Ginzburg and Zhelezniakov 1958). These radio waves are detected as type II radio bursts. The accelerated ions are detected by in-situ particle detectors as solar energetic particles (SEPs). The white-light CMEs are imaged by coronagraphs and the type II radio bursts are detected by radio receivers. SEPs are also detected both by space and ground based instruments.

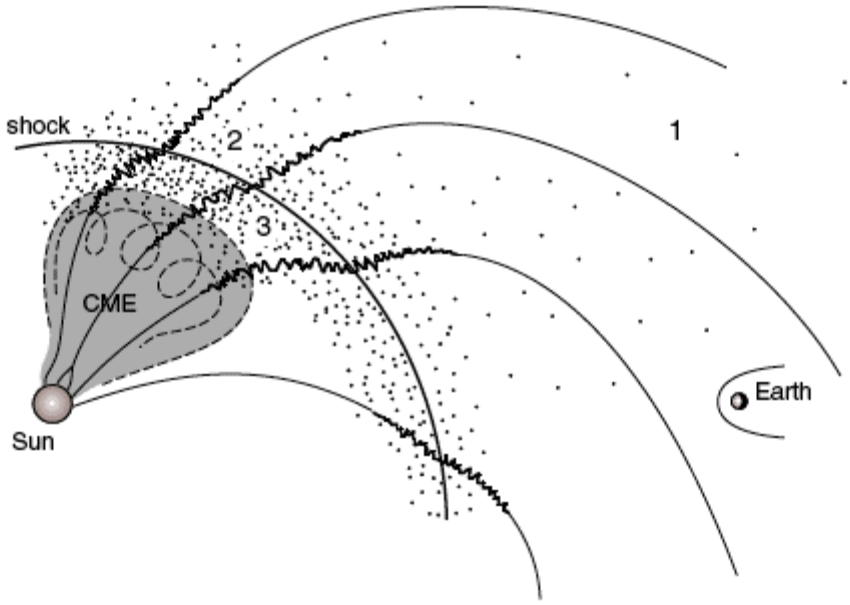

Figure 1.5. A schematic showing the acceleration of particles at the shock front of the CME and the propagation of some of the particles along the open magnetic fields. "1" marks the escaping particles (SEPs) along the interplanetary open magnetic field. Some of the SEPs pass through the Earth. This figure is adapted from Mikic and Lee (2006).

1.1.3 Instrumentation

We are using multi-wavelength, multi-instrument and multi-spacecraft data to understand large scale disturbances from the Sun, such as the CME, shocks, radio bursts and SEPs. CMEs and radio emissions from the Sun can be detected by radio receivers either from the ground or from space. Radio emissions below ~10 MHz cannot be observed from the ground due to the well-known ionospheric cutoff (Gopalswamy 2004a). Hence space born satellites are needed to measure the low frequencies.

The following sub-sections are short summaries of these instruments. Data from these instruments are used extensively in the studies presented here.

1.1.3.1 Large Angle Spectrometric Coronagraph (LASCO) on board the Solar Heliospheric Observatory (SOHO)

The Solar Heliospheric Observatory (SOHO, Domingo et al. 1995) spacecraft was launched on 1995 December 2 with the Large Angle Spectrometric Coronagraph (LASCO, Brueckner et al. 1995) on board. SOHO is located about the ecliptic plane at 0.99 Astronomical Unit (AU) on a halo orbit around the Lagrangian L1. The LASCO instruments originally included three coronagraphs namely C1, C2 and C3. However, the C1 stopped working in 1998. The field of view (FOV) of the C2 and C3 ranges from 2.1–6.0 and 3.7–32 Rs (Brueckner et al. 1995), respectively. A coronagraph is like any other telescope, except it has an occulter (a disk) that blocks the bright photospheric light from entering the telescope. This allows us to clearly image the much fainter solar corona. Figure 1.6 is a LASCO/C3 image from http://lasco-www.nrl.navy.mil and shows the key features of the LASCO image. The large disk (the occulter), which blocks the photospheric light, is kept in place by the occulter pylon. The size of the Sun is indicated by the white circle drawn on the occulting disk. Coronal streamers and stars are observed as white-light enhancements over the blue back ground. LASCO has observed more than 20,000 CMEs over the past 20 years (http://cdaw.gsfc.nasa.gov).

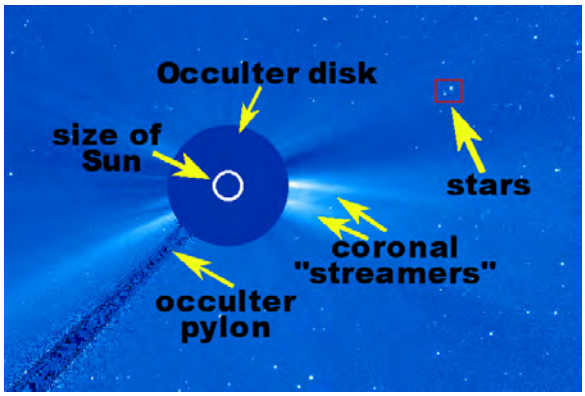

Figure 1.6. A C3 image from SOHO LASCO, showing key coronal features in the field of view (FOV). An image from http://lasco-www.nrl.navy.mil.

1.1.3.2 Sun Earth Connection Coronal and Heliospheric Investigation (SECCHI) on board the Solar Terrestrial Relations Observatory (STEREO)

The twin spacecraft of Solar Terrestrial Relations Observatory (STEREO, Kaiser et al. 2008) were launched in 2006. The two spacecraft started orbiting the Sun near Earth at heliocentric distances of 0.9 and 1.2 AU, respectively. Because their radial solar distances are different, they have different orbital speeds, which cause them to drift away from Earth by 22° each per year. The leading and trailing STEREO compared to the Earth are called STEREO Ahead (STEREO-A) and Behind (STEREO-B), respectively. The Sun Earth Connection Coronal and Heliospheric Investigation (SECCHI, Howard et al. 2008) is a suite of instruments on board STEREO. SECCHI has 5 different imaging instruments which image the solar disk and the corona from the Sun all the way to 1 AU. These instruments are the Extreme Ultraviolet Imager (EUVI, Wülser et al. 2004), Coronagraph 1 (COR1), Coronagraph 2 (COR2), Heliospheric Imager 1 (HI1) and Heliospheric Imager 2 (HI2) with FOVs 1–1.7, 1.5–4, 2.5–15, 15–84 and 66–318 Rs, respectively. The large FOV of the SECCHI helps us to observe a CME at the distances

corresponding to long wavelength radio emissions. HI1 and HI2 CME images correspond to type II bursts extending to the kilometric wavelengths.

The image of the STEREO spacecraft and a CME image in HI1 in SECCHI Ahead (HI1-A) at 2010 April 08 are displayed in Figure 1.7, respectively. Mercury is observed as a white dot.

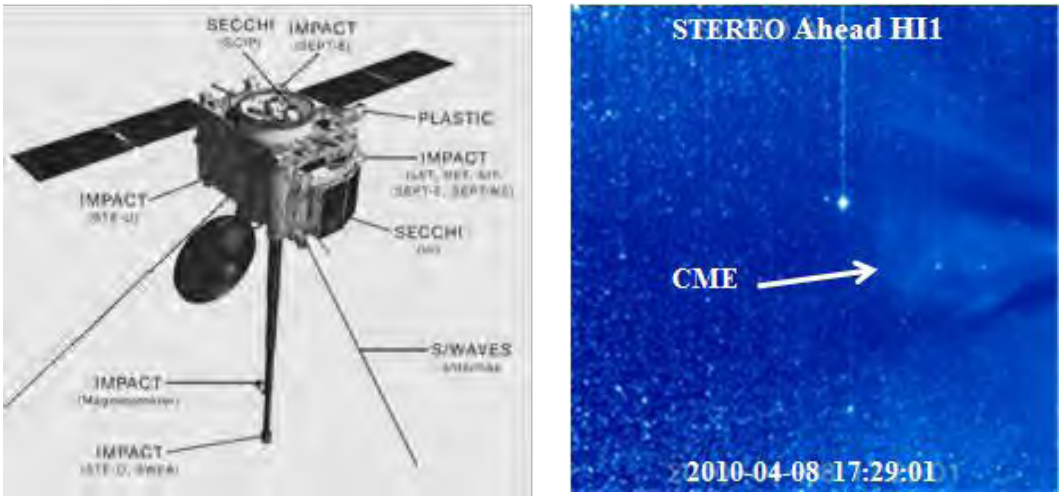

Figure 1.7. Left panel is the STEREO image with its instruments listed while right panel is a HI1-A direct white-Light image of a CME occurred on 2010 April 08 at 17:29 UT. The white dot is Mercury. Left panel image is from http://stereo.gsfc.nasa.gov/spacecraft.shtml and the right panel image is from http://cdaw.gsfc.nasa.gov/stereo/daily_movies/.

1.1.3.3 Radio and Plasma Wave Experiment (WAVES) on board Wind and STEREO

The WAVES (Bougeret et al. 1995) radio instrument on board the Wind (Acuña et al. 1995) spacecraft is space-based radio receiver packages. The spacecraft was launched on 1994 November 1. Its orbit has varied over the years, but currently it is located at L1 point in the ecliptic plane. It has 8 different instruments on board. The WAVES has two radio receivers called Radio Receiver Band 1 (RAD1) and Band 2 (RAD2). The frequency range of RAD1 and

RAD2 is 1040–20 kHz and 13.825–1.075 MHz, respectively. These correspond to wavelength ranges 288.5 m–15 km and 21.7–279 m, respectively. Figure 1.8 shows the Wind spacecraft.

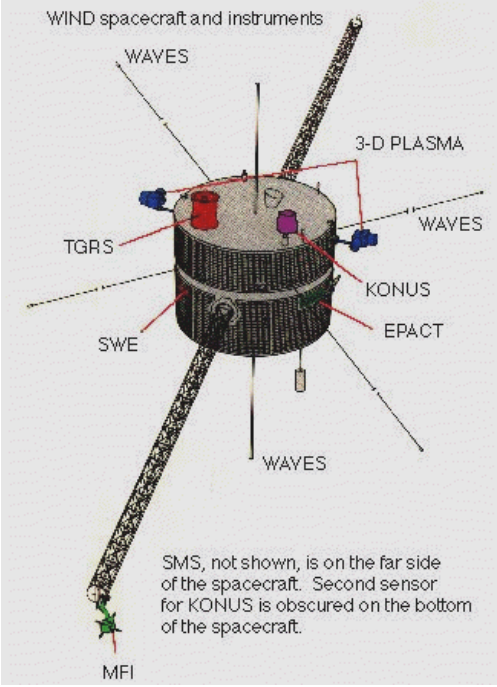

Figure 1.8. The Wind spacecraft with its instrument packages. The 3 radio antennas are marked by "WAVES". The image is from http://pwg.gsfc.nasa.gov/wind.shtml.

The twin STEREO spacecraft have also radio receivers called S/WAVES (Bougeret et al. 2008). The range of frequency of observations is 16000–30 kHz. The S/WAVES experiment is displayed in the assembly of STEREO instruments in Figure 1.7. Figure 1.9 shows samples of dynamic spectra obtained by Wind/WAVES on 2002 August 16 and STEREO-B/WAVES on 2012 January 12. Three types of radio bursts (type II, III and IV) are marked on the plots. The type IV bursts in each dynamic spectrum end in the decametric range. The type III bursts extend to kilometric range. The type II burst in the WAVES continues into the kilometric range. The

type II burst in the S/WAVES dynamic spectrum is short lived and ends in the decameter-hectometric (DH) range.

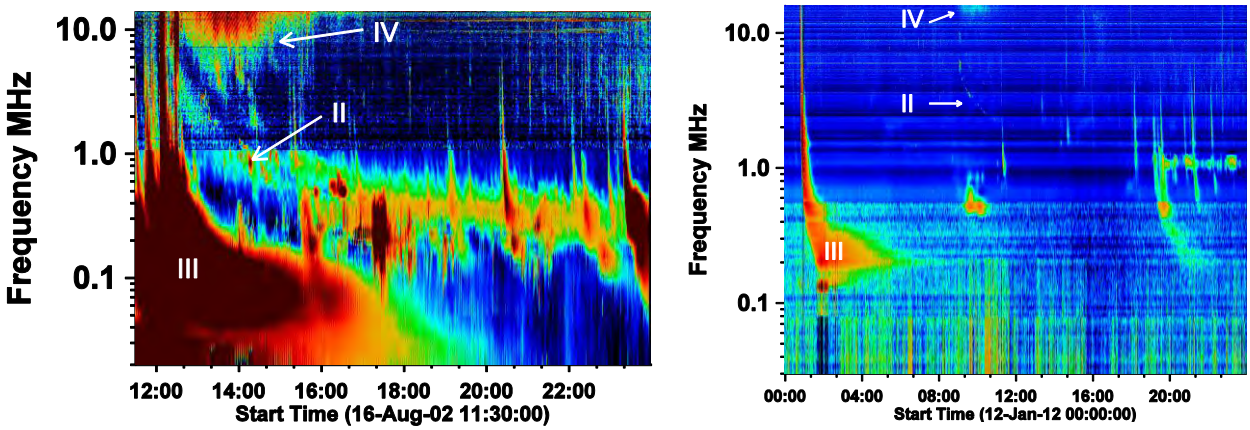

Figure 1.9. A radio dynamic spectrum from (Left) Wind/WAVES on 2002 August 16 and (Right) STEREO-B WAVES on 2012 January 12. Type II, III and IV radio bursts are observable on both the radio dynamic spectra. The type IV burst is at the decametric range and the type III burst decametric extends to kilometric in both images. The type II burst is at decametric-hectrometric to the right but continues to kilometric to the left dynamic spectrum. Left panel image is from http://cdaw.gsfc.nasa.gov/CME_list/index.html and the right panel image is from http://cdaw.gsfc.nasa.gov/stereo/daily_movies.

1.1.3.4 Example of Ground-based Radio Telescope: HiRAS

Radio emission above the ionospheric cutoff frequency are observed by ground-based radio receivers. There are many ground-based radio telescopes but not all of them are used to observe the Sun. The radio telescopes of Radio Solar Telescopic Network (RSTN), CULGOORA and HiRAS are examples of ground-based radio receivers used to observe the solar radio emission. For example, HiRAS radio telescope in Japan consists of 3 antennas namely HiRAS-1, HiRAS-2 and HiRAS-3 with frequency of observations 25–70, 70–500 and 500–2500 MHz, respectively (http://sunbase.nict.go.jp/solar/denpa/hiras/doc.html). Figure 1.10 shows the low-frequency-band HiRASO (HiRASO-1) telescope and a dynamic spectrum from HiRAS. Three major radio bursts

are observed: type II III, and IV at the metric wavelength range. The type II burst has the typical fundamental (F) and harmonic (H) structures.

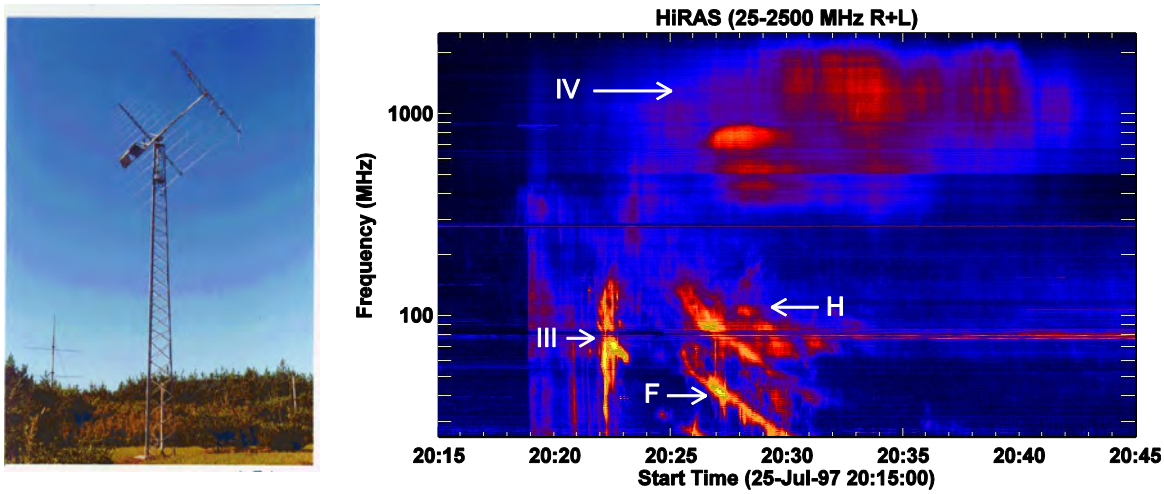

Figure 1.10. (left) An image of HiRAS-1 antenna. Its frequency range is from 25 to 70 MHz. (right) HiRAS radio dynamic spectrum on 1997 July 25. Type II (shown in "F" and "H"), III and IV bursts in the metric range are observable. The type II burst starting around 20:25 UT has fundamnetal ("F") – harmonic ("H") emission. Left and right image extracted from http://sunbase.nict.go.jp/solar/denpa/hiras/antennas.html and http://sunbase.nict.go.jp/solar/denpa/hiras/gif/97072520.gif, respectively.

1.1.3.5 Particle, X-ray, and EUV instruments

In this work other instruments are also used for example, X-ray and particle detectors on board GOES satellites (http://goes.gsfc.nasa.gov/), the Soft X-Ray Telescope (SXT) on board YOHKOH (http://solarscience.msfc.nasa.gov/Yohkoh.shtml), the Atmospheric Imaging Assembly (AIA, Lemen et al. 2012 or http://aia.cfa.harvard.edu/) on board the Solar Dynamic Observatory (SDO, Pesnell et al. 2012 or http://sdo.gsfc.nasa.gov/), ExtremeUltraviolet Imaging Telescope (EIT, Delaboudiniere et al. 1995 or http://umbra.nascom.nasa.gov/eit/) and Michelson Doppler Imager (MDI, http://sohowww.nascom.nasa.gov/) on board the SOHO. The FOV of EIT

is 1−1.4 Rs. SOHO also provides solar wind plasma information from the in-situ observations by the Charge, Element, and Isotope Analysis System/Mass Time-of-Flight (CELIAS/MTOF) Proton Monitor (PM).

The overlap in the region of the corona and beyond observed by both the CME imagers (LASCO and SECCHI) and WAVES (on board the Wind and STEREO) has helped to understand the CME-type II burst relationship in great detail (see Gopalswamy et al. 2001a).

1.2 Literature Review

1.2.1 Coronal Mass Ejections

CMEs are ejections of magnetized plasma clouds from the corona that were discovered in white light in the 1970s (Hansen et al. 1971; Tousey 1973). The first white-light transient was observed from the ground during 1970 August 11–12 (Hansen et al. 1971). Soon after coronal transients were also observed from space: on 1971 December 14 the white-light coronagraph on board the Orbiting Solar Observatory-7 (OSO-7) spacecraft (Tousey 1973) observed the first CME from space. These coronal transients were named as coronal mass ejections after the Apollo Telescope Mount (ATM) (MacQueen et al. 1974) coronagraph on board the Skylab had detected more than a hundred of them. Currently, the LASCO coronagraphs on board SOHO and the coronagraphs and heliospheric imagers of the SECCHI on board the STERO spacecraft are the main instruments for imaging CMEs.

The association of a geomagnetic storm, the disturbances of the Earth‟s magnetosphere, with mass motion from the Sun was suggested before 1920s, which later helped the discovery of CMEs. The ejections were considered as magnetized gas clouds (Parker 1957). Gold (1962) assumed them to be solar gas from eruptions, and to carry with them solar magnetic fields (said

to be "frozen-in" to the moving plasma) still connected to the Sun. He described them as a magnetic bottle driving the MHD shock at the leading edge (see Figure 1.11).

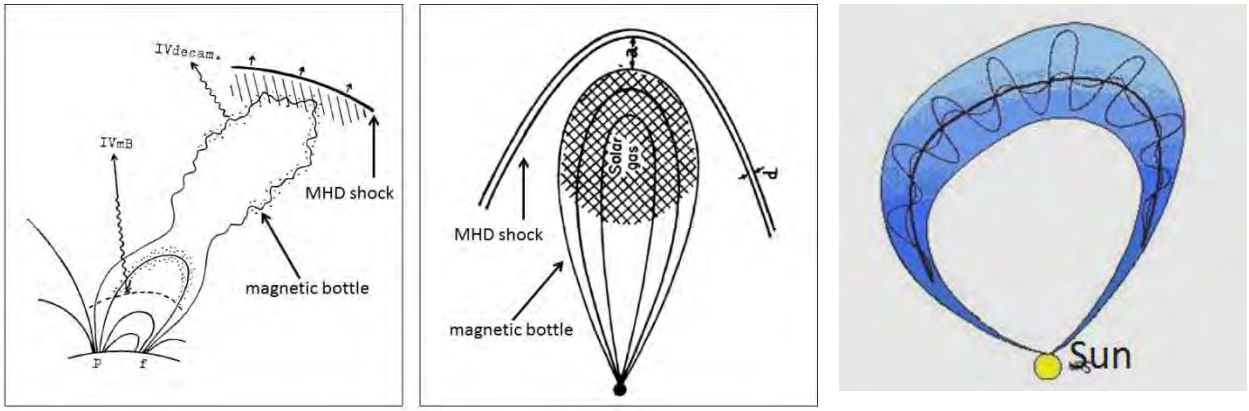

Figure 1.11. Magnetic gas cloud driving MHD shock as described by Fokker (1963) near the Sun (left), by Gold (1962) in the interplanetary medium (middle) and the current MC cartoon (right). Magnetic loops, associated type IV burst, the magnetic bottle and the MHD shock are described to the left. Middle panel shows the magnetic bottle anchored to the Sun, mass frozen in the magnetic bottle (solar gas), MHD shock, shock curvature "a" and shock thickness "d". The figure to the right shows the magnetic cloud with its twisted magnetic fields. The left two figures are from Gopalswamy (2016) and the right is from http://wind.nasa.gov/mfi/images/magcloud.gif

Nowadays, the magnetized gas clouds or the solar gas carrying a frozen-in magnetic field are called either magnetic clouds (MC) or ejecta (EJ) depending on the observed geometry of the magnetic field lines at 1 AU. Burlaga et al. (1981) first identified transient ejecta with well-ordered magnetic fields behind a shock and a sheath region of the turbulent hot plasma compressed by the shock and consisting of highly variable magnetic field. They observed that the shock-driving magnetic structure had high magnetic field, low temperature and smooth rotation of the field vectors indicating a loop structure, and called it a MC. Subsequently the helical magnetic field of the MC has been called a flux rope (Klein and Burlaga 1981). This is consistent with the original suggestion by Gold (1962) except that the magnetic fields are

twisted. Goldstein (1983) first modelled the magnetic structure of the magnetic cloud as a flux rope. The flux rope can be formed before eruption or after eruption (Gibson et al. 2006; Low 1997).

SOHO and STEREO provided direct evidence of the flux ropes in coronagraphic images. The sheath region between the shock and the CME leading edge were first identified in the SOHO white-light images by Sheeley et al. (2000). Figure 1.12 (a) shows a CME in the direct image of the coronagraph C2 of SOHO/LASCO observed on 2005 January 15 at 06:30 UT. The three distinct parts of the CME: the core (prominence), the cavity (the flux rope) and the leading edge are observable. The sheath is observable in Figure 1.12 (b) which shows a LASCO difference image superposed on an EIT difference image. The shock is assumed to be the outer edge of the sheath region, but the shock itself is invisible, because it is very thin structure. Figure 1.12 (c) shows a CME on 2012 August 20 at 14:25 UT by STEREO-A/COR1 (a running difference image) superposed onto EUVI image. It has a clear flux rope structure. Recent studies have suggested that all interplanetary CMEs (ICMEs) may be flux ropes (Gopalswamy et al. 2013a).

A study by Gopalswamy (2009) of CMEs during solar cycle 23 shows that the average speed, width and acceleration of a CME is 470 km s^{-1}, 54° and −0.4 m s^{-2}, respectively. Gopalswamy (2009) also estimated the average kinetic energy of the CME to be 5.4×10^{22} J. Halo CMEs form a special class of CMEs. Halo CMEs are regular CMEs that are seen to surround the occulting disk of the coronagraph because they are propagating away or towards the Earth (Howard et al. 1982). Halo CMEs are known to be fast and wide CMES on average. Front-side halos are important for space weather since they directly impact Earth. Approximately 4% of the general population of CMEs is halo (Gopalswamy et al. 2010a).

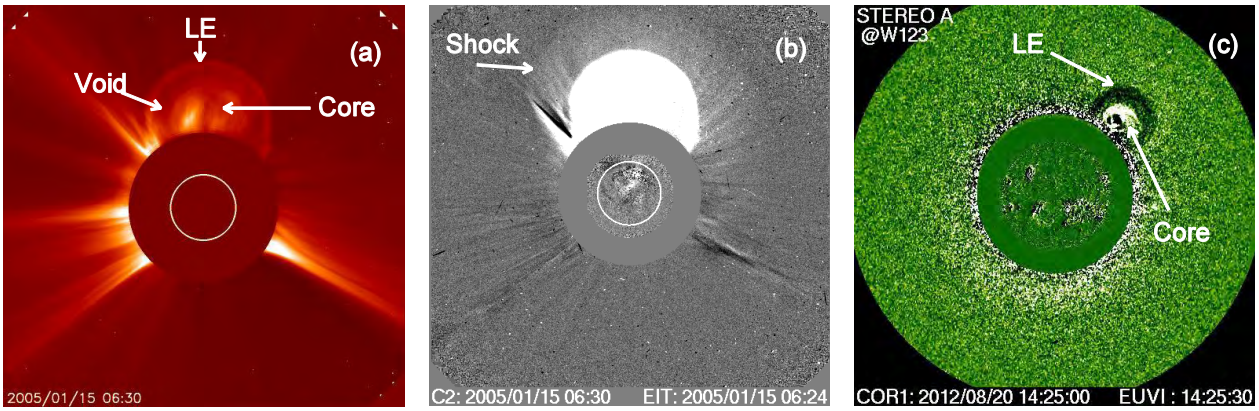

Figure 1.12. (a) A CME in the C2 FOV (direct image) on 2005 January 15 at 06:30 UT. The leading edge, the cavity and the core are clearly observable. In (b), same image as in (a) but a pre-event image has been subtracted to see the change in the corona. The bright feature is the envelope containing the flux rope and the core. The faint feature is the shock sheath. The shock is assumed to be at the leading edge of the sheath. (c) a running difference image from STEREO-A/COR1, with a superposed EUV I image for a different CME on 2012 August 20 at 14:25 UT. In this case, the core, flux rope (dark region), and faint leading edge are observable. (a) and (b) are from Gopalswamy (2010). (c) is from http://cdaw.gsfc.nasa.gov.

1.2.2 Solar flares, SEP events and Solar activity cycle

CMEs are associated with different types of eruptive activities which include flares, post-eruption arcades, SEPs, type II radio bursts and type IV radio bursts.

Flares occur as the result of the reconnection of magnetic fields on the Sun as explained in Section 1.2. Flares can be broadly classified into A, B, C, M or X class, which correspond the peak soft X-ray flux of $< 10^{-7}$, 10^{-7} to 10^{-6}, 10^{-6} to 10^{-5}, 10^{-5} to 10^{-4} and $> 10^{-4}$ W m^{-2}, respectively (Gopalswamy, 2009). Flares emit soft X-rays (gradual), hard X-rays (impulsive), extreme ultraviolet (EUV), microwave (μ) and gamma rays. The soft X-rays are due to thermal electrons at the reconnection site in the corona (a few MK to > 10 MK) temperature, according to the relation $\lambda_{max}T = 0.0029$ mK), but hard X-rays are due to nonthermal electrons precipitating to the chromosphere. Soft X-rays have energies of a few keV (J), while hard X-rays have energies

in the range 10–300 keV ($1.6 \times 10^{-15} – 4.8 \times 10^{-14}$ J). Soft X-ray flare dominates the hard X-ray emission. The EUV emission originates from the chromosphere, transition region and the corona. The gamma rays are due to the nuclear process in the chromosphere when accelerated protons interact with the chromospheric nuclei.

CMEs and flares are two manifestations of the same eruption (Low 1994; Harrison 1995), but a CME takes on average the largest component of the released energy (Emslie et al. 2012). All CMEs are associated with flares but not the reverse (Bougeret 1985). There are intense X-class flares that are not associated with CMEs, because the flux rope fails to escape due to restricting overlying magnetic field lines (Veronig and Polanec 2015). These are called confined flares. However, intense flares (> X3) are always associated with CMEs.

Post-eruption arcades are the closed magnetic loops formed after the reconnection during flare and CME eruption. They are series of closed magnetic field lines rooted at the opposite polarities across the neutral line as discussed in section 1.2 (see Figure 1.3).

The sunspot number (SSN) has an 11-year cycle. The 11-year cycle is actually a half of a 22-year magnetic polarity reversal cycle of the Sun, where the global solar magnetic field polarity reverses, i.e., the magnetic South and North Pole switch places about every 11 years resulting in a 22-year full cycle. Sunspots are mostly located in the latitude range between ±30°. The CME-SSN correlation was first studied by Hildner (1976). Study by Gopalswamy et al. (2010b) shows that SSN and CMEs are correlated. They have weak correlation during solar maximum due to large number of CMEs erupting from the polar crowns (non-sun spot regions).

SEPs were discovered by Forbush (Forbush 1946). SEPs can be produced by flares and/or the shocks at the CME front (Cliver et al. 1982; Cane et al. 1988; Reames 1990). CMEs are the main producers of SEPs (Kahler 1992). SEPs are charged particles that propagate along the interplanetary magnetic field lines. Therefore, in order to reach Earth, SEP source must be

magnetically connected to Earth. Figure 1.5 depicts the acceleration of SEPs at the shock front and its connection to Earth.

1.2.3 Solar Radio Bursts

Acceleration of electrons to nonthermal energies by transients (flares or CMEs) from the Sun are responsible for various types of radio emissions. A small fraction of the electron energy gets converted into electromagnetic waves in the radio domain. The acceleration mechanism and distribution of the electrons decide the intensity and spectrum of the radio waves. Based on the frequency and its time evolution, solar radio bursts can be identified and classified into different types. Type I bursts are due to weak electron beams accelerated in the process of active region evolution, type II radio bursts are due to electrons accelerated by shocks driven by CMEs, type III radio bursts are due to beams of electrons that are accelerated at the flare site and propagate along open magnetic field lines, and Type IV bursts are due to electrons accelerated at the flare site and trapped in post-eruption arcades. Type V bursts are a variant of type III bursts in that they travel along curved open field lines (see Gopalswamy 2011a for a review). The frequency of emission (f) and the density of the local plasma (n) are related by $f \approx \sqrt{(n)}$. Sources of these radio bursts can be tracked all the way to the interplanetary medium, which allow us to gain information about the radio source and the medium they propagate. A 30 MHz radio emission corresponds to a density level of 1.1×10^7 cm^{-3} in the solar corona and density measurements from eclipse observation show that this density corresponds to a heliocentric distance of ~ 10 Rs (Gopalswamy 2004b). Although there are a wide variety of such radio emissions close to the Sun extending to shorter wavelengths, the three burst types (type II, III and IV) dominate in the interplanetary (IP) medium. Figure 1.13 shows that the flux density of radio emissions from the quiet Sun is dominated at any distance range by nonthermal radio emissions (type II and III).

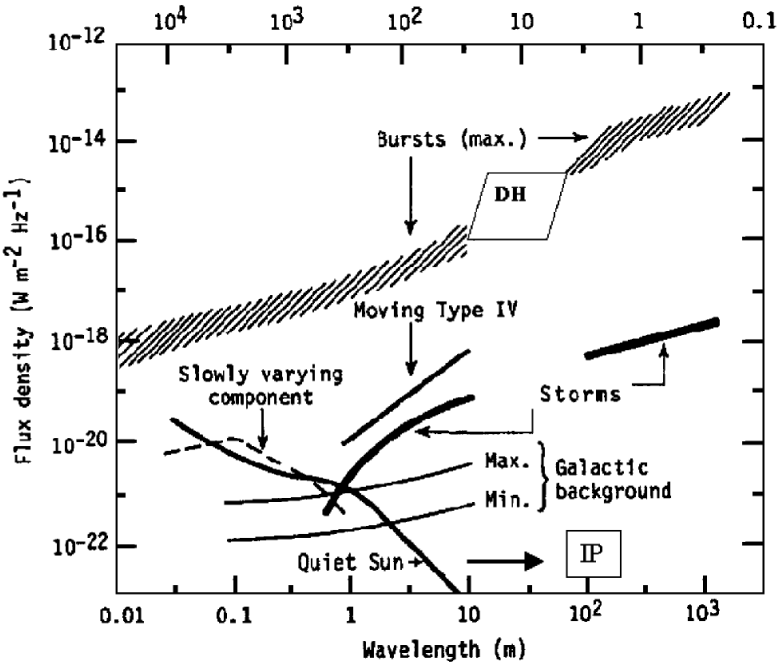

Figure 1.13. The radio flux of the different radio emissions from the quiet Sun and nonthermal electrons at the corona and in the interplanetary medium. "Bursts (max)" refers to the type II and III bursts. "Storms" indicates to type III storm. "Max." and "Min." show the maximum and minimum galactic background intensity. The type II and III bursts dominate both in the coronal and interplanetary medium (IP). Image is from Gopalswamy (2004b).

Type II radio bursts were first identified by Payne-Scott et al. (1947) who reported the observation of slowly drifting radio bursts at three frequencies. Latter these slow drifting bursts were called type II radio bursts by Wild and McCready (1950). Type II bursts are observed over a wide wavelength range, spanning metric (m), decametric (D), hectometric (H), kilometric (km) wavelength domains and a combination of them (Gopalswamy 2010). Figure 1.14 shows these wavelength ranges. Type II bursts are indicative of shock-driving CMEs. CMEs propagating with a super-Alfvenic speed drive MHD shocks (e.g., Gopalswamy 2004a). The shocks in turn accelerate electrons that induce Langmuir waves in the ambient medium. The Langmuir waves are converted to electromagnetic (radio) waves at the local fundamental and/or harmonic plasma frequency detected as a type II burst by radio receivers in space and on the ground. This emission

process is known as coherent plasma emission (Ginzburg and Zhelezniakov 1958; Nelson and Melrose 1985; Cairns and Melrose 1985; Cairns 1987a, b).

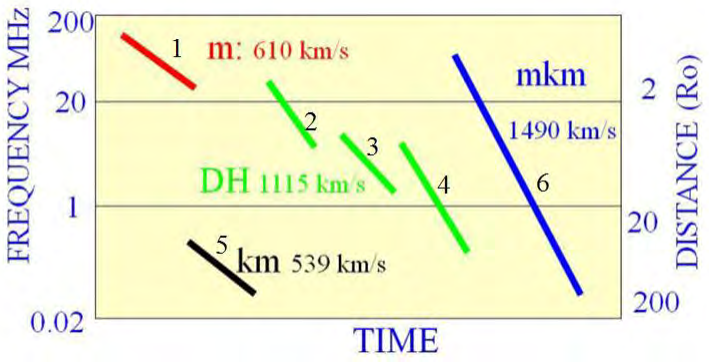

Figure 1.14. Frequency ranges of type II radio bursts and the average speeds of the associated CMEs. The numbers "1", "2", "3", "4", "5" and "6" indicate the m (metric), pure DH (Decametric-hectometric), m-DH (metric-DH), km (kilometric), DH-km and m-km type II bursts and the associated CMEs. CMEs associated with m-km type II bursts have the highest speed. Right-hand scale shows the typical height of the type II emission source in Solar radius (Ro). Figure is from Gopalswamy (2010).

The typical high-frequency cutoff of type II bursts is ~150 MHz (Gopalswamy 2000; 2011b), although type II bursts are occasionally observed at much higher frequencies (Cho et al. 2013). The range frequencies of radio bursts that can possibly be observed originate from the chromosphere all the way to the interplanetary medium range 300 GHz–3 kHz (Gopalswamy 2004b).

1.3 Rationale of the Research

The connection between solar activity and geomagnetic storm was understood since early 1900s. Our modern society is dependent on space satellites and ground based technologies, which can

be highly vulnerable to the effects of geomagnetic storms. An exemplary situation is the Halloween period, 2003 October 28, (Gopalswamy et al. 2005b). There were intense flares and extremely fast CMEs that had significant space weather impact on Earth and other destinations in the heliosphere. Space weather is greatly affected by the Sun‟s emissions such as SEPs, CMEs and EUV radiation. The two primary CME space weather effects are particles accelerated by the CME driven-shock and the production of geomagnetic storm when the CME hits the magnetosphere. Studies have shown that CMEs play the greatest role in space weather (Gopalswamy 2009). Accordingly, an early warning before the arrival of such potentially dangerous CMEs is important. Those CMEs that are heading towards Earth and have an appropriate magnetic configuration can cause space weather disturbances. Today, there are empirical and analytical CME models that can allow us to predict the CME arrival within ~7 hours, but further improvements are needed (Gopalswamy et al. 2013b).

The properties of CMEs can be studied remotely before the arrival of the CME using the type II radio bursts associated with CME-driven shocks, because type II bursts are electromagnetic waves, which arrive at Earth in ~ 8 minutes. Our research focuses on the further study of type II bursts but in connection with the associated CMEs.

1.4 Objectives of the Research

The general objective of this research is to

- study the charactertics of radio emissions (regular type II bursts and Diffuse Interplanetary Radio Emissions (DIREs) and associated CMEs.

The specific objectives are to

- identify the radio source location complex type II radio bursts occurred on 2012 January 19 (a case study) and a new spectral feature (an interplanetary radio emission, DIRE) observed on 2001 September 27.
- study the charactertics of the DIREs and their associated CMEs
- investigate how the kinetic energy of CMEs organizes the wavelength range of type II bursts.

The thesis is divided into four chapters. The first chapter focuses on a complex type II burst observed by Wind/WAVES on 2012 January 19 which has two separate emissions: a short lived DH and long lived DH-km type II bursts. The investigation utilizes the white-light and radio measurements with added input from the SOHO and STEREO observations and search for the source of the radio emissions.

In Chapter 3, we report on a case study of one such event that occurred in 2001 September 27. We identify the source of the radio emission and discuss the possible mechanisms that produce it. We also study the kinematic properties of the associated CME. In chapter 4, we perform a statistical study of set of such events and their associated CMEs to understand the variability in the acceleration of non-thermal electrons in CME-driven shocks (the shock geometry, shock kinematics and the inhomogeneity in the ambient medium).

Gopalswamy et al. (2005a) measured the average speed, non-halo width, acceleration, and the fraction of full halo CMEs associated with the pure metric, DH and m-km type II bursts. All the quantities increased progressively from pure metric to DH and the m-km CMEs. They have shown that the CME kinetic energy organizes the different populations of the type II bursts. DH CMEs are more energetic than metric CMEs. On the other hand, m-km CMEs are the most energetic. In Chapter 5, we consider pure DH, m-DH and DH-km as separate groups, which were previously included under DH. This investigation will further clarify the hierarchical relationship especially in the interplanetary medium.

Chapter 2

A Study of the 2012 January 19 Complex Type II Radio Burst Using Wind, SOHO, and STEREO Observations

In this chapter we report on a case study of the complex type II radio burst of 2012 January 19 and its association with a white-light coronal mass ejection (CME). The complexity can be described as the appearance of an additional type II burst component and strong intensity variation. The dynamic spectrum shows a pair of type II bursts with fundamental-harmonic structures, one confined to decameter-hectometric (DH) wavelengths and the other extending to kilometric (km) wavelengths. The type II burst has no metric component. The type II burst also showed a sudden enhancement and upward shift of the emission frequency at km wavelengths. We provide quantitative explanations to these deviations as a consequence of the inhomogeneous ambient medium into which the CME-driven shock propagates. The inhomogeneity is caused by preceding CMEs with which the primary shock-driving CME interacts. By comparing the coronal density obtained from white-light polarization brightness images with that inferred from the fundamental component of the type II burst, and the CME-driven and the CME speed, we show that the long-lived type II radio emission (DH-km) primarily comes from the region above the shock flank. Using similar method, we show that the source of the short-lived DH component is near the nose.

2.1 Introduction

Type II bursts are slowly drifting features in the radio dynamic spectra in contrast to the fast drift of type III bursts. The slow drift is indicative of shock propagation with speeds in the range 500–3000 km s^{-1}, while the type III bursts are fast drifting because of the high-speed (a fraction of the speed of light) electron beams. The present work utilizes the white-light and radio measurements to analyze the complex type II burst observed by Wind/WAVES on 2012 January 19 with added

input from the SOHO and STEREO observations. The overall behavior of the type II burst and its association with white-light CME was already reported by Liu et al. (2013). However, they overlooked the presence of a short-duration, second type II at the beginning with a drift rate much higher than that of the long-lasting type II over the same frequency range. In fact, this type II burst is observed by all the three radio receivers (Wind, STEREO-A and STEREO-B). Furthermore, there is an enhancement in the long-lasting type II burst seen by all the three spacecraft. Liu et al. (2013)‟s CME height-time data points also fall on both fundamental and harmonic bands, so it is necessary to clarify the spectral features more closely. The enhancement also showed an upward shift in frequency. The frequency shift can be due to either the inhomogeneity of the ambient medium or interaction of the associated CME with the preceding CMEs (Gopalswamy et al. 2001a). The associated primary CME is a fast halo and it seems to be interacting with three preceding CMEs. The interaction signatures are clearly observed in the LASCO FOV and STEREO‟s Heliospheric Imager (HI1-B) FOV.

The purpose of this work is to explain the complex nature of the type II radio burst. First, we determine the speed of the CME from the height-time measurements. We compare the CME speed with the speed of the shock estimated from the radio dynamic spectrum. If the nose of the CME-driven shock is the source, the two speeds should be comparable and the plasma density corresponding to the fundamental emission should be similar to the density of the upstream of the shock nose. The background density of the coronal medium is obtained by the inversion of polarization brightness images (Schuster 1870; Minnaert 1930; van de Hulst 1950; Billings 1966; Quémerais and Lamy 2002; Thernisien et al. 2006) and compared with the plasma density inferred from the fundamental frequency of the type II emission. Finally, we compare the iso-density contour plots of the ambient medium with the white-light image of the CME and search for a section of the CME (shock) traversing the plasma density level having a density equal to the one obtained by inverting the frequency of the type II burst (Reiner et al. 1998). We compare our results with those of Liu et al. (2013).

Section 2.2 describes the radio and white-light observations. Sections 2.3 and 2.4 present the results and discussion. Section 2.5 summarizes the conclusions.

2.2 Observations and Analysis

The 2012 January 19 type II radio burst is observed by the WAVES instrument on board the STEREO and Wind spacecraft. The STEREO Ahead (A) and Behind (B) spacecraft were located at W108° and E113°, respectively on this day. Ground based radio observatories did not report any type II radio burst in the metric domain; there is only a weak continuum emission report in NOAA Solar Geophysical Data Report (e.g., http://solarmonitor.org/data/2012/01/19/meta/noaa_events_raw_20120119.txt).

Figure 2.1 shows the Wind/WAVES dynamic spectrum on 2012 January 19 showing the type II burst extending from ~14 MHz (DH to km wavelengths). The dynamic spectrum contains a complex set of type II emissions. In particular, there is an additional fundamental (F)-harmonic (H) pair, marked Segment 1 (S1) in the DH range. The regular type II in the DH-km wavelength is marked Segment 2 (S2), Segment 3 (S3), and Segment 4 (S4). In the km range (below 380 kHz) one can see a sudden enhancement with a slight upward shift in frequency (S3). Note that S2 and S3 constitute the main type II burst, while S1 is an additional component. S1 and S2 overlap in start time but differ in the frequency of emission and drift rate. S1 is a short-duration type II burst that lasts for about 10 minutes. The duration of S2 and S3 is ~ 3 and about ~ 2 hours, respectively. Beyond ~ 20:36 UT the F-H structure is not observed; the single structure seems to be just the harmonic (Segment 4, S4). The enhancement and upward shift in frequency of S3 is a clear signature of CME-CME interaction, first reported by Gopalswamy et al. (2001a). This part of the research is primarily concerned with the presence of S1 and the enhancement in S3 in the dynamic spectrum. Both S1 and S2 appear to start around the same time, but S1 is brighter and its slope in the frequency-time plane is steeper.

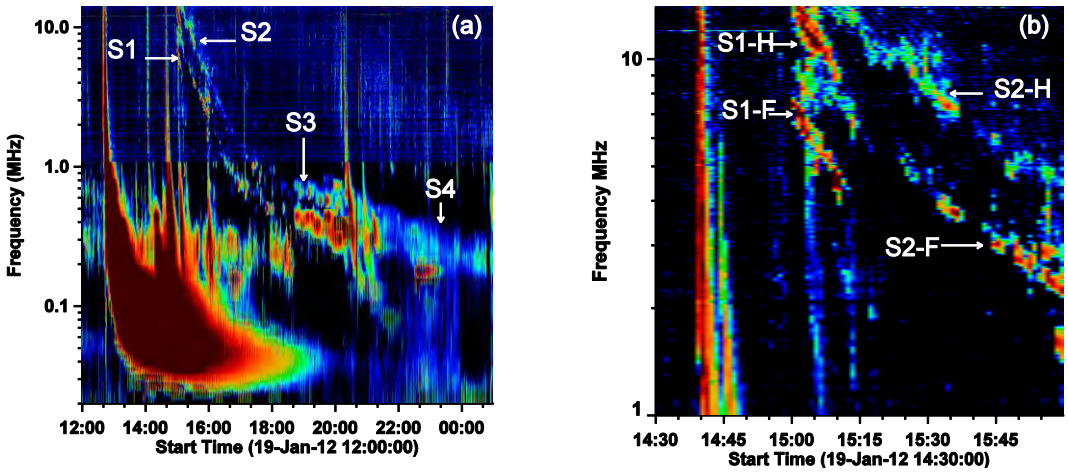

Figure 2.1. (a) The complex dynamic spectrum of the 2012 January 19 type II radio burst observed by Wind/WAVES showing all the components. The "S1", "S2", "S3" and "S4" represent for segment 1, segment 2, segment 3 and segment 4, respectively. (b) High-frequency section of the dynamic spectrum mainly showing the component S1. "S1-F" and "S1-H" represent the fundamental and harmonic components of S1. "S2-F" and "S2-H" represent the fundamental and harmonic components of S2.

The radio dynamic spectrum does not have spatial resolution, except for the fact that the emission frequency (and hence the plasma density) indicates a certain distance from the Sun. Fortunately, the EUV and white-light observations made during the type II radio bursts by SOHO and STEREO spacecraft provide details on the spatial evolution of the associated CME. The SOHO spacecraft provides EUV and white-light images from the EIT and the C2 and C3 telescopes of LASCO.

The type II burst is associated with an energetic CME observed by the coronagraphs on board STEREO and LASCO. We refer to this CME as the primary CME (PCME), which first appeared at 14:48 UT on 2012 January 19 in the LASCO/C2 FOV. The CME was reported to appear at 14:36 UT in the Coordinated Data Analysis Workshop (CDAW) CME Catalog (Yashiro et al. 2004; Gopalswamy et al. 2009), but we now know that the time corresponds to the appearance of

a preceding CME, which is quickly overtaken by the primary CME. The average sky-plane speed of PCME is 1120 km s^{-1}. The PCME is associated with an M3.2 flare from National Oceanic and Atmospheric Administration (NOAA) active region (AR) 11402 located at N32E22. A snapshot of the PCME and the associated GOES soft X-ray flare are shown in Figure 2.2. The eruption occurred in the northeast quadrant as can be seen from the difference image at 193 Å from the AIA on aboard the SDO spacecraft overlaid on the LASCO/C2 image. The PCME is also associated with a minor (~3 pfu in the >10 MeV GOES channel) SEP event. No SEPs are observed in the >50 and >100 MeV channels, consistent with the large shock formation distance characteristic of soft-spectrum events (Gopalswamy et al. 2015a). The associated shock reached Earth at 05:18 UT on January 22, as observed by SOHO/MTOF and Wind in-situ observations. The shock transit time is ~ 38.75 h, which corresponds to a transit speed of ~1075 km s^{-1} suggesting that the shock remained strong over the Sun-Earth distance.

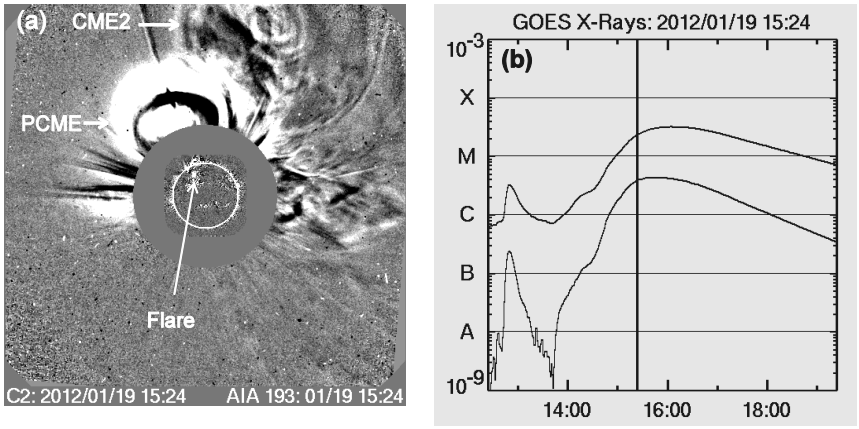

Figure 2.2. (a) The white-light CME of interest in the LASCO/C2 FOV at 15:24 UT. This is a running difference image in which the previous frame is subtracted. The LASCO image is overlaid by a running difference image obtained by the SDO/AIA image at 193 Å. The primary CME (PCME) and one of the preceding CMEs (CME2) are marked on the image. The lower arrow points to the solar source of the PCME. (b) GOES soft X-ray profiles (upper 1–8 Å; lower 0.5–4 Å) showing the M3.2 flare associated with the PCME. The vertical line marks the time of the LASCO frame in (a).

The PCME interacted with 3 preceding CMEs (see Figure 2.3). The 3 CMEs are denoted by CME1, CME2 and CME3 in the order they are overtaken by the PCME and appeared overlying high latitude loops with slow motion. At the beginning, the PCME captures CME1 first observed at about 14:24 UT (not reported in CDAW CME Catalog) in the C2 FOV. The CME1 originates from the same region as the PCME. This interaction does not seem to have any consequence in the dynamic spectrum because the shock does not form until later. The PCME then interacts with the eastern flank of CME2 observed at 09:48 UT in the C2 FOV. It originates from N38W57. The interaction is observed as deflection of the eastern flank of CME2. Finally, it interacts with CME3 in HI1 FOV as evidenced by a clear white-light enhancement and PCME deflection. CME3 is first seen at 12:24 UT in C2 FOV in the previous day. It originates from S23E21.

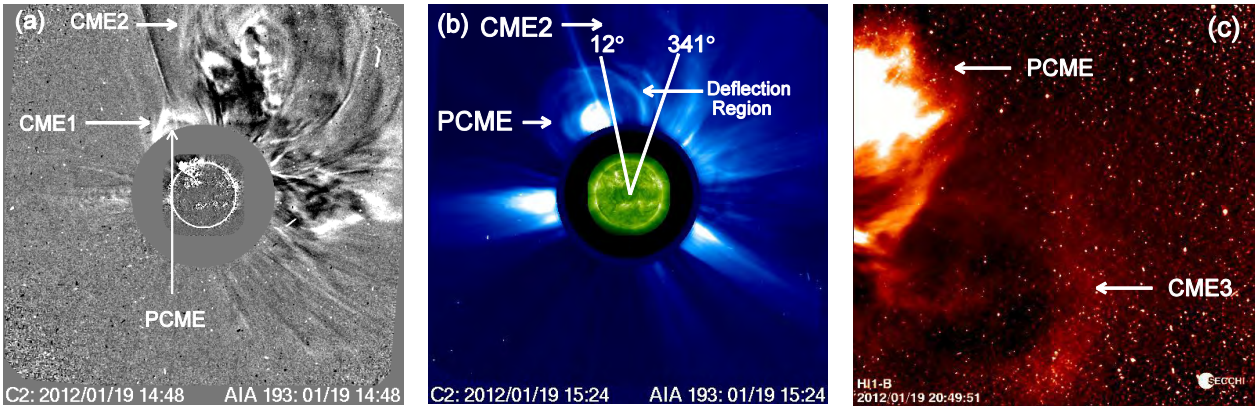

Figure 2.3. The primary CME and preceding CMEs observed in the FOVs of different instruments. (a) The LASCO/C2 running difference image shows observation of the PCME, CME1 and CME2. (b) The PCME and CME2 observed in the combined direct images of SDO/AIA 193 Å and LASCO/C2. The eastern flank of CME2 deflection is also indicated. The deflection swept by the cone is 31°. (c) The direct image by STEREO-B/HI1 shows the PCME and CME3.

2.3 CME Kinematics

2.3.1 CME Kinematics from White-light Observations

The height-time measurements of the PCME from the CDAW CME Catalog are presented in Figure 2.4. The PCME is moving with an average speed of 1120 km s^{-1}. The second order speeds at 20 Rs and the final height are 1390 and 1499 km s^{-1}, respectively. The height-time profile shows that the PCME has a clear acceleration in the LASCO FOV, somewhat similar to CMEs associated with quiescent filament eruption (Gopalswamy et al. 2015a). The acceleration is about 54 m s^{-2}, consistent with the large shock formation height indicated by the lack of metric type II radio burst. A close examination of the solar source revealed that a filament immediately to the north of the active region erupted and became part of the PCME.

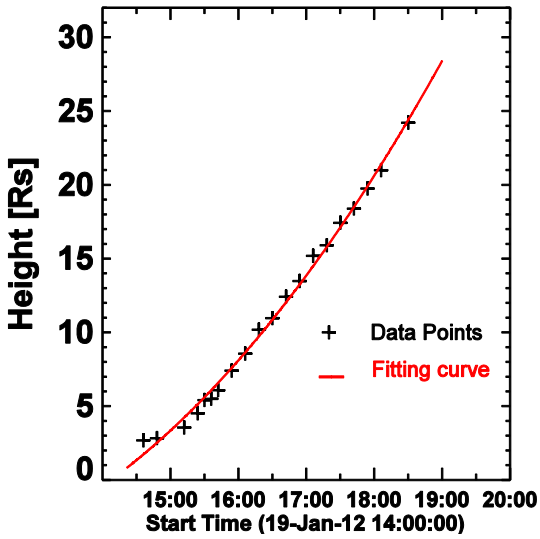

Figure 2.4. The height-time profile of the primary CME in the LASCO FOV extracted from CDAW CME Catalog. A second order polynomial fit (red) is used to the height-time measurements.

The LASCO measurements of the PCME are made in the sky plane, so they are subject to projection effects. Fortunately, the PCME is a limb event in STEREO-B view, so we are able to track the leading edge using STEREO-B/COR1, COR2 and HI1 images to get a speed that is not subject to projection effects. We are not able to track the PCME in HI2 images because the image quality is too low.

Figure 2.5 (a-c) shows the four position angles (PAs) of 305°, 310°, 315° and 320° along which we measured the height-time (H-T) history of the PCME in STEREO-B/COR1, COR2 and HI1 images. The corresponding H-T plots are displayed in Figure 2.5 (d-g). A third order polynomial fit ($H = C_0 + C_1t + C_2t^2 + C_3t^3$) to COR1 and COR2 data points, and a linear polynomial fit ($H = C_0 + C_1t$) to the HI1, respectively are used for the PAs 305°, 310° and 315°. A second order polynomial fit ($H = C_0 + C_1t + C_2t^2$) to COR1 and COR2, and a linear fit to HI1 is suited best for the data measured along the PA 320°. C_0, C_1, C_2 and C_3 are coefficients for the fitting

polynomials. “H” and “T” are the height (in Rs) and time (in hours), respectively. The values of the coefficients and the polynomials are presented in Table 2.1.

Table 2.1 Shows the fitting polynomials with the corresponding coefficients for position angles 305°, 310°, 315° and 320°.

PA	FOV	Fitting polynomial	C_0	C_1	C_2	C_3
320°	COR1 and 2	$C_0 + C_1t + C_2t^2$	1.1	2.2	1.3	
	HI1	$C_0 + C_1t$	1.1	2.2		
315°	COR1 and 2	$C_0 + C_1t + C_2t^2 + C_3t^3$	3.0	–2.7	5.1	–0.9
	HI1	$C_0 + C_1t$	–1.1	5.7		
310°	COR1 and 2	$C_0 + C_1t + C_2t^2 + C_3t^3$	3.2	–3.1	5.2	–1.0
	HI1	$C_0 + C_1t$	–0.5	5.3		
305°	COR1 and 2	$C_0 + C_1t + C_2t^2 + C_3t^3$	2.7	-1.9	4.4	–0.8
	HI1	$C_0 + C_1t$	–1.5	5.7		

PA and FOV describe the position angle and field of view, respectively. C_0, C_1, C_2 and C_3 refer to zero, first, second and third order coefficient of the polynomials, respectively. “t” refers the time.

The corresponding speed profiles in Figure 2.6 show three phases of the PCME: the early acceleration phase followed by the deceleration phase, and finally a constant speed phase (Gopalswamy et al. 2001b). The PCME is on average moving with a linear speed of 1091, 1042, 1112 and 1255 km s^{-1} at the four measured PAs 305°, 310°, 315° and 320°, respectively. The

feature tracked at the PA 320° has the highest speed indicating that the section of the PCME at this PA should be the nose of the PCME. The PCME has a peak speed of 1584 km s^{-1} at 16:39 UT in the COR2 FOV at this PA. Note that this time of peak speed is almost 2 hours after the first appearance of the PCME in the LASCO FOV. When the PCME attained its peak speed, it is at a heliocentric distance of 13.1 Rs. The speed might be a little over estimated because it assumes similar acceleration as in the low heights in COR1 and COR2. The result is consistent with the second order speeds 1390 and 1499 km s^{-1} at 20 Rs and the final height, listed in the CDAW CME Catalog if we allow the projection effects. We use the height and speed of the PCME at PA 320° for the radio source analysis. The in-situ shock speed measured by Wind at 1 AU is 408 km s^{-1} (SOHO/MTOF), suggesting a significant deceleration of the PCME beyond the LASCO FOV.

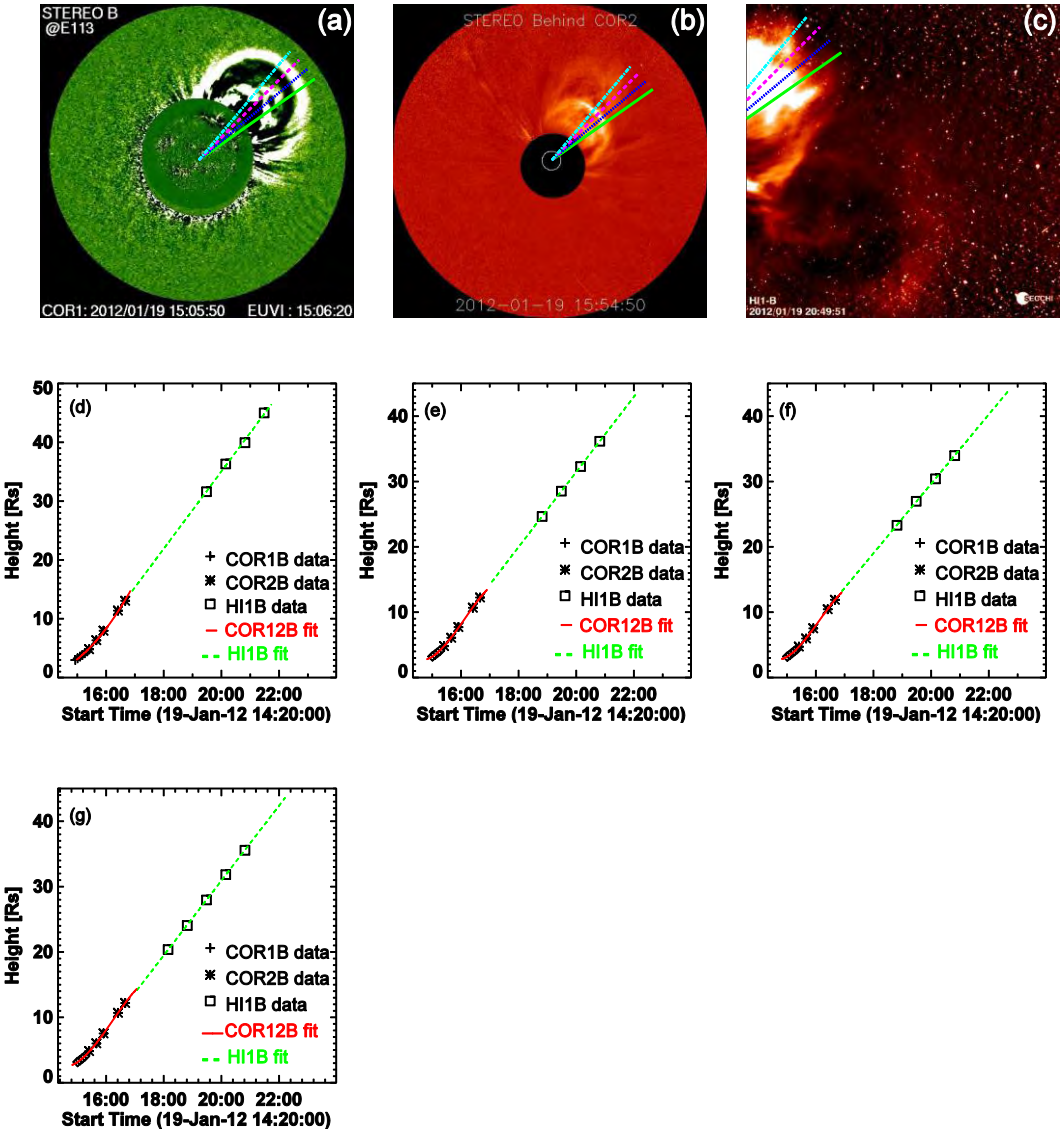

Figure 2.5. White-light images of the PCME obtained by STEREO-B COR1 (a), COR2 (b), and HI1 (c) instruments. The four lines mark the PAs 305° (light green), 310° (blue), 315° (magenta) and 320° (cyan) along which the PCME height-time measurements are made. The measured height-time profile of the PCME at the 320°, 315°, 310° and 305° position angles are shown in plots (d-g), respectively. The "+" and "*" represent COR1 and COR2 measurements, while the "□"s denote the HI1 measurements, respectively. In panel (d), the solid red curve shows the second order polynomial fit to COR1 and COR2 data and broken green line is a linear fit to the HI1 data. In panels (e), (f), and (g), the solid red curve indicates a third order polynomial fit to the COR1 and COR2 data and the broken green line a linear fit to the HI1 data.

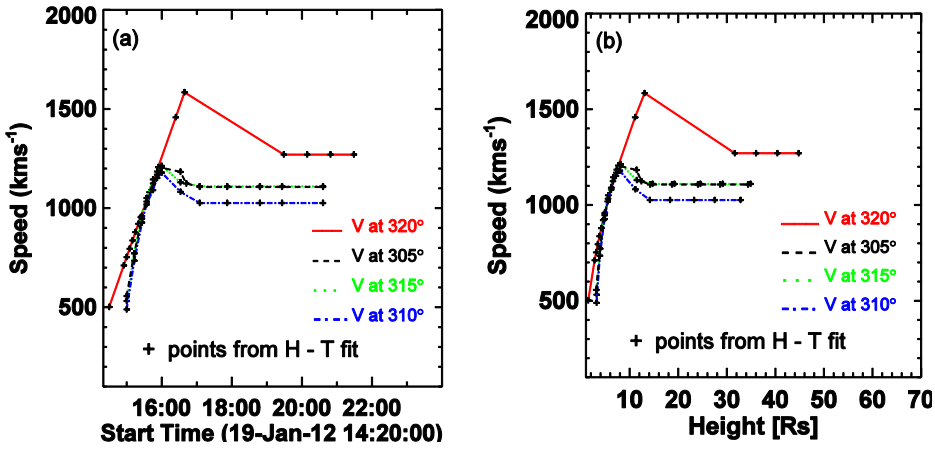

Figure 2.6. The velocity of the PCME at PAs 305°, 310°, 315° and 320° as a function of time (a) and the radial distance (b). The red, black, green and blue are the velocity profiles at 320°, 305°, 310° and 315°, respectively. The plus symbols in black correspond to the data points extracted from the fitted height-time plots in Figure 2.5. The maximum peak speed (1584 km s^{-1}) is measured at the PA 320°.

2.3.2 CME Kinematics from Radio and White-light Observations

The speed of the PCME-driven shock can be determined from the drift rate, *df/dt*, of the type II radio bursts and the density scale height (L_C) in the ambient medium. The speed corresponds to the average shock speed (V_{sh}) in a given interval of the type II burst and is given by,

$$V_{sh} = [2L_c/f_c][df/dt] \tag{2.1}$$

where f_c is the plasma frequency corresponding to the fundamental component of the type II burst at time t_c (see e.g., Gopalswamy 2011a). The heliocentric distance (r_c) of the shock at the instance (t_c) can be taken as the heliocentric distance of the PCME measured from coronagraph observations. The parameters t_c, f_c and *df/dt* can be measured from the dynamic spectrum.

The scale height L_C given in equation (2.2) obtained from the ambient density *n(r)*, which can be measured from white-light observations (details given later).

$$L_c = \{[1/n][dn/dr]\}^{-1} \tag{2.2}$$

If the density decreases with *r* as a power law,

$$n = n_o r^{-\alpha} \tag{2.3}$$

with n_0 as the density at the coronal base, one can see that

$$L_c = r_c/\alpha \tag{2.4}$$

It is known that the power-law exponent "α" ranges from six to two depending on the height of the CME. The above estimations are valid for an undisturbed ambient medium. If inhomogeneities are present, one can expect deviations from this scale height. We can also get the actual density distribution by measuring the density at various PAs and heliocentric distances from coronal images taken just before the CME eruption. The density profile can also be obtained inverting the fundamental emission frequency ($f = 9.11\ \sqrt{(n)}\ kHz$) in the dynamic spectrum using heights measured in specified PAs where "*n*" is in cm^{-3}. For each height-time data point of the CME, the corresponding fundamental emission frequency is noted from the dynamic spectrum. In this section, the speeds of the PCME and shock are compared.

The measured central times t_c, frequencies f_c, drift rates *df/dt*, heights r_c, density scale height L_c, shock (V_{sh}) and CME speeds (V_{PCME} at 320°) of the three segments (see Figure 2.1) are presented in Table 2.2. The "α" values are derived from power law density profile (see Figure 2.7) fitted to the density inverted from the fundamental frequencies of the S1, S2 and S3 of the type II burst using height measured at 320°. The derived densities can be fit to a Leblanc et al. (1998) density distribution (referred to as LDB hereafter) or a power law distribution.

The densities corresponding to the three type II segments can be fit to LDB distribution with some multipliers: 3.5, 10 and 5 for S1, S2, S3, respectively (see Figure 2.7 (a-c)). Here, we have used the basic LDB distribution because the 1-AU density is close to 7.2 cm^{-3}. The power law fits yield "α" values of 4.3, 2.9, and 1.5, respectively for S1, S2 and S3 with $n_o = (3 - 7) \times 10^7\ cm^{-3}$ for S1 and S2 but $n_o = 3 \times 10^5\ cm^{-3}$ is for S3 (see Figure 2.7 (a-c)).

Table 2.2 The measured parameters corresponding to the three segments (Segment 1, 2 and 3) of the complex type II burst.

λ	t_c	f_c	df/dt	N	α	r_c	L_C	V_{sh}	V_{PCME}
S1	15:05	~ 5.97	~ 4.8×10^{-3}	~ 4.4×10^5	~ 4.3	~ 3.45	~ 0.8	~ 902	~ 795
S2	15:20	~ 5.2	~ 1.4×10^{-3}	~ 3.3×10^5	~ 2.9	~ 4.7	~ 1.6	~ 609	~ 938
S3	19:42	~ 0.38	~ 1.6×10^{-5}	~ 1.75×10^3	~ 1.5	~ 33.1	~ 22.1	~ 1266	~ 1270

(λ) referes wavelength. S1, S2 and S3 refer to Segment 1, Segment 2 and Segment 3, respecrively.

(t_c) refers to the central time of S1, S2 and S3 in UT.

(f_c) refers to the average frequency in each segment (S1, S2 and S3) in MHz.

(df/dt) refers to the drift rate of the bursts in each segment in MHz s^{-1}.

(n) density in cm^{-3} and (α) is alpha determined from the height of the PCME using power law in this case.

(r_c) is the PCME height in Rs at t_c and (L_C) is the scale height in Rs at r_c.

(V_{PCME}) and (V_{sh}) are the PCME and associated shock speeds in km s^{-1}, respectively.

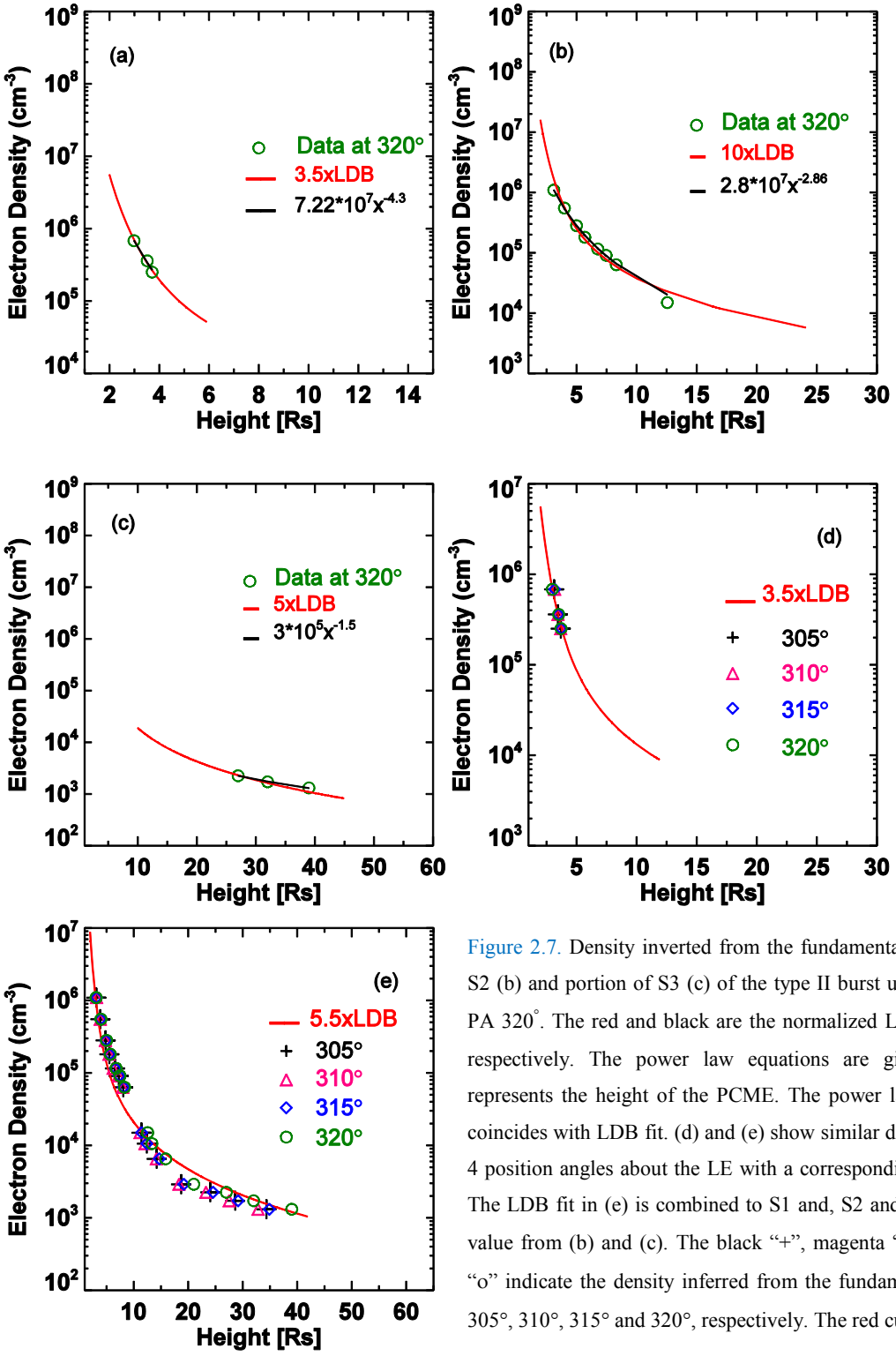

Figure 2.7. Density inverted from the fundamental frequencies of S1 (a), S2 (b) and portion of S3 (c) of the type II burst using height measured at PA 320°. The red and black are the normalized LDB and power law fits, respectively. The power law equations are given on the plot. "x" represents the height of the PCME. The power law fit is invisible since coincides with LDB fit. (d) and (e) show similar densities but they include 4 position angles about the LE with a corresponding normalized LDB fit. The LDB fit in (e) is combined to S1 and, S2 and S3 which has different value from (b) and (c). The black "+", magenta "Δ", blue "◊" and green "o" indicate the density inferred from the fundamental frequency at PAs 305°, 310°, 315° and 320°, respectively. The red curve is the LDB fit.

The derived "α" values are consistent with the typical values expected in the DH and km wavelength domains (see Gopalswamy 2011a). In the km domain, the normal density distribution should yield $\alpha \sim 2$. Here we get $\alpha = 1.5$, suggesting that the density variation is gradual. This is a clue that the CME-driven shock may be passing through a preceding CME and hence the deviation from the normal solar wind. The different "α" values for S1 and S2 suggest that they must be coming from different regions because the density fall-off is different.

The shock and PCME speeds estimated from radio and white-light observations for S1 are consistent. The result indicates that the nose region might be the source of S1. Images from STEREO/COR1 when compared with the radio dynamic spectrum from S/WAVES shows that the radio burst starts and ends when the PCME is within the COR1 FOV in the height range 3.2–3.7 Rs. Interestingly, this height range corresponds to the peak in the Alfven speed profile of the corona (Mann et al. 1999; Gopalswamy et al. 2001c). Therefore, the PCME is barely super-Alfvenic at the time of S1. Note that the PCME is still accelerating around this time and reaches its peak speed an hour later. This means S1 ends mainly because it could not remain super-Alfvenic because the speed increase is not fast enough to overcome the increase in Alfven speed with heliocentric distance. The nose region is also consistent with the fact that the burst is seen at all three views (SOHO and STEREO) because the PCME body poses less obstruction to the burst.

On the other hand, the speeds derived from S2 and S3 are inconsistent. So, the nose may not be the source of S2 and S3. S1 and S2 have similar frequencies but the speed comparison implies that the source of S1 should be at the nose but a different source location from S2. Most likely the S2 comes from a region where the Alfven speed is still low and hence the PCME remains super-Alfvenic to continue and produce S3. Such a situation is possible at the shock flank, which is at a lower heliocentric distance and hence lower Alfven speed. The lower Alfven speed can also result when the shock flank passes through a denser region, for example, provided by the eastern flank of CME2. In order to confirm this interpretation, we use a different technique in the next section and compare the results given in Table 2.2.

2.4 Coronal Density from the Polarized Image and from the Type II Radio Burst

We use polarized brightness (pB) images available from

http://lasco-www.nrl.navy.mil/content/retrieve/polarize and invert the pB profiles into density profiles with the Solar Software routine "pB_inverter" (Thernisien and Howard 2006; Cho et al. 2007). We use the pB images from LASCO/C2 and STEREO-B/COR1 for the density estimation in the region we are interested in. The pB image taken by STEREO-B/COR2 has calibration issues and hence is not useful. The PCME is a backside event to STEREO-A. We normalize the LDB density model with the density estimates from pB images to extrapolate the density to distances outside the region for which the pB technique is used.

The density profile from the pB technique is compared with the density profile found by inverting the frequency of type II emission at various position angles covering the span of the PCME. We compared the iso-density contours of the pre-event corona with the white-light image of the PCME to identify the plausible location of radio emission. We searched for a section of the PCME (shock) traversing the plasma density level having a density equal to the one obtained by inverting the frequency of the type II burst (e.g., Reiner et al. 1998).

In this section, first, we invert the frequency of type II burst using the heights of the PCME at the four position angles in subsection (2.4.1). Second, we investigate the density profile of the ambient medium (background) using the pB images in subsection (2.4.2), and (2.4.3). In subsection (2.4.4), the two results obtained in subsection (2.4.1) and the next two results from subsections (2.4.2) and (2.4.3) are compared for possible radio source location. Finally, the results from the superposed images of iso-density contour plot and white light images are presented in subsection (2.4.5).

2.4.1 Coronal Density Inverted from the Type II Radio Burst

The plasma density corresponding to the fundamental plasma frequency is plotted as a function of the PCME height in Figure 2.7 (d) and (e). The derived plasma densities for S1 and, combining S2 and S3 correspond to a 3.5 × LBD and 5.5 × LDB density model, respectively as indicated by the fit. The fitted line represents the average density variation in the corona in the 20^{o} PA swath of the corona from PA=305° to PA=320^{o}. In the next two sections, the density traversed by the PCME is measured from the pB images of C2 and COR1-B. If the densities match at the position angle of interest, then the nose region of the PCME is the radio source location.

2.4.2 pB Inversion of the LASCO/C2 data

The PCME occurred at E22° on 2012 January 19. So, the corona overlying the PCME should have been above the east limb on 2012 January 13. The C2 pB image at 02:57 UT 2012 January 13 is u0sed to make 24 density measurements at PAs ranging from 110° to 355° in steps of 5° (anti-clockwise). The measurements at the PAs 5°, 10°, 15°, 60° and 65° are rejected since the inverted pB have unrealistic profiles. The measured densities correspond to 1 × LDB at most PAs except at PAs 55° (0.9 × LDB) and, at PAs 70°, 75°, 80°, 90° and 95° (1.4 × LDB). The coronal densities obtained from the pB inversion and from the LDB model fitting to the pB data are displayed in Figure 2.8 (a) and (b), respectively. One should note that the C2 pB image is obtained about eight days apart. The corona might have also evolved over this interval.

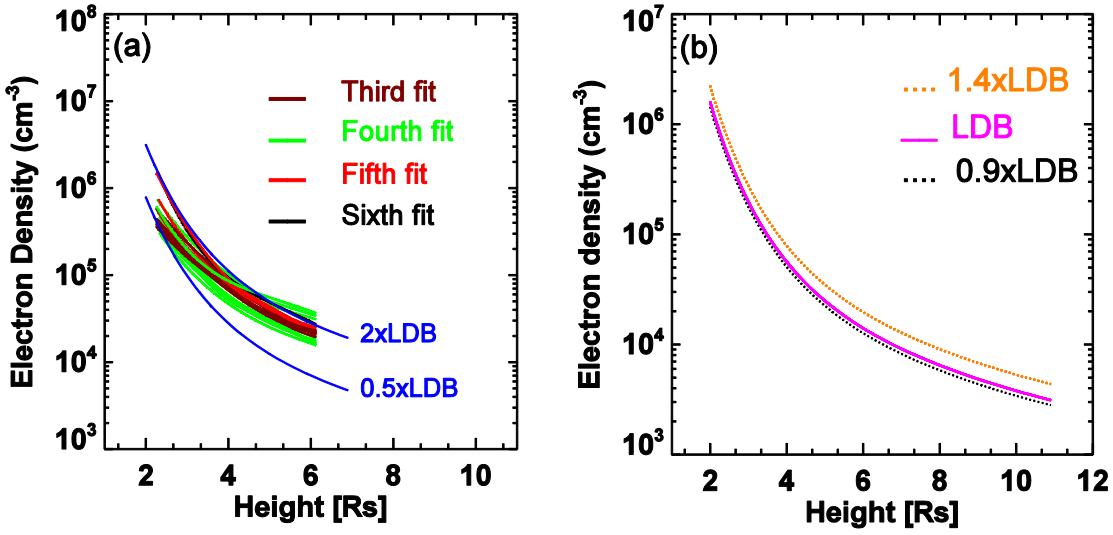

Figure 2.8. (a) The density profile of the background corona using the C2 pB image on 2012 January 13 at 02:57 UT and pB_inverter code provided by Solar software package at PAs from 110° to 355° in 5° steps. The IDL program fits an nth order inverse polynomial fit to the pB data. The maroon (5 PAs), green (9 PAs), red (4 PAs) and black (1 PA) lines represent the inversion using 3rd, 4th, 5th and 6th order inverse polynomial fits. PAs with similar multiplier are combined. The densities obtained from the pB data lie between 0.5 and 2 times the LDB model (blue lines). (b) The LDB model curves normalized to the actual densities from the curves in (a). Each density profile in (a) is fitted to a normalized LDB model curves. Similar to (a), PAs with similar multiplier are combined. The three curves correspond to orange, magenta and black lines represent 1.4 × LDB (5 PAs), 1 × LDB (13 PAs), and 0.9 × LDB (1 PA). The fitted curves extend the densities into heliocentric distances not covered by coronagraph images.

2.4.3 pB Inversion of the COR1-B data

The background corona on 2012 January 19 at 08:50 UT (COR1-B) is relatively undisturbed. As in the C2 image, we made 24 density measurements along the PAs from 5° to 250° in steps of 5° (clockwise). The density profiles from the pB inversion and the corresponding LDB model

densities are displayed in Figure 2.9 (a) and (b), respectively. The data at PAs 295°, 300°, 350°, 355° and 360° are rejected because the inversion of the pB profiles is unrealistic. Densities at PAs 5° and 345° match with 0.4 × LDB and 0.45 × LDB, respectively. Densities at PAs 330° and 325° match with 0.7 × LDB. The densities along 10 PAs (250°, 255°, 260°, 270°, 305°, 310°, 315°, 320°, 335° and 340°) correspond to the 1 × LDB model. The density along the remaining 5 PAs (265°, 275°, 280°, 290° and 285°) are best fit with 1.2 × LDB, 1.2 × LDB, 1.6 × LDB, 1.8 × LDB and 2 × LDB, respectively. The PAs 5° and 345° correspond to the polar region where densities are low. Compared to the C2 density profiles, the density profiles of COR1-B are more dispersed.

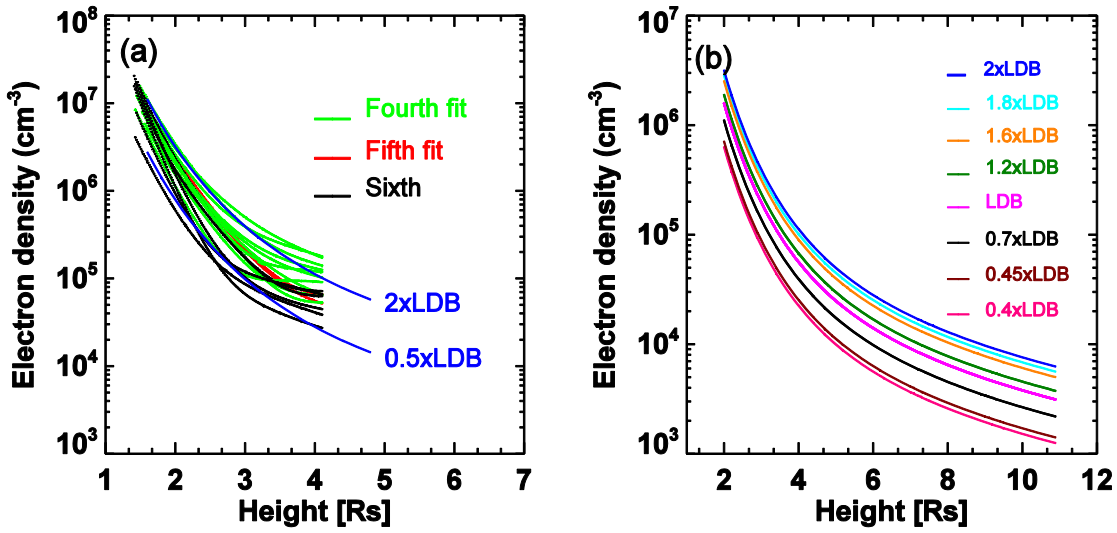

Figure 2.9. (a) The density profile of the normal corona on 2012 January 19 at 08:50 UT from COR1-B. The colors are same as in Figure 2.8. In (a) 11 lines are green, 2 lines are maroon and 6 lines are black. The density ranges from 0.5 × LDB – 2 × LDB. (b) LDB model curves consistent with the densities in (a) obtained from pB inversion. The density multipliers for various lines are noted on the plot.

2.4.4 Comparison of Coronal Density Inverted from Radio Emission and pB White-light Images of COR1-B and C2

From Figures 2.8 and 2.9, the normalizing factor varies from 0.7 to 1.2 on C2 and 0.4 to 2 on COR1-B. From Figure 2.7 (d) and (e), the estimated value of the LDB normalizing factor is 3.5 and 5.5 for the S1, and S2 and S3, respectively. Except for S1 (close LDB value), none of the four PAs from Figures 2.8 and 2.9 has the density profile estimated in Figure 2.7 (d) and (e). The density obtained from the pB images is generally lower than what is required for the type II burst to occur at the nose. This can be resolved if we note the fact that the pB inverter routine assumes a spherically symmetric corona, which might underestimate the local density. Furthermore, the line of sight depth may also be overestimated, giving an underestimate of the density. We suggest that these two factors account for the discrepancy between the density profiles derived from radio and pB inverter. This would have been a problem if the density derived from the pB images is larger than that from the radio dynamic spectrum. Hence the radio source region for S1 should be near the PCME nose. The difference for S2 and S3 implies that a shock section at these locations should not produce the type II emission. The result for S2 and S3 is consistent with results in section 2.3.2. The density multipliers for the density profile from pB at the position angles spanning the interaction regions of the PCME both in C2 and COR1-B are small compared to the results inferred from the type II burst. This may imply that the radio source has a non-radial motion at these position angles. In the next section, the radio source is identified using a different technique for all segments.

2.4.5 Radio Source Location Using Iso-Density Contour plot

2.4.5.1 DH Type II Burst (S1)

The radio source location for S1 is estimated by superposing the COR1-B difference images over the iso – density contour plots of the corona from pB white-light images. The density level that is equivalent to the one inverted from the type II burst and is traversed by the PCME at a given time is searched for in the combined image (see e.g., Reiner et al. 1998). The white-light difference images at times15:00, 15:05 and 15:10 UT are important for this purpose. The times of the type II, of S1, fundamental frequency measurements and the corresponding inverted densities are at 15:00, 15:05, 15:06 and 15:10 UT and 6.8×10^5, 4.4×10^5, 3.6×10^5 and 2.5×10^5 cm^{-3}, respectively. The density at 15:05 UT corresponds to the central frequency mentioned in Table 2.2. The source regions of these densities are assessed as follows. The density at 15:00 UT is indicated in magenta contour iso-density level in Figure 2.10 (a). Equivalently, the type II emission at 15:05 and 15:06 UT are indicated in black and magenta iso-density contour plots in Figure 2.10 (b), respectively. The density contour at 15:10 UT is indicated in magenta iso-density contour level in Figure 2.10 (c). None of the four iso-density contour plots are traversed by the nose. However, if we account for the possible density underestimate from the pB images described in the previous subsection, the S1 source can be closer to the PCME nose.

2.4.5.2 DH-km Type II Burst (S2 and S3)

In this subsection, the technique we use is similar to section 2.4.5.1 except the COR1-B, COR2-B and HI1-B white light images are used. The COR2-B white-light images used here are the direct. Polarized brightness (pB) density profiles in COR2-B and HI1-B are used by interpolating the COR1-B LDB fits. The COR1-B frames at 15:00, 15:05, 15:10 15:15, 15:25 and 15:35 UT are used. The times of the type II burst, of S2, fundamental frequency measurements and the corresponding inverted densities are at 15:00, 15:13, 15:26, 15:34 and 16:53 UT and 10^6, 5.5×10^5, 2.8×10^5, 1.8×10^5 and 8.4×10^3 cm^{-3}, respectively. The time and density at the central

point (see Table 2.2) are at 15:20 UT and 3.3×10^5 cm^{-3}, respectively. The time and density at the time closer to the PCME frame are at 15:53 UT and 2.8×10^4 cm^{-3}, respectively.

Considering the 15:00 UT frame in Figure 2.10 (a), the type II emission corresponds to a local plasma density of 10^6 cm^{-3} indicated in black iso-density level indicate that the PCME nose does not cross this region at that time. Similarly at about 15:15 UT, type II emission should originate

from 5.5×10^5 cm^{-3} dense corona and the PCME nose does not pass through this region as indicated in black iso-density contour plot in Figure 2.10 (d). The next frame at 15:25 UT in Figure 2.10 (e) shows that the source region corresponding to a coronal region with a density of 2.8×10^5 cm^{-3} as indicated in black iso-density contour plot and again the PCME nose does not cross it. The frame at 15:35 UT in Figure 2.10 (f) further strengthened the above results, because the black iso-density contour plot containing density equal to the one inferred from the type II frequency, 1.8×10^5 cm^{-3}, does not pass through the nose. Analysis of source identification using the above technique could not precede further especially for the COR2-B using the pB images. We interpolate the fitted LDB results presented in section 2.4.3 but for wider position angles spanning the PCME in COR2-B and HI1-B. The COR2-B frame at 15:24 UT and the density corresponding to the central frequency, at 15:20 UT and 3.3×10^5 cm^{-3}, is displayed in Figure 2.10 (g). Consistent with the above results, the nose does not pass through this interpolated iso-density contour plot. Rather the density level is in the region of the corona occulted by the occulting disk. Of course the interpolated contour plot might be a little underestimated due to the LDB fit. The next frame at 15:54 UT in Figure 2.10 (h) shows that the section of the PCME traversed by a density level of 2.8×10^4 cm^{-3}. In all the frames, the nose does not traverse the iso-density contour plots. The results found in subsection 2.4.4, assuming the nose as the source of the S2 emission, showed that the densities inferred from the type II burst (S2) and from pB image are unequal and the implication is that the nose should not be the source which is in agreement with the result in this section.

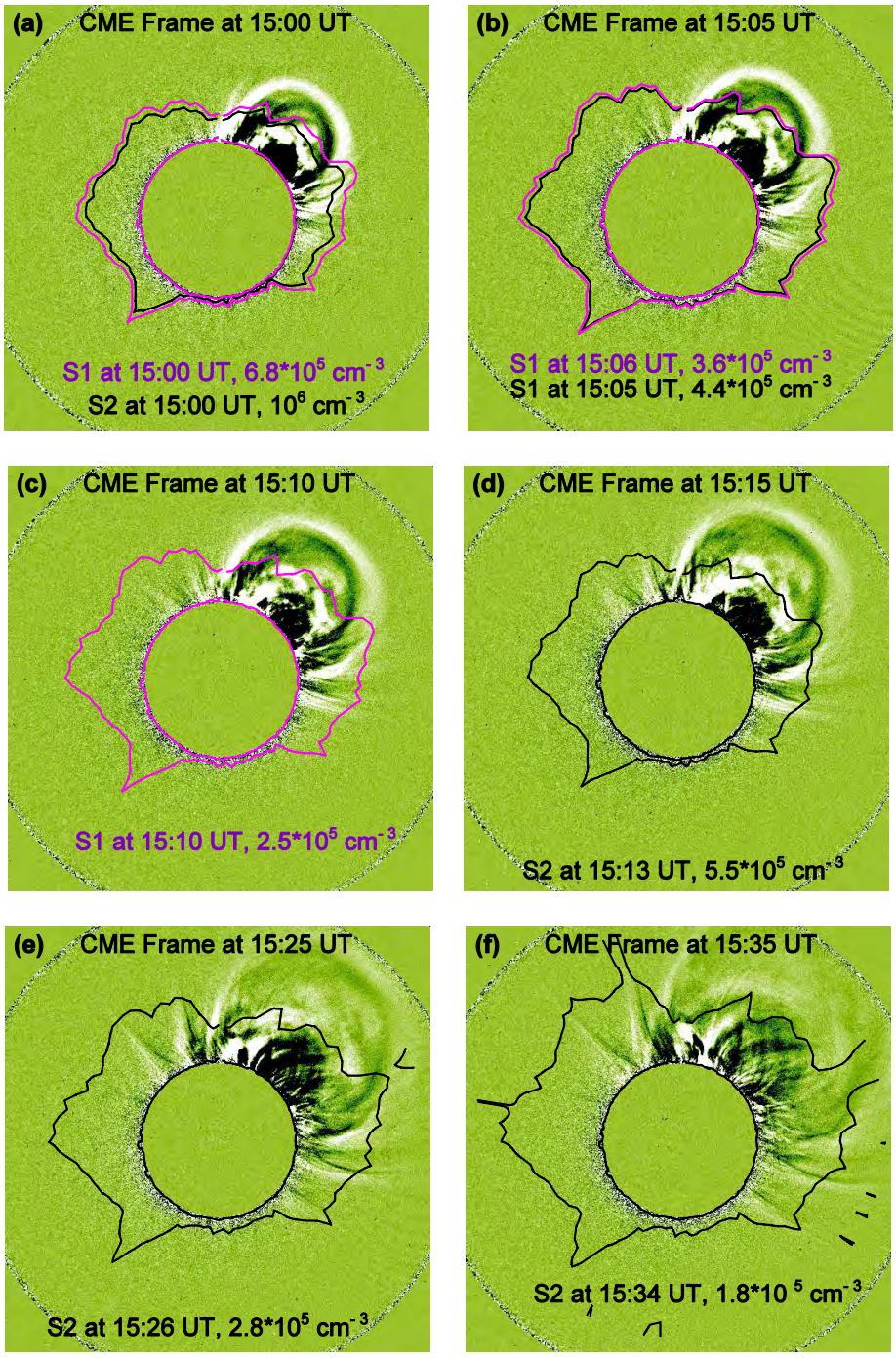

* The caption for the above images is presented in the next page (Figure 2.10).

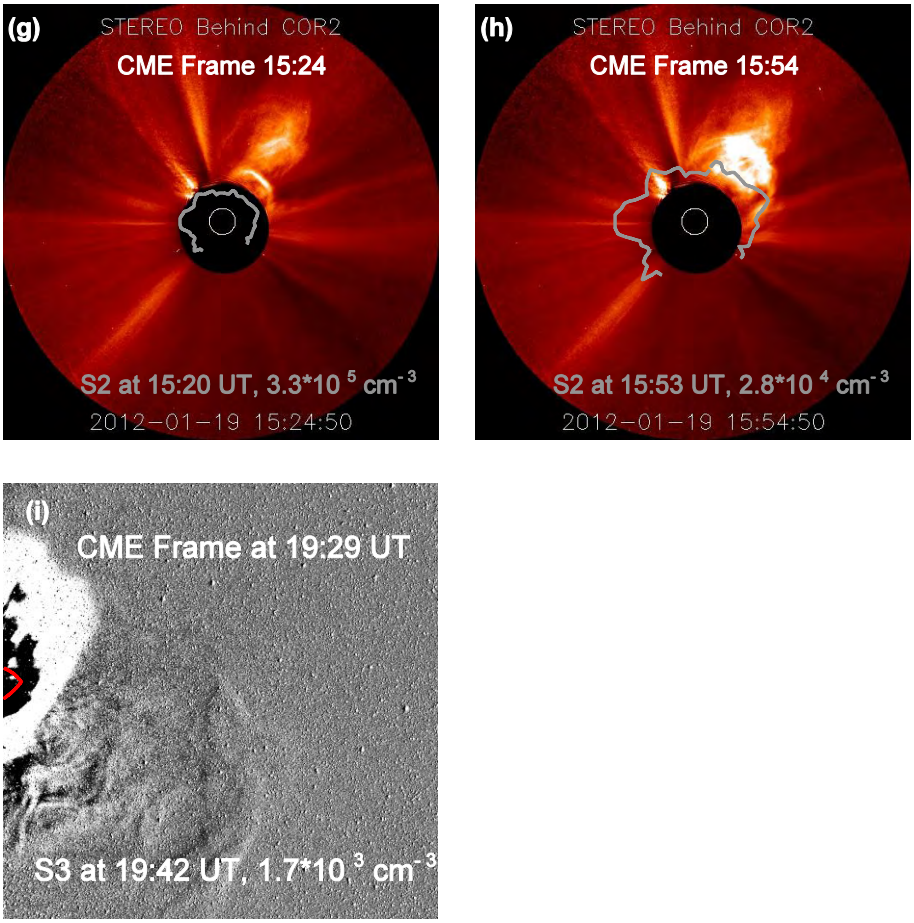

Figure 2.10. In (a-f) the locations of the radio sources are identified using COR1-B CME white-light difference images over-plotted by iso-density contour (magenta and black) levels inverted from the COR1-B pB images equal to the density inferred from the fundamental frequency of the type II bursts. The time of the PCME image and type II frequency measurement together with the corresponding coronal density value are shown on the image. The magenta contours in (a-c) and black in (b) indicate the density inverted from S1 while the black in (a) and (d-h) refer to S2. (i) Refers to S3. The density contour in COR2-B (in cyan) and in HI1-B (in red) are interpolated from COR1-B pB measurements at PAs 235°–140° (anti-clock wise). The density corresponding to each contour level is displayed in each panel. The PCME images in (g) and (h) are direct and the contour plots correspond to density levels at the central frequency of S2 specified at 15:20 and 15:53 UT, respectively. The contour plot in (i) corresponds to density level inferred from the central frequency of S3 specified in Table 2.2.

Figure 2.11 shows the height-time plots of the PCME, CME1, CME2 and CME3. The PCME has the largest speed compared to all the preceding CMEs. The linear speeds in the LASCO FOV are 1120, 119, 317 and 267 km s^{-1} for the PCME, CME1, CME2 and CME3, respectively. The PCME first overtakes the CME1 and simultaneously interacts with the CME2. A clear PCME-CME2 interaction at the flank and extending near the nose is observed in C2 (see Figure 2.3 (b)) simultaneously (both spatially and in time) with the radio enhancement in S2. It occurs within C2 FOV and in the time of S2. This would show that the region of the PCME above the flank should be the source.

Using the interpolated density profile from COR1-B, the iso-density contour inferred from the type II burst (S3) is plotted in Figure 2.10 (i). It shows that the nose of the PCME at 19:29 UT does not pass through a density inferred at 19:42 UT (1.7×10^3 cm^{-3}). The contour is neither traversed by the nose nor by the flank. The LDB fit at this range is underestimated since it is at larger distances. Using simultaneous observations of the white-light enhancement of the PCME in HI1-B and the corresponding radio signatures in the kilometric segment of the emission in Wind WAVES, the possible radio source might be proposed. A clear enhancement and shift in frequency from 0.37 to 0.42 MHz at 20:09 UT is observed in the dynamic spectra is S3. A wide interaction region between PCME and CME3 is observed in HI1-B as can be seen in Figure 2.3 (c). The region which extends further above the flank seems to be the best candidate for the source. This is in line with results found in sections 2.4.1, 2.4.2 and 2.4.3.

S4 is also part of this DH-km type II burst. At this range, there is no more fundamental-harmonic structure. At larger distances in the interplanetary medium, the shock becomes weaker and the emission may be coming from narrower regions. Further investigation is needed to understand such a transition.

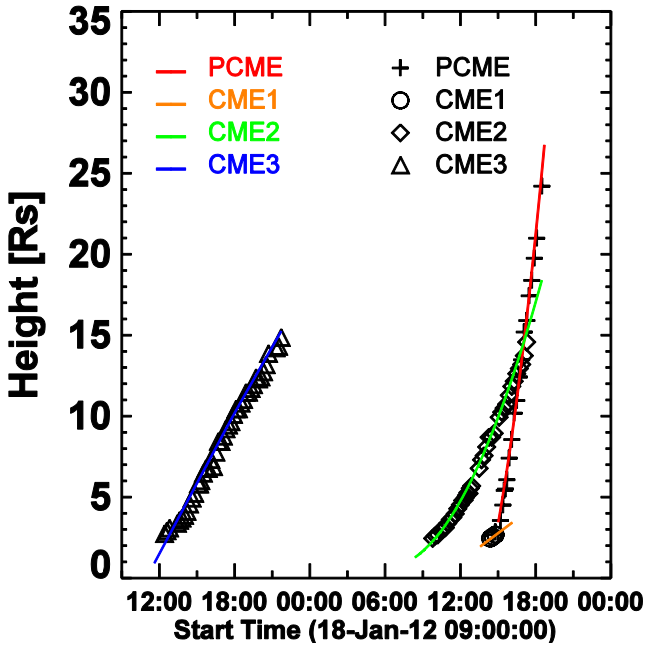

Figure 2.11. The height-time profiles of the primary CME and the 3 preceding CMEs from CDAW CME Catalog. The "+", "o", "◊" and "Δ" represent the data points of PCME, CME1, CME2 and CME3, respectively in the LASCO FOV. The blue, green, red and orange fits correspond to CME3, CME2, PCME and CME h-t data points, respectively. All lines are second order fits to the measurements.

2.5 Conclusions

The complex type II burst on 2012 January 19 can be understood as a consequence of the interactions of the energetic primary CME with preceding CMEs and the relative increase between the Alfven speed and the CME speed. Furthermore, the radial density profile is also different at different source locations. The CME interactions cause deviations from the normal coronal scale heights, which also contributes to the observed complexity.

The fastest part of the leading edge of the PCME is found to be at the PA 320°. This nose region is propagating at a speed of 1255 km s^{-1} based on the height-time measurements of the PCME

from STEREO-B/COR1, COR2 and HI1. The PCME is driving a strong shock that is responsible for the entire type II emission. However, the shock forms only when the PCME is at a height of ~3 Rs, very similar to filament eruption events. The short-lived, fast drift S1 seems to be produced near the nose of the PCME when it is between 3 and 4 Rs. S2 seems to be produced from a different location (above the flank), where the Alfven speed is lower because of passage through a dense region associated with a preceding CME. The PCME also became faster, so the super-Alfvenic condition always matched for S2 and eventually S3. The start of S1 and S2 overlap in time but differ in frequency and in the drift rate of the frequency. The Segment 2, 3 and 4 are consistent with the known fact that fast and wide CMEs produce long-duration type II bursts (Gopalswamy 2006). The normal coronal density, used for the investigation of the location of the type II radio source, is obtained from the inversion of pB white-light images of COR1-B and C2. We use different techniques in identifying the source of the radio bursts: CME and shock speed comparison from type II burst using power law density distribution, inversion of frequency of emission of the type II burst, pB inversion, LDB density model, combination of iso-density plots with white-light images, and considering CME-CME interaction observed in white light images consistent with the radio enhancement. The double type II bursts and the different density scale-height requirements of S1 and S2 are not in agreement with the results by Liu et al. (2013). The main difference is that they overlook the details of the radio dynamic spectrum. Basically, they did not consider the two separate F-H structures (S1 and S2). The Leblanc density model is valid for an undisturbed corona but clear CME-CME interaction in the white-light images and interaction signatures in the radio dynamic spectrum are observed.

Chapter 3

A Diffuse Interplanetary Radio Emission Observed by the Wind/WAVES Instrument

We report on an unusual drifting feature in the radio dynamic spectrum at frequencies below 14 MHz observed on 2001 September 27 by the Radio and Plasma Wave (WAVES) experiment on board the Wind spacecraft. We call this feature "Diffuse Interplanetary Radio Emission (DIRE)". The DIRE drifts like a type II burst in the dynamic spectra, but the drifting feature consists of a series of short-duration spikes (similar to a type I chain). The DIRE is observed at higher frequencies than the associated type II burst, with no harmonic relationship with the type II burst. The onset of the DIRE is delayed by ~2 hours from the onset of the regular type II burst. Comparing the shock and CME speeds, the densities derived from the polarized brightness (pB) images and the radio emission frequency, we infer that the DIRE source is located at the flank. We discuss the implications of this event for electron acceleration by CME-driven shocks.

3.1 Introduction

White-light observations from SOHO/LASCO and the low-frequency radio observations from Wind/WAVES have provided important information on phenomena in the outer corona and near Sun-IP medium because of the overlap of the spatial domain probed by these missions. For example, radio emission due to the interaction between CMEs is discovered by such combination of observations (Gopalswamy et al. 2001a; 2002; Gopalswamy 2004a).

On 2001 September 27 the Wind/WAVES observed an unusual drifting radio emission associated with a regular type II burst at frequencies below 14 MHz. The feature occurs at a frequency much higher than that of the associated type II burst. We call this faint feature "Diffuse Interplanetary Radio Emission (DIRE)". The drifting feature consists of a series of

short-duration spikes (similar to a type I chain). We identify the source of this radio emission and discuss the possible mechanisms that produce it.

3.2 Observations

3.2.1 Radio Observations

The DIRE occurred on 2001 September 27 accompanying a regular type II burst observed by Wind/WAVES (see Figure 3.1). The Wind/WAVES receivers measure radio emission at frequencies less than 14 MHz covering a range from decameter-hectometric (DH) to kilometric (km) wavelengths. The regular type II burst has a clear F-H structure but DIRE is at a much higher frequency. DIRE roughly starts at 10:23 UT at a frequency of ~11.4 MHz and is clearly observable down to 1.6 MHz. It extends to lower frequencies but the interference of a type III storm makes it difficult to observe it below 1.6 MHz. The accompanying type II burst is observed from ~8:20 UT, starting at a lower frequency. When the regular type II burst is at 0.8 MHz, the DIRE is at an order of magnitude higher frequency (~10 MHz), confirming that there is no harmonic relationship between the DIRE and the regular type II burst. The average drift rate of DIRE is 3.8×10^{-4} MHz s^{-1} in the 10.2–2.4 MHz range. The regular type II burst drifts by 3×10^{-5} MHz s^{-1} over a similar time range. The DIRE has slightly larger drift rate, but lower intensity than the regular type II. Eventually, their gap in frequency narrows.

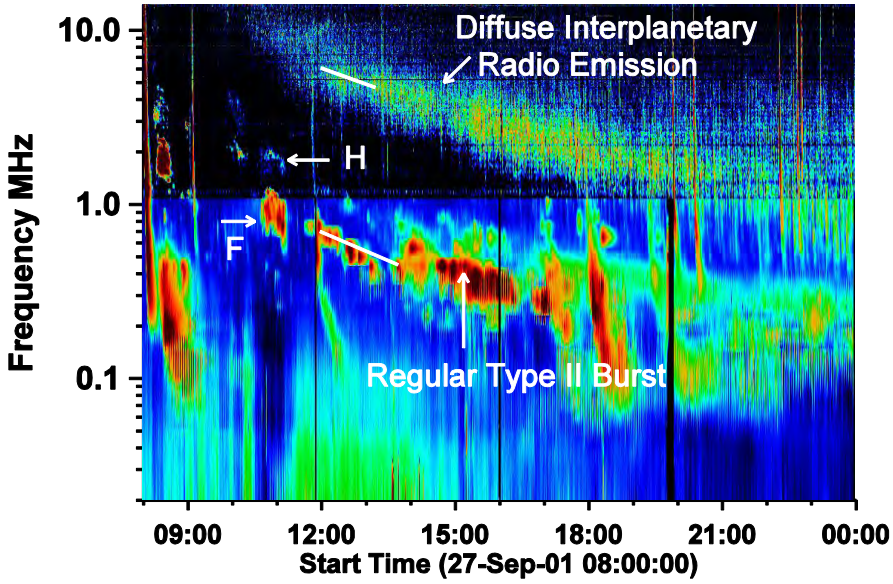

Figure 3.1. Wind/WAVES dynamic spectrum showing diffuse interplanetary radio emission or DIRE (upper diffuse drifting feature) and the associated regular type II burst (lower more intense feature). "F" marks the fundamental and "H" the harmonic component of the regular type II burst. The two white lines drawn on the DIRE show the sections of the dynamic spectra used for shock-speed computation in section 3.3.2.

3.2.2 White-light Observations and the Solar Source

A partial halo CME is detected in white-light images obtained by SOHO/LASCO in association with the type II burst. The CME erupted from a filament channel ~10° to the west of AR09626 (S18W39) seen in SOHO"s Michelson Doppler Imager (MDI) magnetogram shown in Figure 3.2 (a) and (b). Hα pictures indicate that there is no filament in the channel. It is associated with a post eruption arcade (PEA) observed by Yohkoh by soft X-ray Telescope (SXT) (see Figure 3.2 (c)). In the LASCO/C2 image at 08:54 UT (Figure 3.2 (d)), the leading edge (LE) of the CME causing the emission has already left the FOV. All we see is the CME core, which is faint in C2. The CME core seems to be the mass from the filament channel. The CME is clearly observable in C3 FOV with its core (see Figure 3.2 (e)). The CME is associated with a long-duration GOES

C9.5 flare shown in Figure 3.2 (f). There are two CMEs preceding this primary CME (PCME): CME1 observed at 01:31 UT (PA ~204°) originating from S23W20 and CME2 merging with western leg of the PCME by the time it reaches the LASCO/C3 FOV. CME1 is seen ahead of the LE of the PCME in C3 FOV. Some of the intensity fluctuations observed in the Wind/WAVES dynamic spectrum seem to be due to the interaction of the PCME with these preceding CMEs (Gopalswamy et al. 2001a). Figure 3.3 (a) shows a bright streamer at the western flank of PCME. A clear deflection of the streamer in Figure 3.3 (b) indicates that the flank of PCME shock passes through the streamer.

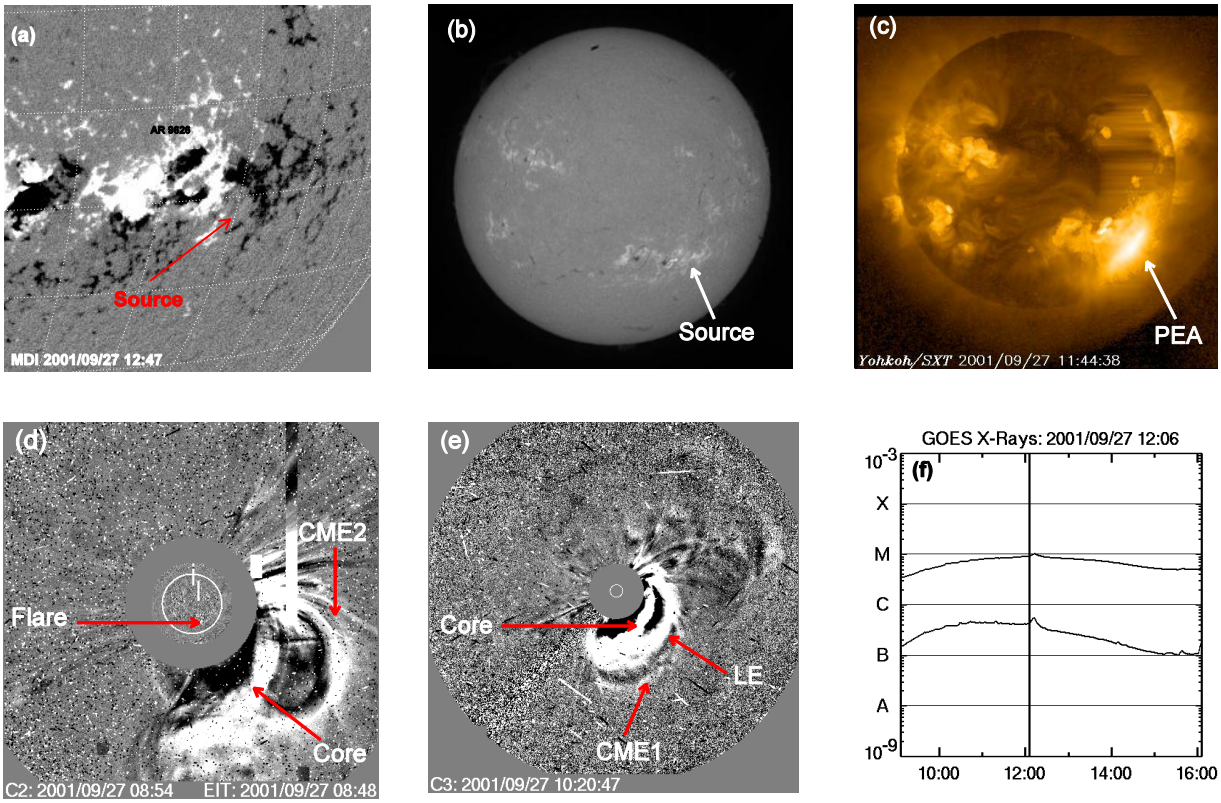

Figure 3.2. (a) MDI magnetogram at 12:47 UT is taken from Solarmonitor.org, (b) Hα image from Kanzelhoehe Solar Observatory at 6:27 UT, (c) Yohkoh soft X-ray (SXT) image showing the post eruption arcade (PEA), (d) LASCO/C2 difference image showing the core of PCME and another CME (CME2); the flare location is indicated in the superposed EUV difference image from SOHO"s Extreme Ultraviolet Imaging Telescope (193 Å), (e) LASCO/C3 image at 10:20 UT showing the PCME core and leading edge (LE) along with another preceding CME (CME1), and (f) GOES soft X-ray flare with the approximate peak time marked by the vertical line; the upper and lower curves correspond to 1–8 Å and 0.5–4 Å.

3.3 Analysis and Interpretation

The height – time profiles of the LE and flank of the PCME are plotted in Figure 3.3 (c) and (d), respectively. The heights are determined using the white-light running difference images in C3. The measurement starts at 09:42 UT because the LE is not clear in C2 images. The LE and flank of the PCME are tracked at PAs 181° and 302°, respectively. We find that a second order polynomial is a better fit to the height-time data. This is typical of CMEs associated with filament eruption outside of active regions (Gopalswamy et al. 2015a). The LE has a relatively high de-projected linear speed of 1303 km s^{-1} (the de-projection is done according to the empirical relation derived in Gopalswamy et al. 2015b). It is still accelerating by 7.6 m s^{-2}, in the LASCO FOV. The flank of the PCME has a linear de-projected speed of 988 km s^{-1}. CME1 has a low linear de-projected speed of 515 km s^{-1} with an acceleration of ~ 7 m s^{-2}.

Since there is no other activity that can be attributed to the production of DIRE, and since it starts after the PCME with a drift pattern somewhat similar to that of the regular type II burst, we suggest that the PCME should be responsible for DIRE. In the following analysis, we provide quantitative evidence supporting this interpretation.

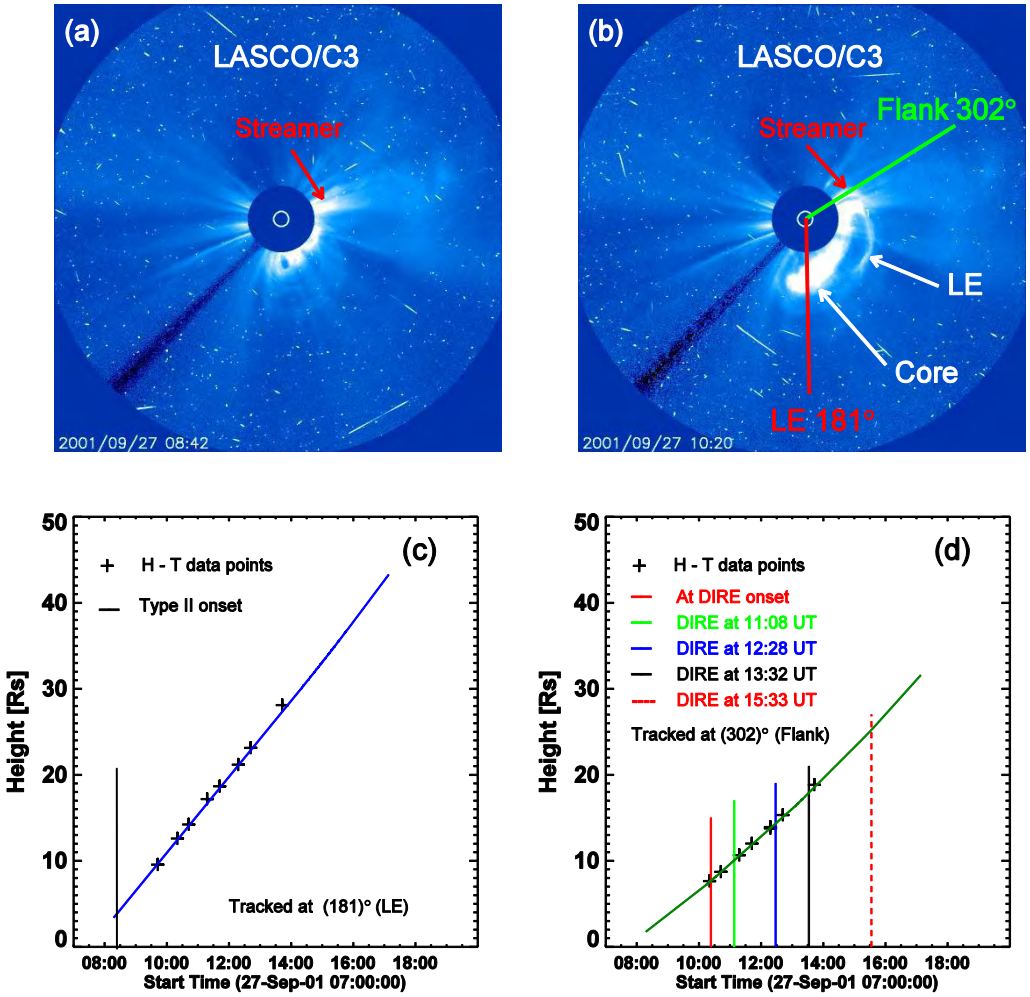

Figure 3.3. LASCO/C3 direct images at 08:42 (a) and 10:20 UT (b), showing the streamer, the PCME core, flank (Flank 302°) and the leading edge (LE 181°). The core is the brightest feature in (b). The deflection of the big streamer in (a) at the north-west quadrant is observable in (b). Height-time (H-T) measurements of the LE (c) and flank (d) made at PAs 181° and 302°, respectively. A 2nd order polynomial best fits to the H – T measurements. The black "+" symbol represents the data points. The black in (c) and red in (d) solid vertical lines indicate the onset times of the regular type II burst (08:20 UT) and DIRE (10:23 UT), respectively. The solid red, green, blue, black and broken red vertical lines in (d) indicate the flank position at 10:23, 11:08, 12:28, 13:32 and 15:33 UT, respectively described in Table 3.1.

At the type II burst onset (08:20 UT), the PCME LE is at 3.5 Rs and traveling with a de-projected speed of 1270 km s^{-1}. At the DIRE onset (10:23 UT), the PCME LE and flank are at 12.7 and 7.8 Rs, respectively. At this time, the LE and flank of the PCME have de-projected speeds of 1291 and 923 km s^{-1}, respectively. The regular type II burst occurs when the PCME LE is in C2 FOV but for DIRE the LE is already in C3 FOV. The large shock formation distance (3.5 Rs) indicated by the onset of type II burst is consistent with the slow acceleration of the PCME. Furthermore, the flare rise time is ~3 hours and 18 minutes, which when combined with the de-projected linear LE speed, 1302 km s^{-1}, yields a positive acceleration of 110 m s^{-2} (Gopalswamy et al. 2012; 2003). This is consistent with the acceleration of CMEs associated with filament eruptions from outside active regions.

3.3.1 Density in the DIRE Source Region

The LE speed of the PCME is high enough to drive a shock and produce the type II burst but the DIRE occurs at a much higher frequency. If the DIRE is due to fundamental plasma emission, its source plasma density must be accordingly higher and hence the source needs to be closer to the Sun. Such a situation is prevalent only at the western flank of the CME, where the shock seems to travel through an unusually dense streamer.

We make use of the polarized brightness (pB) images from SOHO/LASCO to get an independent estimate of the density. Inversion of pB images for the density determination is well-known (Gopalswamy and Yashiro 2011). We use the pB image obtained on the 2001 September 27. We have superposed the iso-density contour inverted from the pB image and over-plotted on the white-light image of the corona taken at 01:55 UT before the appearance of the PCME in Figure 3.4 (a) and at about the DIRE onset in Figure 3.4 (b). The streamer in the west is clearly the brightest feature in the image. Recall that the PCME flank passes through this streamer (Figure 3.3 (a)) and DIRE starts when the PCME flank is at a height of 7.8 Rs. At this height, the density is ~10^4 cm^{-3}, which corresponds to a plasma frequency of 1 MHz compared to 11.4 MHz at

DIRE onset. This means the high density prevalent in the streamer is not present during the pB measurement. This is because the streamer has been ejecting material over this period and hence has become less dense. The depth of the streamer may also be overestimated, giving a lower estimate for the density from the pB inversion.

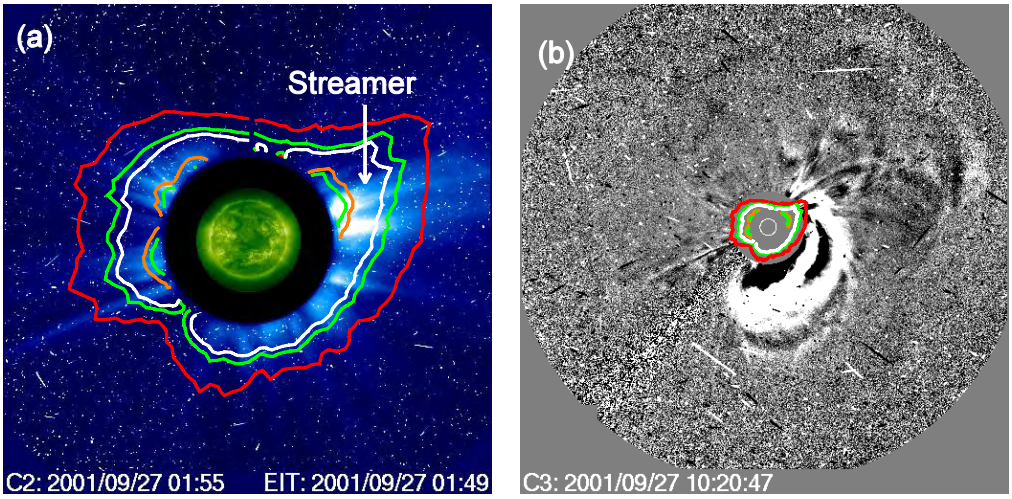

Figure 3.4. (a) and (b) The iso-density contour profile from pB image equal to the density inferred from the fundamental frequency of the DIRE over-plotted on the direct C2 PCME image at 01:55 UT and C3 PCME difference image at about the DIRE onset (10:20 UT), respectively. In (a), the density contours and the PCME image are apart for greater than 10 hours. The inner green, orange, white, outer green and red contour refer to the DIRE emissions at 10:23, 11:08, 12:28, 13:32 and 15:33 UT, respectively.

Table 3.1 Height of radio source inferred from height-time and pB images.

UT	f (MHz)	n (cm^{-3})	$r_{h\text{-}t}$ (Rs)	r_{pB} (Rs)
10:23	11.4	1.6×10^6	7.8	2.6
11:08	9.3	1.1×10^6	10.1	2.9
12:28	5.0	3.1×10^5	14.5	3.9
13:32	4.3	2.7×10^5	18.2	4.1
15:33	2.9	1.0×10^5	25.7	5.3

"f" is emission frequency. "n" is local plasma density. "$r_{h\text{-}t}$" and "r_{pB}" refer to PCME flank distance from height-time (h-t) measurements and the plasma level distance inferred from pB images, respectively.

Interaction of PCME with the streamer can also explain the delay of the onset of DIRE compared to the type II burst because the streamer is at a different longitude than the source region. Additional time is needed for the PCME flank to reach the streamers and accelerate to a speed high enough to be super-Alfvenic.

3.3.2 Shock Speed at the DIRE Source Region

We now compare the speeds of the shock and the PCME at the LE and flank using the drift rates measured from the dynamic spectrum. The shock speed, V_{sh}, is related to the drift rate (df/dt) according to the relation in equations (2.1), (2.2), (2.3) and (2.4). The height (r_c) is extracted

from the height-time plots of the LE and flank displayed in Figure 3.3 (c) and (d). „α‟ is ~2 for the interplanetry medium, consistent with the LDB density model at large "*r*".

In order to derive the shock speed from the regular type II burst, we consider a small section of the dynamic spectrum between 0.7–0.45 MHz, which has duration of ~105 minutes. The central time of the section (t_c) is 12:50 UT. Around this time, the DIRE drifts from 6–4.7 MHz in ~71 minutes. The central time of the section (t_c) is 12:35 UT. These ranges are indicated by white lines superposed on the spectra of the regular type II burst and DIRE in Figure 3.1. Assuming the LE is the source of the regular type II burst and the flank for the DIRE, we computed the shock speed using equations (2.1)–(2.4). The de-projected speeds of the PCME and the shock (from the regular type II drift) of the LE are 1314 and 1654 km s^{-1}, respectively. The de-projected PCME and shock speeds (from the DIRE drift) derived of the flank are 1012 and 954 km s^{-1}, respectively.

Given the uncertainty in the measurements of the speed from LASCO images and the drift rate from the dynamic spectrum, the agreement between the shock and CME speed are very satisfactory at the LE (regular type II) and flank (DIRE). We thus conclude that DIRE should be due to the passage of the CME-driven shock through the dense streamer.

3.4 Discussion

The primary result in this chapter is that the diffuse interplanetary radio emission reported here is a consequence of (i) extraordinary density in the streamer, and (ii) the passage of the shock flank through this streamer with sufficient speed. We have presented measurements from white light images and the radio dynamic spectra to support this interpretation. The emission mechanism seems to be similar to that of the regular type II burst, except that DIRE happens only when the above two conditions match. Our preliminary survey indicates that the DIRE emission is not

uncommon. It generally accompanies fast CMEs that produce intense type II bursts. A statistical investigation of the DIRE feature and the associated CMEs will be reported in the next chapter.

It must be noted that the spectral properties of the regular type II bursts and DIRE are quite different. DIRE consists mostly of discrete short-duration bursts similar to type I bursts or herring bone bursts at lower frequencies (see e.g., Carley et al. 2015). The bursts arise probably due to the injection of weak electron beams accelerated at the shock flank into the interplanetary open magnetic field. Recently, Magdelenic et al. (2014) reported a type II burst from the flank of a CME also involving interaction with a streamer. Gopalswamy et al. (2016, under preparation) found nonthermal radio emission from a polar CME with a similar fine structure. Decametric type IV bursts sometimes show such fine structure (Melnik et al. 2011), but no type IV burst is observed in the present event. Furthermore, these authors did not observe additional type II features as we reported here. It is possible that different combination of density, speed, and ambient magnetic field configuration can lead to different spectral features (see e.g., Susino et al. 2015).

3.5 Conclusions

We have reported on a new spectral feature of interplanetary radio emission, which we call diffuse interplanetary radio emission (DIRE) in the decameter-kilometric range. The DIRE is accompanied by a regular type II burst, which does not have a harmonic relationship with DIRE. We suggest that the emission originates from the western flank of the CME-driven shock where it interacts with a dense streamer. The flank shock becomes stronger when it passes through a streamer where the Alfven speed is lower compared to the normal corona. We have derived a consistent picture by combining radio dynamic spectra, white-light images, and polarized brightness images. The results presented here have important implications for electron acceleration by CME-driven shocks in the interplanetary medium. The results support the

possibility of electron acceleration by quasi-perpendicular region in the flank as well as quasi-parallel region around the nose. The spectral features are also different because of the magnetic configuration in the two regions.

Chapter 4

A Statistical Study of Diffuse Interplanetary Radio Emission Associated with Type II Radio Bursts

This chapter focuses on a statistical study of the "Diffuse Interplanetary Radio Emission (DIRE)" associated with the regular type II bursts and coronal mass ejections (CMEs) reported in Chapter 3. DIREs have different drift rates compared to those of the regular type II bursts. The onset of DIREs is generally delayed from the onset of the regular type II bursts. DIREs are mostly associated with fast-halo and disk centered CMEs.

4.1 Introduction

The new kind of drifting feature reported in Chapter 3 is rather diffuse consisting of a series of short duration bursts (Gopalswamy et al. 2016; Teklu et al. 2016). These bursts are termed diffuse interplanetary radio emission (DIRE) because they have an appearance rather different from the regular type II bursts. DIREs are observed by Wind/WAVES. Since the DIRE events are not uncommon, we determine statistics of these events and their associated CMEs and regular type II bursts.

This chapter is organized as follows. Section 4.2 introduces the events. Section 4.3 contains the analysis and discussion. The last section 4.4 has the conclusion.

4.2 Data Selection

The main focus of this research is to study the characteristics of the 10 DIREs observed by Wind/WAVES in the time range 1996–2012 with two large data gaps: 1998 July-September and 1999 January. The associated type II burst information has been obtained from

(http://cdaw.gsfc.nasa.gov/CME_list/radio/waves_type2.html) available online at the CDAW Data Center. The associated properties of the CMEs are also studied. The associated CMEs are listed in the SOHO/LASCO CME Catalog as described by Yashiro et al. (2004) and Gopalswamy et al. (2009) (see http://cdaw.gsfc.nasa.gov/CME_list/index.html). The regular type II bursts we consider start in the decameter-hectometric (DH) wavelengths (except for one event) and may continue to kilometric (km) wavelengths. The DH type II bursts and DIREs are observed by RAD1 and RAD2 receivers of the Wind/WAVES experiment. The radio telescope network (RSTN) data on metric radio bursts have been compiled by NOAA‟s Space Weather Prediction Center (SWPC) and available online at the CDAW Data Center, http://cdaw.gsfc.nasa.gov/CME_list/NOAA/org_events_text). The associated white-light CME images are obtained by the SOHO mission‟s LASCO. The spatial data overlap between the white-light images and radio images allow us to connect the CMEs with the DIREs.

The DIRE data set contains one DH, two km and seven DH-km events. The associated regular type II burst set consists of one metric, three DH and six DH-km events. Each event has a uniquely identified CME associated with the regular type II burst. They are listed in Table 4.1. Column one and three are the starting and ending date of the DIRE. The starting and ending time is given in columns two and four, respectively. The starting and ending frequency are presented in columns five and six. With a similar pattern, the last 6 columns represent the associated regular type bursts. The source location, date, time, width, speed and acceleration of the associated CME are given in the middle columns seven, eight, nine, ten, eleven and twelve.

Table 4.1 List of DIRE events used in this study along with the associated type II bursts and CMEs.

DIRE						CME						Regular type II Burst					
Ds	ts	De	te	fs	fe	Source	D	t	W	V	a	Ds	ts	De	te	fs	fe
05/06/1998	09:52	05/06	11:25	02.10	0.99	S11W65	05/06	08:29	190	1099	24.50	05/06	08:25	05/06	08:55	014.0	5
09/27/2001	10:23	09/27	19:33	11.40	1.60	S15W50	09/27	07:54	180	0882	07:63	09/27	08:20	09/28	06:47	001.8	0.08
11/02/2001	11:58	11/02	19:28	03.10	1.59	N12W2	11/01	22:30	360	453	00.20	11/02	22:31	11/02	23:13	001.1	0.85
11/02/2003	04:34	11/01	08:31	03.59	1.69	S12W60	11/01	23:06	>93	0899	–26.3	11/01	22:55	11/02	00:50	14.0	2.0
12/03/2004	23:32	12/04	13:18	00.70	0.27	N08W02	12/03	00:26	360	1216	–19.8	12/03	00:07	12/04	04:30	10.0	0.06
09/06/2011	03:18	09/06	06:07	03.90	1.4	N14W07	09/06	02:24	360	0782	105.6*[1]	09/06	01:45	09/06	01:48	121	54.0
01/19/2012	20:06	01/20	01:19	04.70	01.27	N32E22	01/19	14:48	360	1120	54.1	01/19	15:01	01/20	02:45	09.40	0.1
03/07/2012	17:01	03/08	08:21	01.20	0.45	N17E27	03/07	00:24	360	2684	–882	03/07	01:00	03/07	19:00	16	0.03
04/15/2012	09:23	04/15	15:11	00.89	0.42	S13E13	04/15	09:48	160	0272	–9.7*[1]	04/15	08:50	04/15	09:25	13	0.63
05/27/2012	07:38	05/27	18:49	03.14	0.45	S11W60	05/27	05:48	197	0725	–0.2	05/27	06:00	05/27	06:42	2.5	1.1

The letters “Ds”, “ts”, “De”, “te”, “fs”, “fe”, “D”, “t”, “a”, “W” and “V” refer to the start date, start time (in UT), end date, end time (in UT), starting frequency (in MHz), end frequency (in MHz), date of CME, time of observation of CME in C2 (in UT), acceleration of CME (in m s^{-2}) and speed of CME (in km s^{-1}), respectively. “*[1]” shows uncertainty in the acceleration. The end frequencies used include only the clearly observable in the dynamic spectrum.

The DIRE events on 1998 May 06, 2001 September 27, 2001 November 02, 2011 September 06 and 2012 January 19 are long duration events but they are unclear beyond some interval. They are superposed with either the regular type III bursts or type III storm. They may have also unclear drift beyond some time. We only consider the portion with clear drift. We say that there are two regular type II bursts associated with the DIRE on 1998 May 06. In the analysis, the pure DH is considered. The data gap between 08:49 and 09:40 UT creates an ambiguity. Onset of DIRE should be earlier than the end of the data gap. The regular type II bursts associated with the DIREs on 2001 November 02 and 2012 April 15 are blob like. The 2003 November 2 DIRE has a one hour data gap. The 2011 September 06 and 2012 May 27 events have the charactertics of both regular type II burst and DIRE. For statistical purposes we include them under DIRE. The 2011 September 06 DIRE is associated with a metric type II burst (see Figure 4.1 (a)). The 2011 September 6 DIRE event has F-H structure but the fundamental is used for analysis. The 2012 May 27 is associated with a short lived DH (R1) and long lived DH-km (R2) type II bursts (Figure 4.1 (b)) in addition to the 2 clear DIRE lanes (indicated as F and H) which have a clear F-H frequency relationship (see Figure 4.1 (b)). “R1” and “F” are used for the analysis.

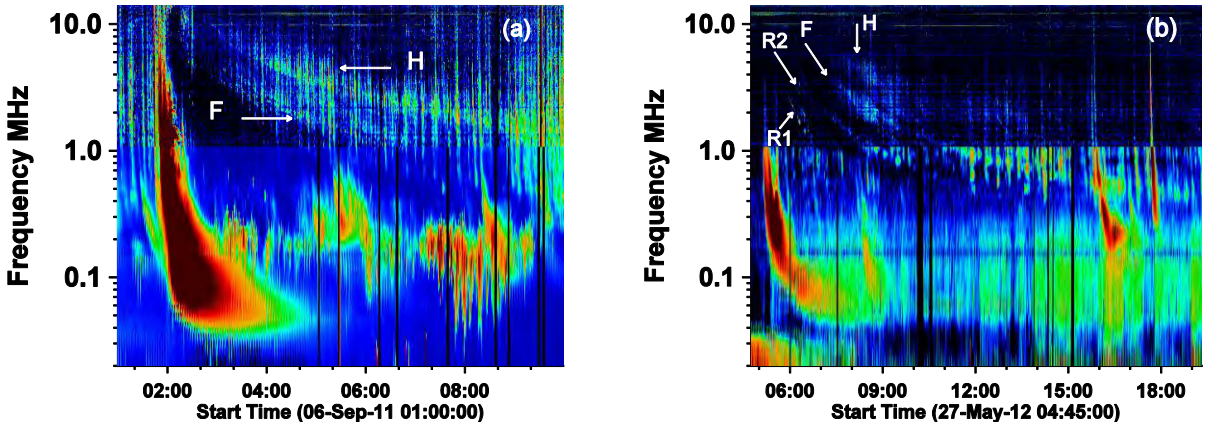

Figure 4.1. The Wind/WAVEs dynamic spectrum showing the DIRE on 2011 September 06 (a) and, regular type II burst and DIRE on 2012 May 27 (b). The "F" and "H" in (a) and (b) show the Fundamental and harmonic structures of the DIREs. The "R1" and "R2" in (b) indicate the DH and DH-km regular type II bursts, respectively, on 2012 May 27. The regular type II burst associated with DIRE on 2011 September 06 is not shown since it occurs at metric wavelength.

The CME associated with 2003 November 02 event has uncertain width. The CME associated with 2011 September 06 and 2012 April 15 events have uncertain accelerations. The CMEs associated with the events 2011 September 06 and 2012 April 15 are poor and do not have white-light images in the C3 FOV.

4.3 Analysis

The onset frequency, drift rate, delay time, onset height, and the CME kinematics of the DIREs and the associated regular type II bursts are analyzed. First, an illustrative example which occurred on 2004 December 03 is described.

Figure 4.2 (a) shows a kilometric (km) DIRE and the associated regular DH-km type II burst, which occurred on 2004 December 03. The DIRE has an onset frequency of about 0.66 MHz at

23:32 UT. The regular type II burst has a higher onset frequency of 10 MHz at 00:07 UT. The DIRE is delayed by about 23 hours and 20 minutes from the regular type II burst onset. At the 23:32 UT on December 03, the DIRE and regular type II burst are at frequencies 660 and 86 kHz, respectively. The DIRE is at high frequency (~ 8 times of the regular type II burst) which shows that they do not have fundamental – harmonic relationship. The DIRE and regular type II burst drift by 7.9×10^{-6} and 6×10^{-7} MHz s^{-1}, respectively in DIRE interval. The DIRE has a higher drift rate compared to the regular type II burst. The regular type II burst has a single component early on but acquires F-H structure in the kilometric range beyond 08:06 UT. It also has an intensity enhancement around this time.

The associated CME is a disk event – halo CME observed at 00:26 UT on December 03 in the C2 FOV (see Figure 4.2 (b)). It erupts from N08W02. It moves with a linear speed of 1216 km s^{-1}. Using a second order fit to the height-time profile in Figure 4.2 (c), it is decelerating by 20 m s^{-2}. It is observed only for 4 hours in the LASCO FOV. The CME is beyond the LASCO FOV at the DIRE onset. The DIRE is a highly lagging event. Therefore, the CME-radio analysis for the DIRE is not possible. On the contrary, the CME is still inside the occulting disc at the onset of the regular type II burst. In the frequency interval of 0.67–0.33 MHz (regular type II burst), the CME and shock speeds are 1030 and 1143 km s^{-1}, respectively. At the central time of this interval (2:50 UT), the CME is at 19 Rs. The „α" used for the shock speed is 2. CME-shock speed analysis shows that the regular type burst is produced at the nose. Since the DIRE occurs at higher frequency, it should be from the flank. The flank of the CME passes through a streamer sitting at PA ~ 118°. This is consistent with the fact that the CME nose is at a large distance from the Sun, incompatible with the higher frequency (and hence lower plasma level) of the DIRE emission.

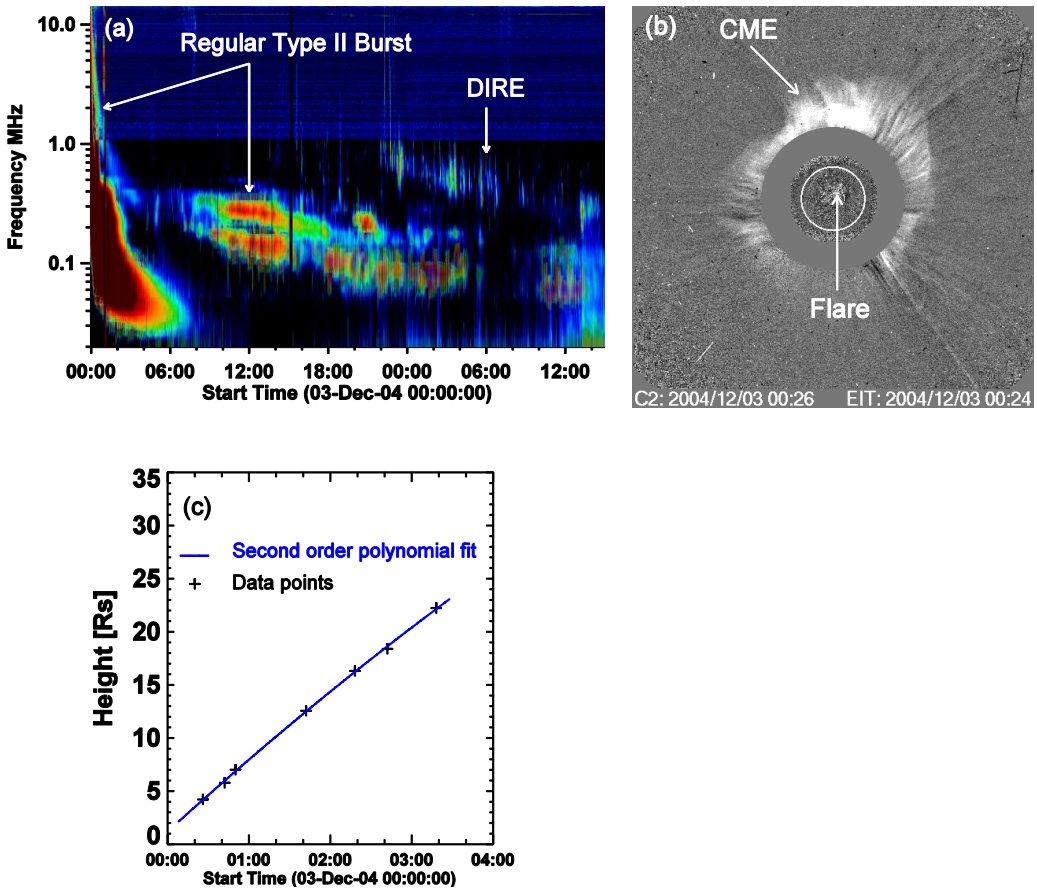

Figure 4.2. (a) Wind/WAVEs dynamic spectrum showing the regular DH-km type II burst and km diffuse Interplanetary Radio Emission (DIRE) on 2004 December 03. (b) The first observation of the associated halo-CME in LASCO/C2 running difference image superposed to 193 Å EIT image. The flare location is also indicated. (c) The height-time profile of the CME in C2 and C3 FOVs. The height-time measurement, indicated in black "+" symbol, is fitted to a 2nd order polynomial in blue.

4.3.1 DIRE and Associated Regular Type II Burst

The statistical properties of the DIRE events are presented in Figure 4.3 in comparison with those of the regular type II bursts. The frequency onset of the regular type II burst is calculated in two different ways. One is the average frequency over the entire range of emission (case 1). The

other is over the interval of the DIRE event (case 2, Diffuse Interval). In case 1, the DIRE events have lower average onset frequency (3.5 MHz) than regular type II bursts (19.1 MHz) (see Figure 4.3 (a)). If we compare the average frequencies in case 2, the DIRE occurs at 4.6 MHz but the regular type II burst occurs 0.4 MHz (See Figure 4.3 (b)). The DIREs have average frequencies ~10 times to the regular type II bursts. For the second analysis, only the type II radio bursts with frequencies extending up-to the onset and beyond of the DIRE are considered. These are the 2001 September 27, 2004 December 03, 2012 January 19 and 2012 March 07. Fundamental emission is considered in all the cases.

DIREs have lower average drift rate, 1.2×10^{-4} MHz s^{-1}, than that of the regular type II bursts, 2.1×10^{-2} MHz s^{-1} in case 1 (see Figure 4.3 (c)), respectively. In case 2, the average drift rates are 1.3×10^{-4} MHz s^{-1} and 9×10^{-6} MHz s^{-1}, respectively (see Figure 4.3 (d)). DIREs have lower average drift rates in the first case and higher in the second case. The drift rates of the 4 events are considered in the second case since all the DIREs do not have regular type II bursts in case 2.

Figure 4.3 (e) shows that all the DIRE events are delayed from the onset of the regular type II bursts. The average delay time is 7.15 hours. The nearest and the farthest delay times compared to the onset of the regular type II burst are 0.5 and 23.5 hours, respectively.

Regular type II bursts have lower average CME height at their onset (3.4 Rs), than that of the DIRE events (15.3 Rs) (see Figure 4.3 (f)). The CME leading edges of 4 events are beyond the LASCO FOV at DIRE. Two events occurred while the CME is within the occulting disk of C2 FOV. DIREs form generally when the CME LE is at large height.

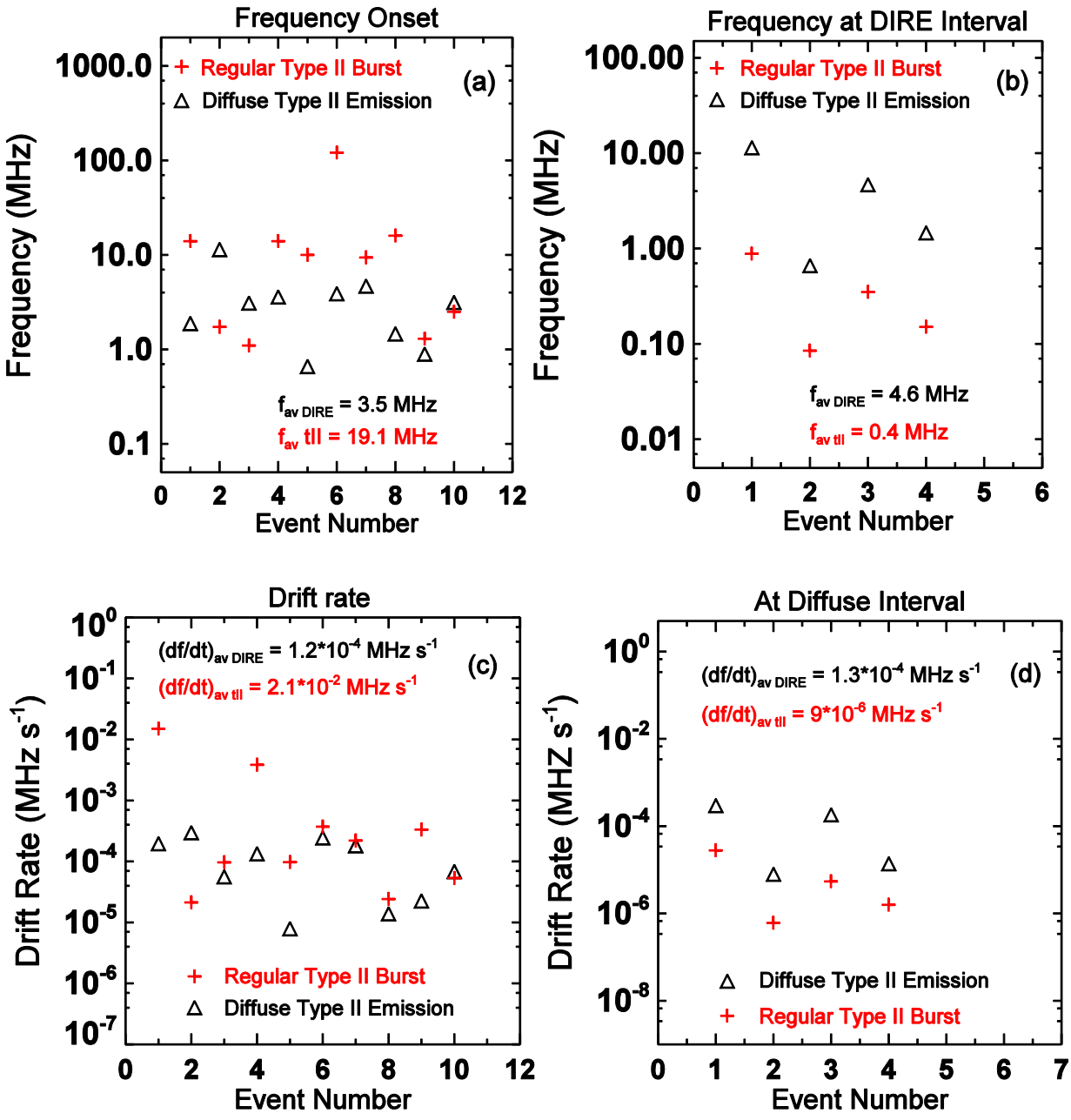

* The figure caption to the above plots is described on the next page (see Figure 4.3).

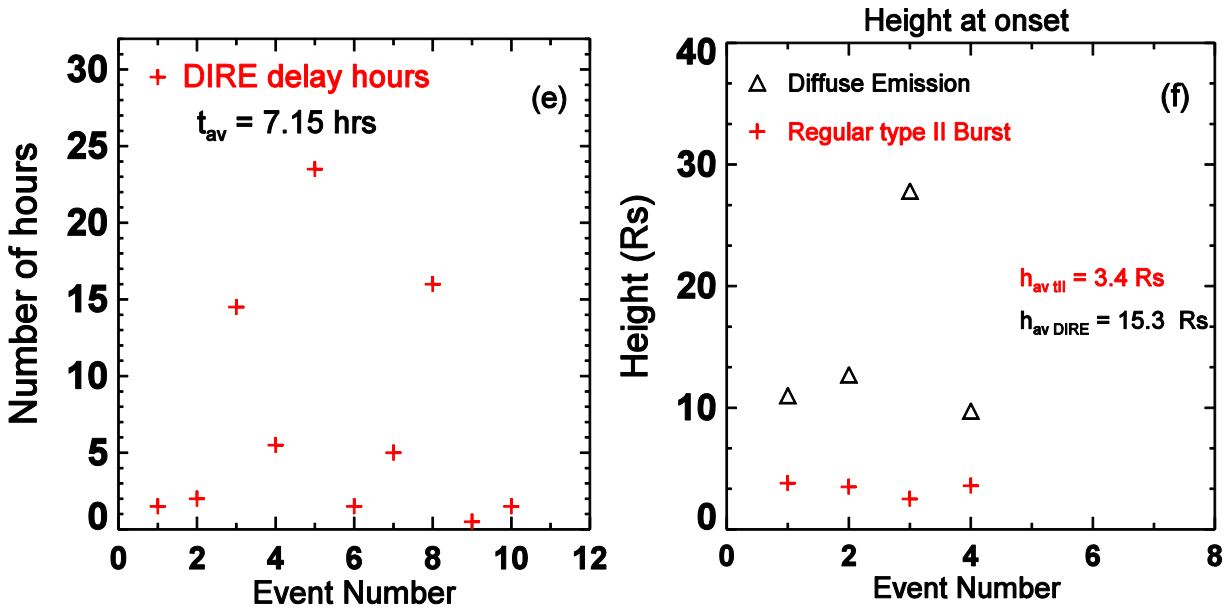

Figure 4.3. The horizontal axis in (a), (c) and (e) indicate all the DIRE dates but in (b) and (d) they correspond to 27/09/2001, 03/12/2004, 19/01/2012 and 07/03/2012. In (f) the dates 06/05/1998, 27/09/2001, 02/11/2003 and 27/05/2012 are considered. The $f_{av\ DIRE}$, $(df/dt)_{av\ DIRE}$ and $h_{av\ DIRE}$ show the average frequency, drift rate and onset height of the DIRE, respectively while the $f_{av\ tII}$, $(df/dt)_{av\ tII}$, and and $h_{av\ tII}$ are the corresponding values to the regular type II burst. t_{av} is the time gap between the onset of the regular type II burst and DIRE. The onset frequency of the regular type II burst and DIRE over the entire range of emissions in (a) and at the DIRE interval in (b) are compared. (c) and (d) compare the drift rates of the two emissions over their entire range of emissions and at the DIRE interval, respectively. (e) summarizes the time gap between the DIRE and regular type II burst onsets. (f) The height of the CME at the onsets of the type II burst and DIRE. The corresponding average values are also indicated in each box. The red (cross) and black (diamond) represent the data of the regular type II burst and the DIRE, respectively.

4.3.2 CME Kinematics

The average speed, non-halo width, acceleration and halo fraction of the DIRE-associated CMEs in the LASCO FOV are 1013 km s^{-1}, 164^0, 4.8 m s^{-2} and 50%, respectively. 58.3% of them have speeds greater than 1000 km s^{-1} (see Figure 4.4 (a-c)). Most of the CMEs are energetic and accelerating on average. 60% of them are disk center events (< 30^0) but 90% are in the central meridian distance (CMD) < 60^0 (see Figure 4.4 (d)). Thus, most DIRE-associated CMEs originate close to the disk-center. Accordingly, we expect higher de-projected speed. The source

location of the slowest CME, 272 km s^{-1}, is S13E13. It is a disk-center event, so the true speed is likely to be significantly higher. Figure 4.4 (d) shows that the distribution of the CME source locations is slightly higher in the western hemisphere (60%). However, the number is too small to derive firm conclusions at this point. Half of the CME population is either wide or halo. Consistent with their high speeds, 50% of the CMEs are decelerating. The positive acceleration in Figure 4.4 (c) is due to the uncertain values at the tail. It is clear that the DIRE associated CMEs are faster and wider, suggesting that they are energetic CMEs. The CME part away from its nose can also cause a significant shock.

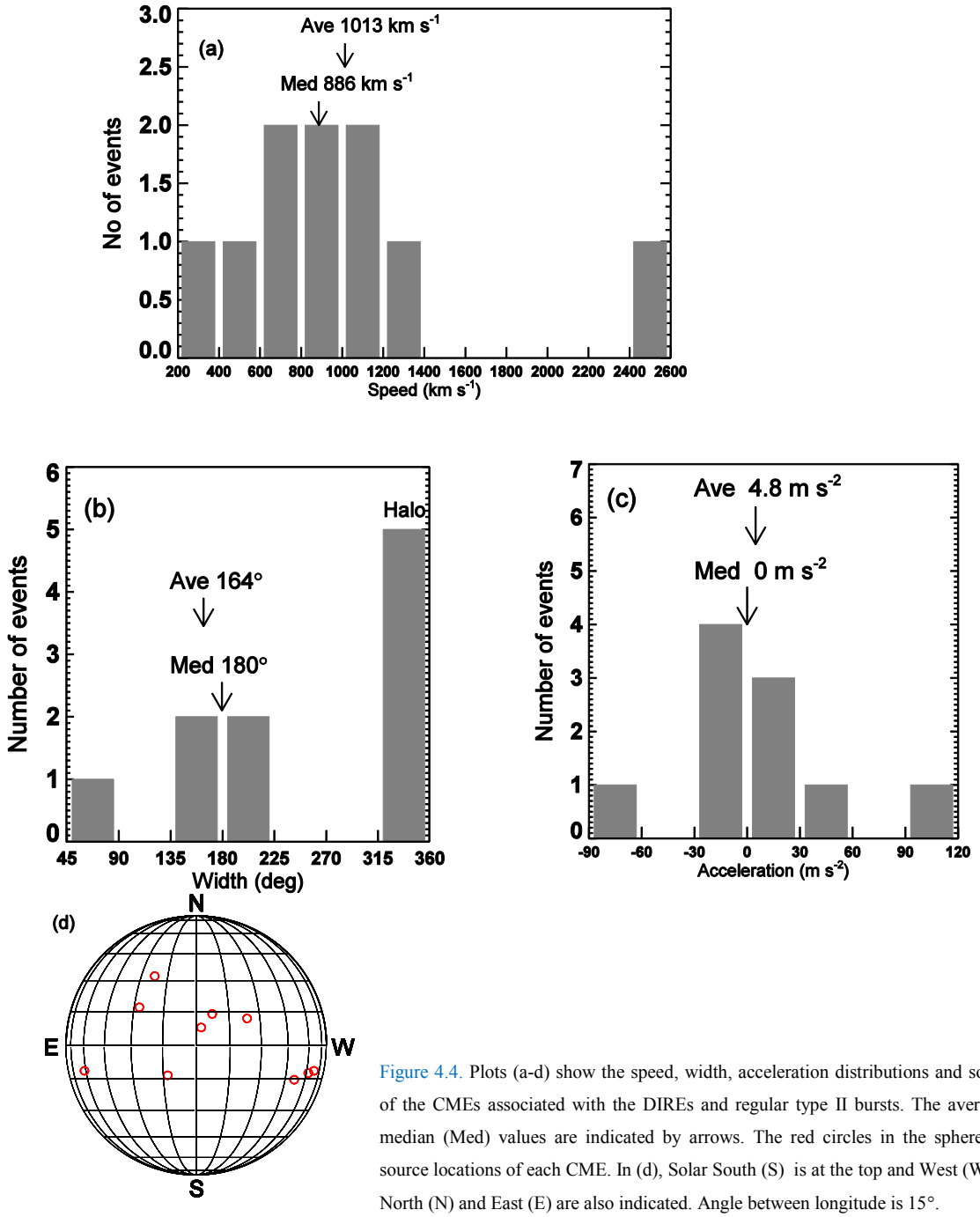

Figure 4.4. Plots (a-d) show the speed, width, acceleration distributions and source locations of the CMEs associated with the DIREs and regular type II bursts. The average (Ave) and median (Med) values are indicated by arrows. The red circles in the sphere represent the source locations of each CME. In (d), Solar South (S) is at the top and West (W) is to the left. North (N) and East (E) are also indicated. Angle between longitude is 15°.

4.4 Discussion and Conclusions

The characteristics of the DIRE events associated with regular type II bursts that occurred during 1996–2012 are analyzed. There are only 10 clear events in this time range, suggesting that these events are rare, but not uncommon. The diffuse interplanetary radio emissions occur at higher frequency compared to regular type II burst. They have relatively higher drift rates at the DIRE interval. The DIRE onset is clearly delayed with respect to the type II onset. Most of the associated CMEs are disk-centered, wide and fast or halos. Consistent with the high-speed, 50% of the CMEs are decelerating. The location of the CME leading edge at the onset of DIRE is much larger than that at the onset of the associated type II burst. The energetic CMEs are expected because only fast and wide CMEs can drive shocks to produce type II radio emission.

These characteristics are consistent with the interpretation that DIREs are similar to the regular type II bursts, except that they occur at the flanks of the CME-driven shocks. The DIRE events are rare because a streamer needs to be present at the shock flank to provide a dense region with low Alfven speed. The flank interpretation is consistent with the fact that DIRE emission consists of a series of short-duration bursts indicating weak electron beam injection into open field lines traversed by the shock flank. The higher drift rate of the DIRE events does indicate a faster shock because the scale heights are lower in the spatial domain they are produced. The shock speed is determined by a combination of scale height and the drift rate. Finally, the disk-center CMEs may indicate that the weak DIRE can freely propagate toward the observer. For a limb event, the DIRE emission from the flank behind the sky plane needs to propagate through the CME before reaching the observer and hence less likely to be observed. This is also consistent with the flank region as the source of DIRE emission.

Chapter 5

Hierarchical Relationship of pure DH, m-DH and DH-km Type II Bursts Using the Kinematic Properties of the Associated CMEs

---

Using type II radio bursts from Wind/WAVES and the associated coronal mass ejections (CMEs) from SOHO/LASCO, Gopalswamy et al. (2005a) found a hierarchical relationship between the wavelength range of the type II bursts and CME kinetic energy. Under „DH Type II bursts" they have included pure DH, m-DH and DH-km bursts. In this work, we consider the pure DH, m-DH and DH-km subsets separately. We find that DH-km type II burst associated CMEs have the largest average speed, non-halo width and halo fraction. The m-DH type II burst associated CMEs have slightly higher speeds than the pure DH type II burst associated CMEs. The DH-km type II burst associated CMEs have the largest mass. m-DH type II burst associated CMEs have slightly larger mass than pure DH associated type II burst associated CMEs. Our m-DH and pure DH CMEs type II burst associated CMEs have slightly lower speed and fraction of halos compared to DH type II burst associated CMEs in Gopalswamy et al. (2005a). However, the DH-km type II burst associated CMEs have higher speeds than Gopalswamy et al. (2005a). We find that the kinetic energy of CMEs organizes the hierarchal relationship of type II bursts. DH-km type II burst associated CMEs have the largest SEP association compared to m-DH and pure DH type II burst associated CMEs. The DH-km type II burst associated CMEs SEP association is slightly smaller than that of Gopalswamy et al. (2005a) m-km type II burst type II burst associated CMEs. The SEP sources are generally located in the western hemisphere because of magnetic connectivity requirement. The CMEs associated with major SEP associated have larger average speed than the pure DH and m-DH CMEs but smaller than the DH-km CMEs.

Chapter 5

5.1 Introduction

Type II bursts are observed at 6 spectral domains of emission. They occur at metric (m), decameter-hectometer (DH), kilometric (km) wavelengths and a combination of these: m-DH, DH-km and m-km. Type II bursts at metric wavelengths can be observed by radio receivers on the ground, but bursts at longer wavelengths can be observed only by radio receivers on board spacecraft because of the ionosphere that blocks longer wavelength bursts. Figure 1.14 shows these domains with the average speeds of the associated CMEs from Gopalswamy (2010).

Gopalswamy et al. (2005a) reported on the hierarchal relationship between the wavelength ranges of type II bursts and the kinetic energy of the associated CMEs. They measured the average speed, non-halo width, acceleration, and the fraction of full halo CMEs for CMEs associated with the pure metric, DH and m-km type II bursts. All the quantities increased progressively from pure metric to DH and the m-km CMEs indicating that the CME kinetic energy organizes the different populations of the type II bursts. The DH type II associated CMEs are more energetic than those associated with metric type II bursts, and m-km type II bursts are associated with the most energetic CMEs. CMEs with m and km type II bursts have comparable average speeds but the former CMEs are decelerating and the latter ones are accelerating, i.e., their acceleration profiles as a function of the distance are drastically different.

We revisit the hierarchical relationship between the different wavelength ranges of the type II bursts and the associated CME kinetic energy. We consider pure DH, m-DH and DH-km as separate groups, which are previously included under a single DH group (numbered 2, 3 and 4 in Figure 1.14). The m-DH type II bursts are identified by comparing the onset times of the metric and pure DH type II bursts.

We have also considered the associated solar phenomena such as solar energetic particle (SEP) events and soft X-ray flares using data from GOES satellites situated at Earth‟s geosynchronous orbit. The GOES integral proton flux with energy greater than 10 MeV is used for the SEP event

analysis. Since SEPs and Earth-hitting CMEs have direct impact on space weather, type II radio bursts might provide early warning on the launch of energetic CMEs because type II bursts are signatures of CME-driven shocks and the radio emission from the shock reach at Earth in ~ 8 minutes. Therefore, we look at the SEP association of the pure DH, m-DH and DH-km type II burst associated CMEs. We looked at the source locations of the associated CMEs as well.

The data selection, data analysis and results on the CME kinematics and associated SEP events will be reported in section 5.2. Section 5.3 contains the discussion on the obtained results. The conclusion will follow in section 5.4.

5.2 Data Selection, Data Analysis and Results

5.2.1 Data Selection

Radio dynamic spectra used are from WAVES on board the Wind spacecraft. CME data are from the CDAW LASCO CME Catalog (Yashiro et al. 2004; Gopalswamy et al. 2009; http://cdaw.gsfc.nasa.gov/CME_list/index.html). The study period spans from 1996 to 2004 with two large data gaps: 1998 July-September and 1999 January. The type II lists used span the same years as the CME list but they are extracted from CDAW Wind/WAVES Type II Bursts and CMEs (http://cdaw.gsfc.nasa.gov/CME_list/radio/waves_type2.html). We start with 155 DH type II bursts (that do not have kilometric component) and the associated CMEs. We rejected 44 faint and unclear bursts, and those with no CME data. We searched for the association of the remaining 111 events with the metric type II bursts listed in the NOAA Edited Solar Event reports (ftp://ftp.swcp.noaa.gov/pub/warehouse). Out of the 111 events, 52 are pure DH and 59 are m-DH type II bursts. One of the CMEs associated with the m-DH type II burst does not have a measurable CME acceleration due to limited cadence. Similarly, there are 128 DH-km type II bursts listed but we find that the 71 are m-km as listed in Gopalswamy et al. (2005a). Out of the

remaining 57 events, 29 are rejected due to various reasons: (i) some are weak and unclear; (ii) 3 bursts do not have CME information; one is a back side event and the other two lack source location information. We analyze the properties of associated CMEs, and the SEP association rate in the three different categories of DH type II radio bursts (see Figure 1.14). In particular, we obtain the average speed, non-halo width, acceleration and full halo fractions of the CMEs associated with pure DH, m-DH and DH-km type II bursts and compare them with the results obtained by Gopalswamy et al. (2005a). All the speed measurements are done in the sky plane. There is no attempt made to correct for projection effects since the main focus is the analysis of the speeds, widths and accelerations of the CMEs under same platform with Gopalswamy et al. (2005a).

Table 5.1 contains the list of DH-km type II bursts and the associated CMEs together with the flare and SEP information. The first and third columns are the starting and ending date of the type II radio burst. The starting and ending time is given in the second and fourth columns, respectively. The starting and ending frequency are presented in fifth and sixth columns. The eruption source location, active region number, and the associated flare information are given in columns seventh, eighth and ninth, respectively. The date, time, central position angle, width, speed, acceleration and the SEP intensity rate are given in columns from tenth to sixteenth, respectively.

Table 5.1 List of DH-km type II bursts and the associated CMEs together with the flare and SEP information.

Type II Burst							Flare			CME					
Ds	ts	De	te	fs	fe	Loc.	AR#	Imp.	D	t	CPA	W	V	a	SEP
11/05/1998	22:00	07-Nov	8:00	5	0.500	N22W18	8375	M8.4	05-Nov	20:44	Halo	360	1118	–24	10
06/01/1999	18:50	02-Jun	09:00	14	0.400	NW90b	-----	----	01-Jun	19:37	Halo	360	1772	1.8[*1]	48
05/15/2000	16:47	16-May	14:00	4.8	0.400	S24W67	8993	C7.8	15-May	16:26	257	>165	1212	–20.5	2
10/25/2000	09:30	25-Oct	24:00	10	0.300	N09W63	9199	C4.0	25-Oct	08:26	Halo	360	770	17.4	15
11/08/2000	23:20	09-Nov	12:00	4	0.200	N10W77	9213	M7.4	08-Nov	23:06	271	>170	1738	69.9	14800
01/28/2001	15:45	28-Jan	17:00	14	0.200	S04W59	9313	M1.5	28-Jan	15:54	Halo	360	916	3.5	49
04/03/2001	03:40	03-Apr	07:25	14	0.400	S21E83	9415	X1.2	03-Apr	03:26	108	292	1613	–16.7	>500
04/06/2001	19:35	07-Apr	01:50	14	0.230	S21E31	9415	X5.6	06-Apr	19:30	Halo	360	1270	–57.3	HiB
04/26/2001	12:40	28-Apr	05:00	5	0.020	N20W05	9433	M1.5	26-Apr	12:30	Halo	360	1006	21.1	57
05/07/2001	12:00	07-May	13:50	2	0.280	NW90b	-----	----	07-May	12:06	286	205	1223	19.2	28

09/24/2001	10:45	25-Sep	20:00	7	0.030	S16E23	9632	X2.6	24-Sep	10:30	Halo	360	2402	54.1	2560
10/01/2001	07:00	01-Oct	18:30	1	0.150	S24W81	9628	M9.1	01-Oct	05:30	Halo	360	1405	97.8	678
10/05/2001	11:35	05-Oct	12:55	14	0.500	SW90b	-----	----	05-Oct	10:30	Halo	360	1537	3.3	HiB
08/16/2001	00:10	15-Aug	08:40	5.4	0.200	Back	-----	----	15-Aug	23:54	Halo	360	1575	–31.7	493
01/08/2002	18:30	09-Jan	24:00	14	0.090	NE90b	-----	----	08-Jan	17:54	Halo	360	1794	81.4	92
04/30/2002	22:30	30-Apr	23:20	2	0.500	W90b	-----	----	30-Apr	23:26	254	199	1103	–2.8	4
07/07/2002	11:35	07-Jul	20:00	14	0.200	S19W90	10017	M1.0	07-Jul	11:30	277	>228	1423	22.0[*1]	23
07/15/2002	21:15	16-Jul	05:00	5	0.175	N19W01	10030	M1.8	15-Jul	21:30	14	>188	1300	–7.3	234
08/14/2002	02:20	14-Aug	24:00	1	0.030	N09W54	10061	M2.3	14-Aug	02:30	297	133	1309	–28.5	26
03/18/2003	12:25	18-Mar	13:45	4.5	0.500	S15W46	10314	X1.5	18-Mar	12:30	263	209	1601	–13.3	HiB
06/16/2003	00:00	16-Jun	03:00	14	0.400	S07E80	10386	X1.3	15-Jun	23:54	Halo	360	2053	–0.9	No SEP
04/06/2004	13:05	06-Apr	16:00	8	0.300	S18E15	10588	M2.4	06-Apr	13:31	Halo	360	1368	45.6	No SEP
04/08/2004	10:25	08-Apr	12:50	3	0.500	S15W11	10588	C7.4	08-Apr	10:30	Halo	360	1068	–36.5	No SEP
04/11/2004	04:20	11-Apr	05:35	14	0.500	S14W47	10588	C9.6	11-Apr	04:30	203	314	1645	–77.6	36
07/25/2004	15:00	26-Jul	22:25	1	0.028	N08W33	10652	M1.1	25-Jul	14:54	Halo	360	1333	7	55

07/31/2004	07:10	31-Jul	11:30	1	0.200	N05W89	10652	C8.4	31-Jul	05:54	259	>197	1192	46.4	HiB
12/03/2004	00:07	04-Dec	04:30	10	0.060	N08W02	10708	M1.5	03-Dec	00:26	Halo	360	1216	–19.8	3
11/11/2002	16:15	11-Nov	17:50	14	0.600	S13W60	10180	M1.8	11-Nov	15:54	212	093	1083	19.9	HiB

The letters “Ds”, “ts”, “De”, “te”, “fs” and “fe” refer to the start date, start time (in UT), end date, end time (in UT), starting frequency (in MHz), and the end frequency (in MHz) of the type II burst, respectively. The “Loc.”, “AR#”, “Imp.”, “D”, “t”, “CPA”, “W”, “V”, “a” and “SEP” describe the source of eruption of the CME, active region number, associated flare intensity, time of observation of CME in C2 (in UT), central position angle, width of the CME, speed of CME (in km s^{-1}), acceleration of CME (in m s^{-2}) and the associated solar energetic particle intensity (in pfu), respectively.

5.2.2 Data Analysis and Results

5.2.2.1 CME Properties

We compiled the 3 basic attributes (speed, non-halo width and acceleration) of CMEs associated with the pure DH, m-DH and DH-km type II bursts. The CME speed is obtained by a linear fit to the height-time measurements in the sky plane. The CME acceleration, in the sky plane, is found by a second order fit to the same height-time profile. The speed, width and acceleration are listed in the CDAW CME Catalog. The average speed, non-halo width, acceleration and fraction of halo CMEs of our combined data set are compared with the DH type II data set of Gopalswamy et al. (2005a).

Two exemplary case studies are considered in order to give a picture of some of the type II bursts considered in this study.

Pure DH Case: 2002 July 26

A type II burst confined to the DH domain occurred on 2002 July 26. Examination of the ground based data revealed that there is no type II burst in the metric domain. From the Wind/WAVES dynamic spectrum we determined that the burst does not extend to frequencies lower than ~ 1 MHz. Therefore, this is a pure DH type II burst. The CME associated with this event erupted from S19E26 (see Figure 5.1 (a)). It is first observed at 22:06 UT in the LASCO/C2 FOV. A faint feature ahead of the bright CME structure, a signature of an associated CME-driven shock (Sheeley et al. 2000; Vourlidas et al. 2003), is clearly visible in the LASCO/C2 running difference image at 23:06 UT displayed in Figure 5.1 (a). The geometry of the CME changes progressively as it moves further out from the Sun. The CME erupts along a pre-existing streamer, which affected the geometry of the CME around the nose region. This is seen especially in the C2 FOV. The CME is associated with a M8.7 flare (see Figure 5.1 (b)). The halo CME has a linear sky-plane speed of 818 km s^{-1} (see Figure 5.1 (c)). CME is decelerating

by –0.1 m s^{-2}. The CME is energetic enough to be associated with an enhanced fundamental-harmonic DH type II burst (see Figure 5.1 (d-e)). The eruption is also associated with type III and V radio bursts. The fundamental emission of the type II burst starts at ~ 8 MHz at 22:25 UT and drifts all the way to 2 MHz in about an hour. The harmonic emission is short durational, it is observed only for about 14 minutes. The height-time profile of the CME in C2 and C3 FOVs shows that the CME starts to drive a radio-loud shock at 2.7 Rs (shown by the vertical line at 22:25 UT in Figure 5.1 (c)). However, the type II radio emission is intermittent. The possible association with an SEP event is unknown since the eruption occurs during a period of high-intensity (~12 pfu; 1 pfu = 1 proton cm^{-2} sr^{-1} s^{-1}) background due to preceding SEP events (see Figure 5.1 (f)).

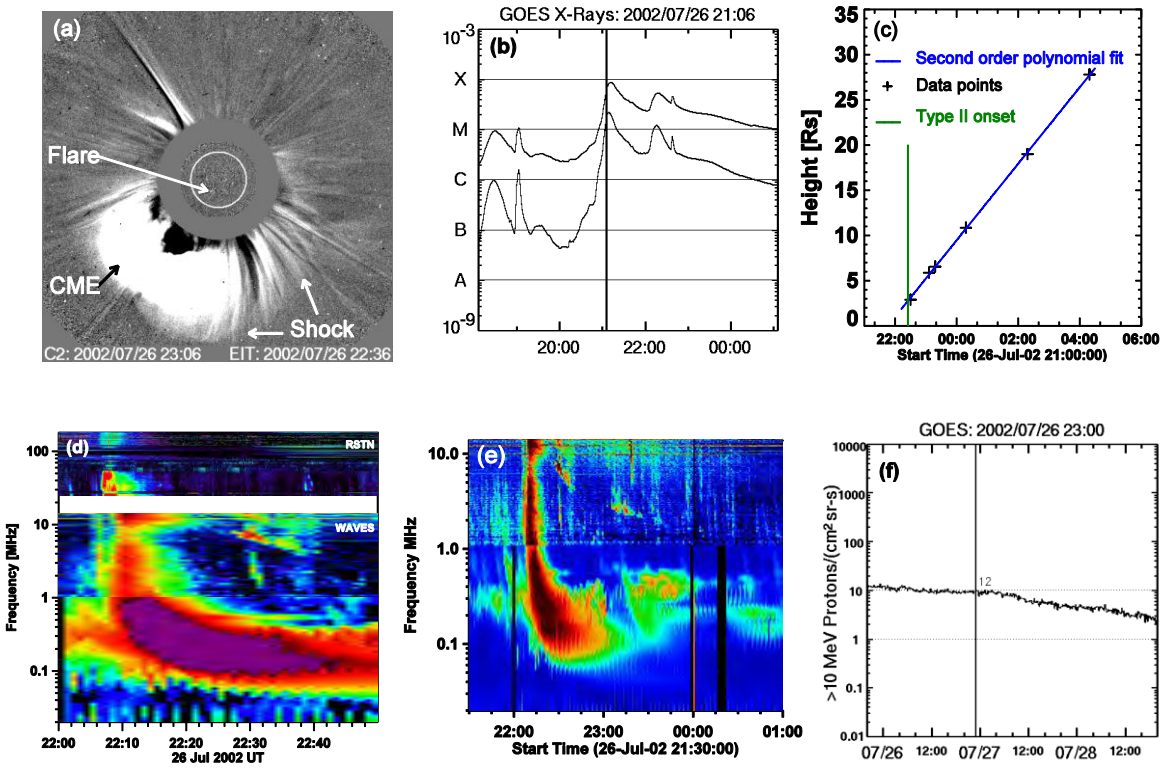

Figure 5.1. (a) LASCO/C2 running difference image of a CME on 2002 July 26 at 23:06 UT with a superposed 195 Å EIT difference image. The CME, CME-driven shock and location of flare are indicated by the arrows. (b) GOES soft X-ray intensity plot. The vertical line indicates the flare maximum time. (c) The height-time profile of the CME in the LASCO FOV. The data points (in "+" symbol) are fitted to a quadratic expression. The green vertical line indicates the onset of the fundamental emission of the DH type II burst. (d) The combined image of the radio emission at the metric and pure DH wave range from RSTN and Wind/WAVES. (e) The type II burst at the DH wavelength range from the Wind/WAVES dynamic spectrum. (f) The GOES > 10 MeV proton intensity showing enhanced background of 12 pfu at 23:00 UT. The horizontal lines indicate the 1 and10 pfu intensity levels.

m-DH Case: 2001 April 12

The 2001 April 12 type II burst starts in the metric domain and ends in the DH domain. Therefore, this is an m-DH type II burst. The associated halo CME in Figure 5.2 (a) erupted from S19W43. It is first observed at 10:31 UT in the LASCO/C2 FOV. It is associated with an X2.0 flare starting at 10:06 UT and peaking at about 10:31 UT (see Figure 5.2 (b)). A linear fit to the height-time measurements shown in Figure 5.2 (c) gives an average speed of 1184 km s^{-1} in the LASCO FOV. It is decelerating by –20 m s^{-2}. The high deceleration is consistent with the high speed of the CME, as high-speed CMEs are known to decelerate towards the solar wind speed as they propagate. The clear shock signature is observed early in the C2 FOV and the shock produces the type II bursts in the inner corona (see Figure 5.2 (a)). The type II emission consists of three fundamental – harmonic pairs at the metric range and it continues in the DH range (see Figure 5.2 (d) and (e)). The fundamental modes of the three in white, red and orange metric type II bursts start at 75, 32 and 59 MHz, respectively. The frequencies overlap at the onset of F2 and end of H1. In the DH domain, the emission is more enhanced and looks like a single broad horizontal feature. The emission seems to be a mix from different sections of the shock. The burst has a short life time of 30 minutes, which is well aligned with the high deceleration of the CME. The inhomogeneities in the density of the inner corona are manifested as intensity enhancements and frequency jumps of the type II emission. The LASCO/C2 image shows pre-existing streamer to the western quadrant, which may cause the intensity enhancement especially at the DH range. The CME source has a good magnetic connectivity to Earth and GOES detected ~ 40 pfu peak proton intensity in the >10 MeV channel (see Figure 5.2 (f)) in association with the CME and the radio burst.

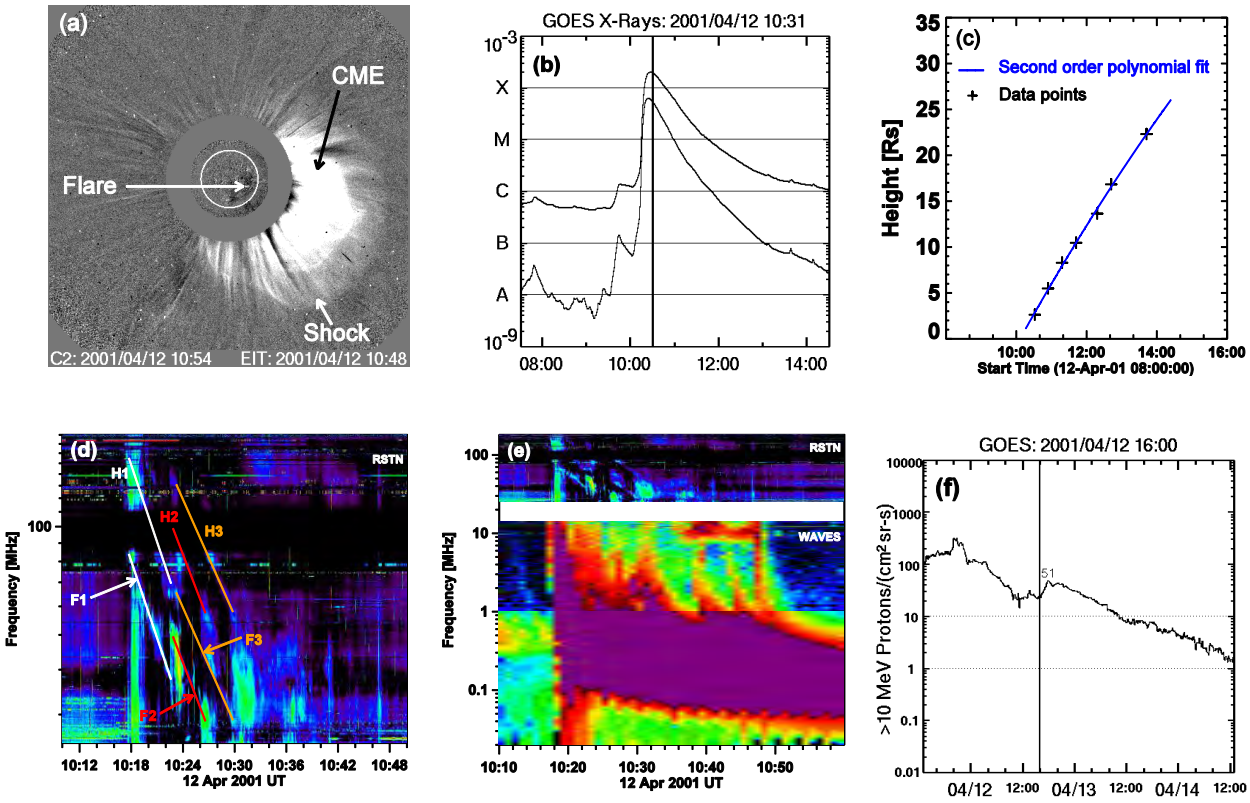

Figure 5.2. (a) A running difference image of a CME in LASCO/C2 FOV on 2001 April 12 at 10:54 UT superposed with a 195 Å EIT difference image showing the location of eruption on the Sun. The CME, the CME –driven shock and flare location are indicated by the arrows. The GOES soft X-ray intensity plot (b) shows an associated X-class flare peaking at ~ 10:31 UT. (c) The height-time measurement of the CME in the LASCO FOV. Second order polynomial is fitted to the data. (d) The RSTN dynamic spectrum showing the metric type II emissions. Three separate fundamental (F)-harmonic (H) emissions occurred which are indicated by white (F1-H1), red (F2-H2) and orange (F3-H3). Fundamental component of each burst is indicated by an arrow. (e) The combined RSTN and Wind/WAVEs dynamic spectra. (f) The proton intensity in the GOES > 10 MeV channel shows the associated SEP event which peaks at 51 pfu. The vertical line shows the start of the SEP profile due to the CME of interest.

5.2.2.1.1 Speed, Angular Width and Acceleration of DH CMEs

Here, we give the CME properties for the combined set of pure DH, m-DH and DH-km type II bursts. Six, nine and five of the pure DH, m-DH and DH-km type II associated CMEs, respectively have uncertain widths. Four of the pure DH type II bursts associated CMEs with uncertain width are partial-halo CMEs. One of the CMEs is very faint and the uncertainty of the last CME arises from the CME-CME interaction which makes it difficult to identify the exact edges of the CME. All the m-DH and DH-km type II burst associated CMEs with uncertain width are partial-halo CMEs. In all the partial halo cases, it is difficult to identify the exact edge of the CME. Fifteen, seven and four of the pure DH, m-DH and DH-km type II CMEs, respectively have uncertain accelerations mostly due to too few data points.

Considering all the 139 CMEs as a single set, we find that they have an average speed, non-halo width, acceleration and fraction of halo of 1078 km s^{-1}, 157°, –6.2 m s^{-2} and 44.6%, respectively. Gopalswamy et al. (2005a) obtained similar values of 1115 km s^{-1}, 139°, –7 m s^{-2} and 47.5%, respectively. Therefore, the CME data sets are comparable.

5.2.2.1.2 Kinematics of pure DH, m-DH and DH-km Type II Associated CMEs

Figure 5.3 (a-c), (d-f) and (g-i) summarize the speed, width and acceleration distributions of the 52 pure DH, 59 m-DH and 28 DH-km type II associated CMEs, respectively. The pure DH CMEs have average speed, non-halo width, acceleration and fraction of halos of 946 km s^{-1}, 142°, –4.1 m s^{-2} and 36.5%, respectively. The m-DH type II associated CMEs have the corresponding values of 1045 km s^{-1}, 157°, –14.1 m s^{-2} and 45.8%, respectively. The average values for the DH-km type II associated CMEs are 1395 km s^{-1}, 199°, 6.2 m s^{-2} and 57%, respectively. A pure DH halo-CME from the disk-center has the lowest speed, 291 km s^{-1}. The m-DH and DH-km have minimum speeds greater than 400 and 700 km s^{-1}, respectively. The maximum speeds of the pure DH, m-DH and DH-km type II associated CMEs are 2191, 2519 and 2402 km s^{-1}, respectively. Most of the CMEs are decelerating in the LASCO FOV and peak

at the bin with a central value of –15 m s^{-2} (see Figures 5.3 (c), (f) and (i)). The average and median values of the speed and non-halo width for each category are closer but large in case of the acceleration. These values indicate that the hierarchy is maintained even when we divided the DH type II bursts into three sub-categories. In terms of increasing speed and width, we see the following order: pure DH, m-DH, and DH-km type II bursts.

The average speed, non-halo width and full-halo fraction of CMEs associated with pure DH type II bursts are all less than those of CMEs associated with the m-DH and DH-km type II bursts. CMEs associated with DH-km type II bursts have the highest speeds and widths. The pure DH and m-DH type II associated CMEs are decelerating whereas the DH-km type II associated CMEs are accelerating in the LASCO FOV. However, the most probable bin has deceleration. The positive acceleration may be due to uncertain events. The few but positive values are likely to be correct because some CMEs continue to accelerate and form shocks beyond the metric domain. The m-DH type II associated CMEs have the highest deceleration.

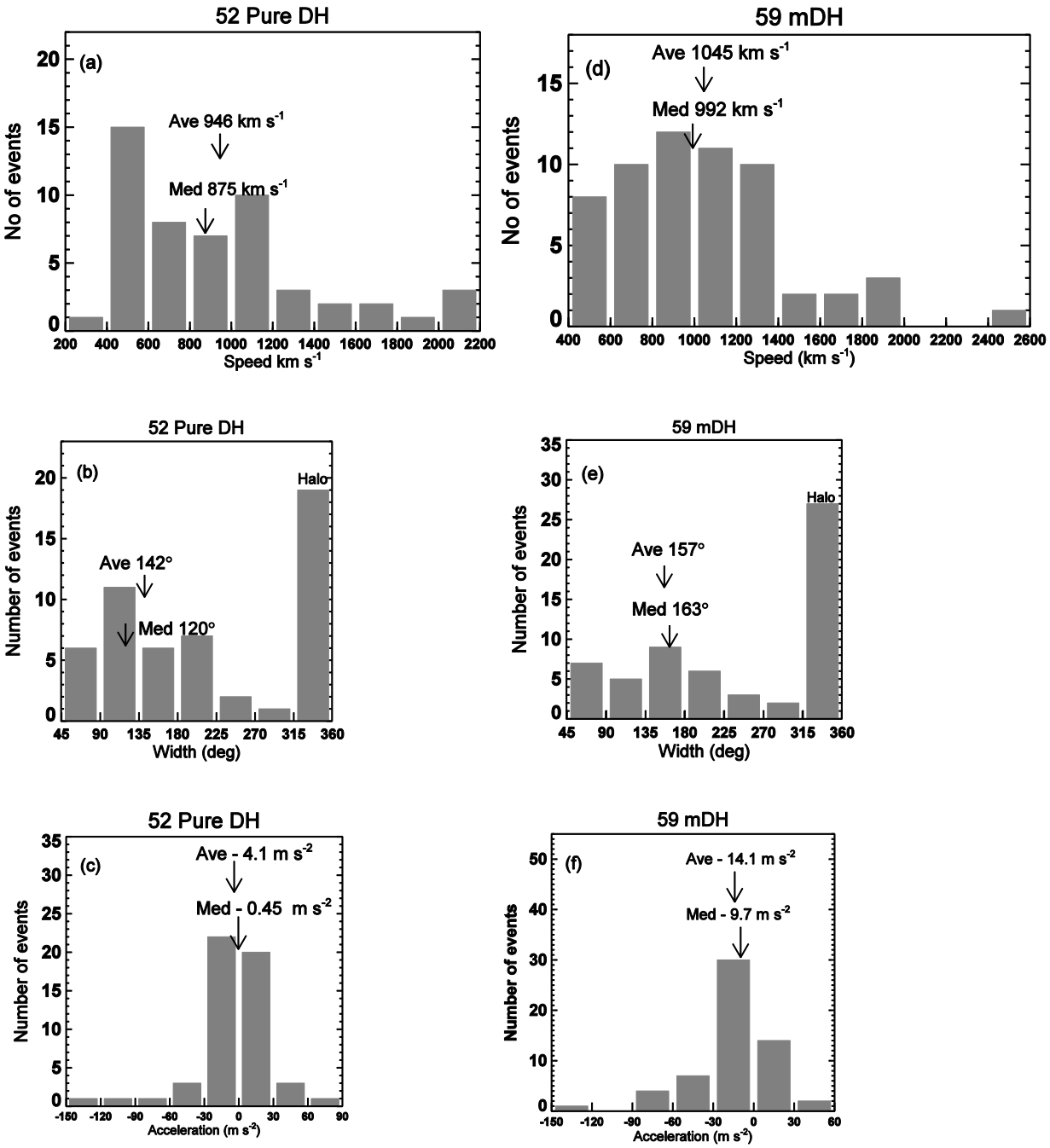

* Figure caption is in the next page (Figure 5.3).

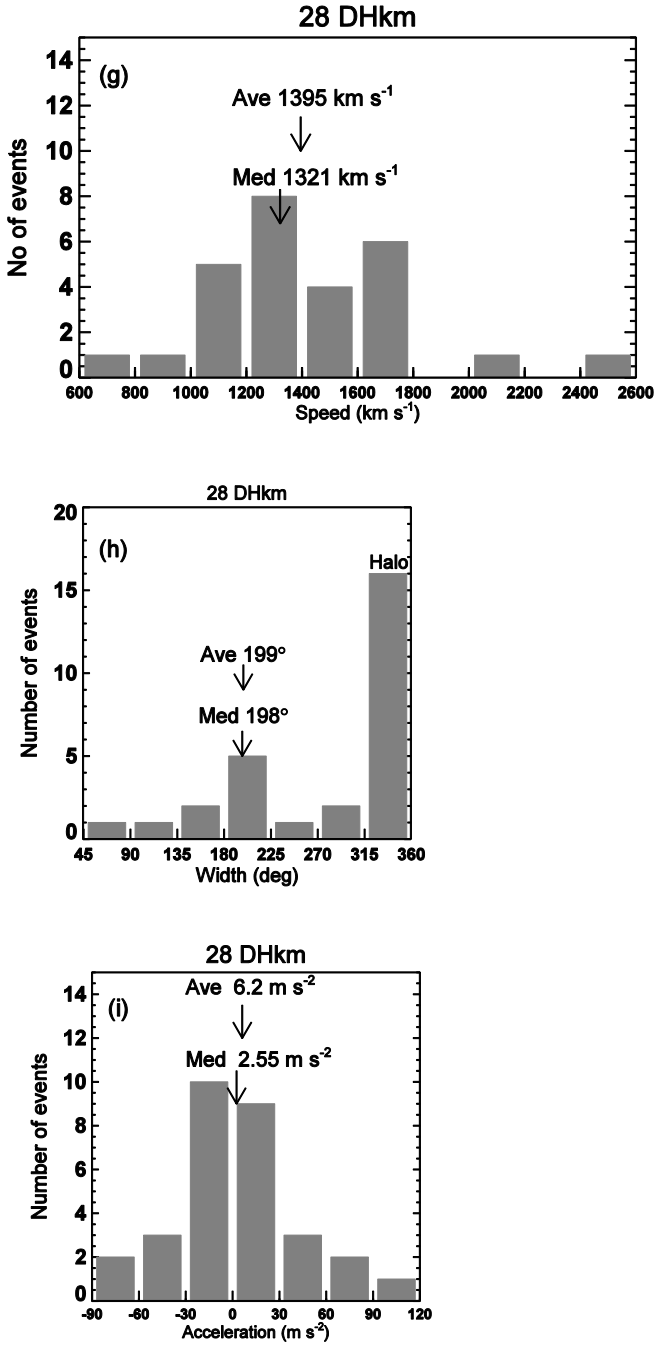

Figure 5.3. The speed, width, and acceleration distributions of CMEs associated with pure DH (a-c), m-DH (d-f) and DH-km (g-i) type II bursts. The average (Ave) and median (Med) values are shown by arrows and the right-most bin of the width distribution shows the number of halo CMEs.

5.2.2.2 Associated flares

Pure DH type II associated CMEs are associated with 21 C, 17 M and 5 X class flares. The rest do not have clear association with a flare. The m-DH type II associated CMEs have 1 B, 9 C, 27 M and 14 X class flares and the DH-km type II associated CMEs are associated with 5 C, 12 M and 5 X class flares. Six of the DH-km CMEs do not have flare information. More than 50% of the flare associated pure DH, m-DH and DH-km type II associated CMEs have M and higher class flares consistent with the result of Gopalswamy et al. (2010c). They found that the median size of flares associated with radio-loud CMEs is M4.7.

5.2.2.3 SEP Association

For the SEP event association, proton measurements in the GOES >10 MeV channel are used. The SEP association is categorized into major (> 10 pfu), minor (< 10 pfu), no SEP (about ≤ 0.1 pfu) and high-intensity background, HiB (if SEPs from previous events are present) events.

Out of the 52 pure DH type II associated CMEs, 24 (46.2%) do not have an SEP association. Seven (13.5%) of them are SEP-associated (4 of them are associated with a major SEP event). Twenty one (40.4%) events occur during an elevated background. On the other hand, out of the 59 m-DH type II associated CMEs, 30 (50.9%) do not have an SEP association. Nineteen (32.2%) have an SEP association and 11 of those (57.9%) are associated with a major SEP events. The rest occur during an enhanced background. Finally, 3 (10.7%) of the DH-km type II associated CMEs do not have SEP association, while 20 (71.4%) have an SEP association (16 or 80% with major SEP events). The rest occur during an enhanced background. The summary of the results is presented in Table 5.2.

5.2.2.4 Kinematics of SEP Associated CMEs

Figure 5.4 (a-c) and (d-f) show the speed, width and acceleration distributions of the 46 SEP-associated and 31 major SEP associated CMEs, respectively, in our data set. The average speed, non-halo width, acceleration and halo fraction for 46 SEP associated CMEs are 1163 km s^{-1}, 175°, –0.28 m s^{-2} and 52.2%, respectively. The corresponding average values for the 31 CMEs associated with a major SEP event are 1252 km s^{-1}, 190°, 5.3 m s^{-2} and 54.8%, respectively (see Figure 5.4 (d-f)). Compared to the 46 SEP-associated CMEs, the average speed, non-halo width and full halo fraction of the CMEs associated with a major SEP event have slightly larger values. Both results (of Figure 5.4) show that the average speed, non-halo width, and full halo fraction of SEP-associated CMEs are larger than those of the combined set of CMEs (Figure 5.3 (a) and (b), (d) and (e)) for the pure DH and m-DH type II associated CMEs but lower than those for the DH-km type II associated CMEs (Figure (g) and (h)). The average accelerations peak at the negative –15 m s^{-2} bin but the average value lies between those of the pure DH and m-DH type II associated CMEs.

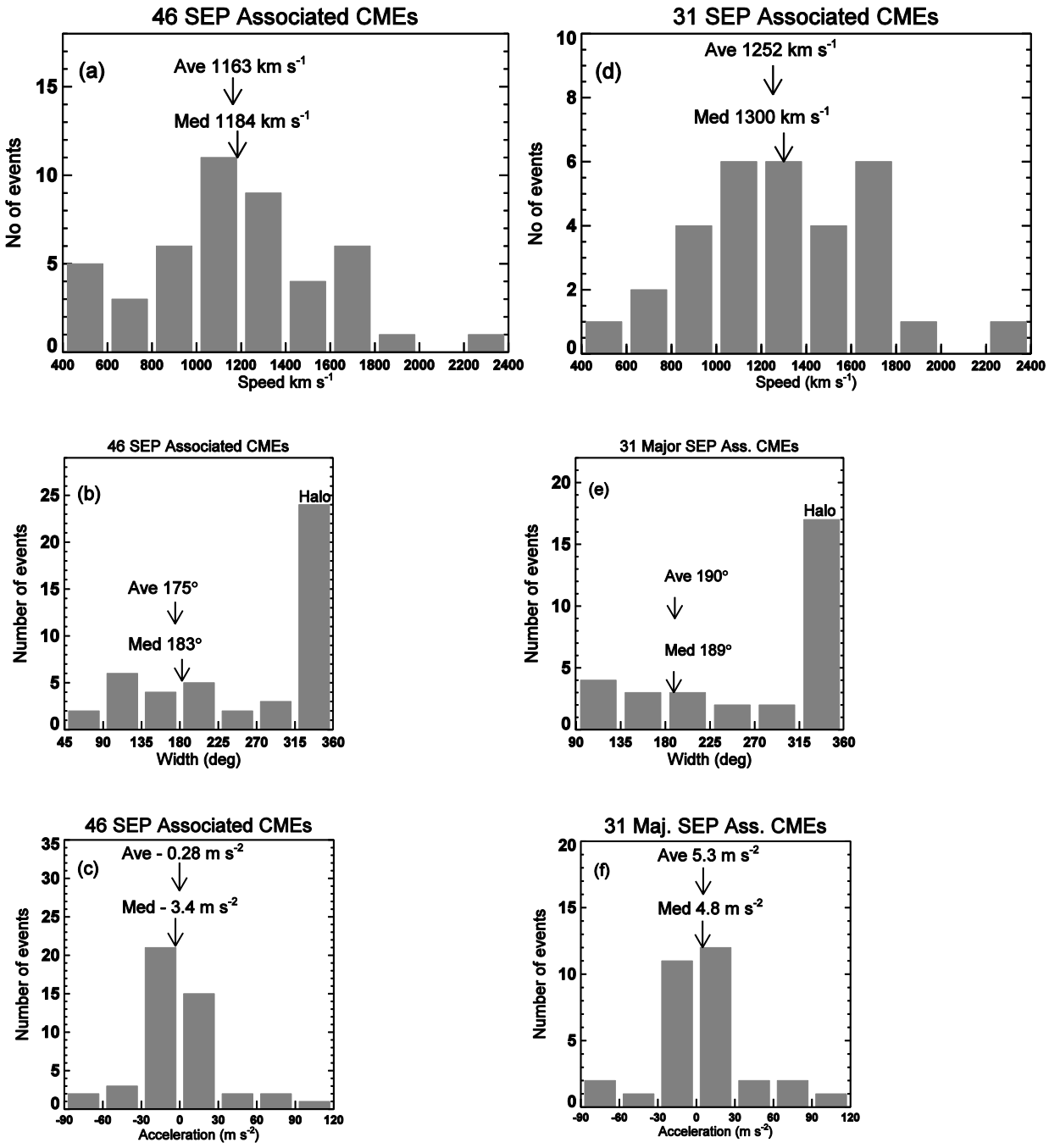

Figure 5.4. Forty six of the hundred and thirty nine CMEs are SEP associated. Thirty one of them are major SEP events. The speed, width and acceleration distributions of the 46 SEP (a-c) and 31 major SEP (d-f) associated CMEs. The median (Med) and average (Ave) values are indicated by arrows and the right-most bin of the width distribution shows the number of halo CMEs.

5.2.2.5 Distribution of Solar sources

The distribution of the solar source locations of the pure DH, m-DH and DH-km type II associated CMEs are presented in Figure 5.5 (a-c), respectively. Among the pure DH, m-DH and DH-km type II burst associated CMEs, 31 (61.5%), 39 (66.1%) and 14 (50%) of the CMEs lie within a CMD of 60°, respectively. Most of the CMEs are non-limb events.

We find that 50%, 60% and 66.7% of pure DH, m-DH and DH-km type II associated CMEs with no SEP events, respectively, are from the eastern hemisphere. On the other hand, 85.7%, 94.7% and 80% of the pure DH, m-DH and DH-km type II associated CMEs with SEP events are located in the western hemisphere. Finally, 42.9%, 50% and 80% of the pure DH, m-DH and DH-km type II associated CMEs with high density background are from the western hemisphere. Two and five of the m-DH and DH-km type II associated CMEs, respectively are backside events. The five SEP associated backside events of the DH-km type II associated CMEs are from the NW90b (NW quadrant behind the limb), NW90b, W90b (W behind the limb), NE90b (NE quadrant behind the limb) and unknown backside location with peak SEP intensities of 48, 28, 4, 92 and 493 pfu, respectively. Most of the SEP associated CMEs and a significant number of HiB CMEs have western source. Western CMEs are magnetically well-connected to the Earth due to the Parker spiral structure of the IP magnetic field and therefore particles have a direct access to Earth and GOES spacecraft.

Figure 5.5 (d) presents the source locations of the 46 SEP associated CMEs accompanied with pure DH, m-DH and DH-km type II bursts. Thirty one out of the forty six SEP associated events (67.4%) are major SEP events. Twenty seven out of the thirty one (87.1%) are western events. Three out of the twenty seven (11.1%) are backside events. It is clearly seen that most SEP associated CMEs are still from the western hemisphere.

Table 5.2 provides the summary of SEP association and source location information.

Table 5.2 SEP association and source location of the pure DH, m-DH and DH-km type II associated CMEs.

No	Type II Burst	SEP Association	No of events (%)	Eastern events (%)	Western events (%)
1	DH	No	24 (46.1)	12 (50)	12 (50)
		Yes	7 (13.5)	1 (14.3)	6 (85.7)
		HiB	21 (40.1)	12 (57.1)	9 (42.9)
2	m-DH	No	30 (50.9)	18 (60)	12 (40)
		Yes	19 (32.2)	1 (5.3)	18 (94.7)
		HiB	10 (16.9)	5 (50)	5 (50)
3	DH-km	No	3 (10.7)	2 (66.7)	1 (33.3)
		Yes	20 (71.4)	3 (15)	16 (80)
		HiB	5 (17.9)	1 (20)	4 (80)

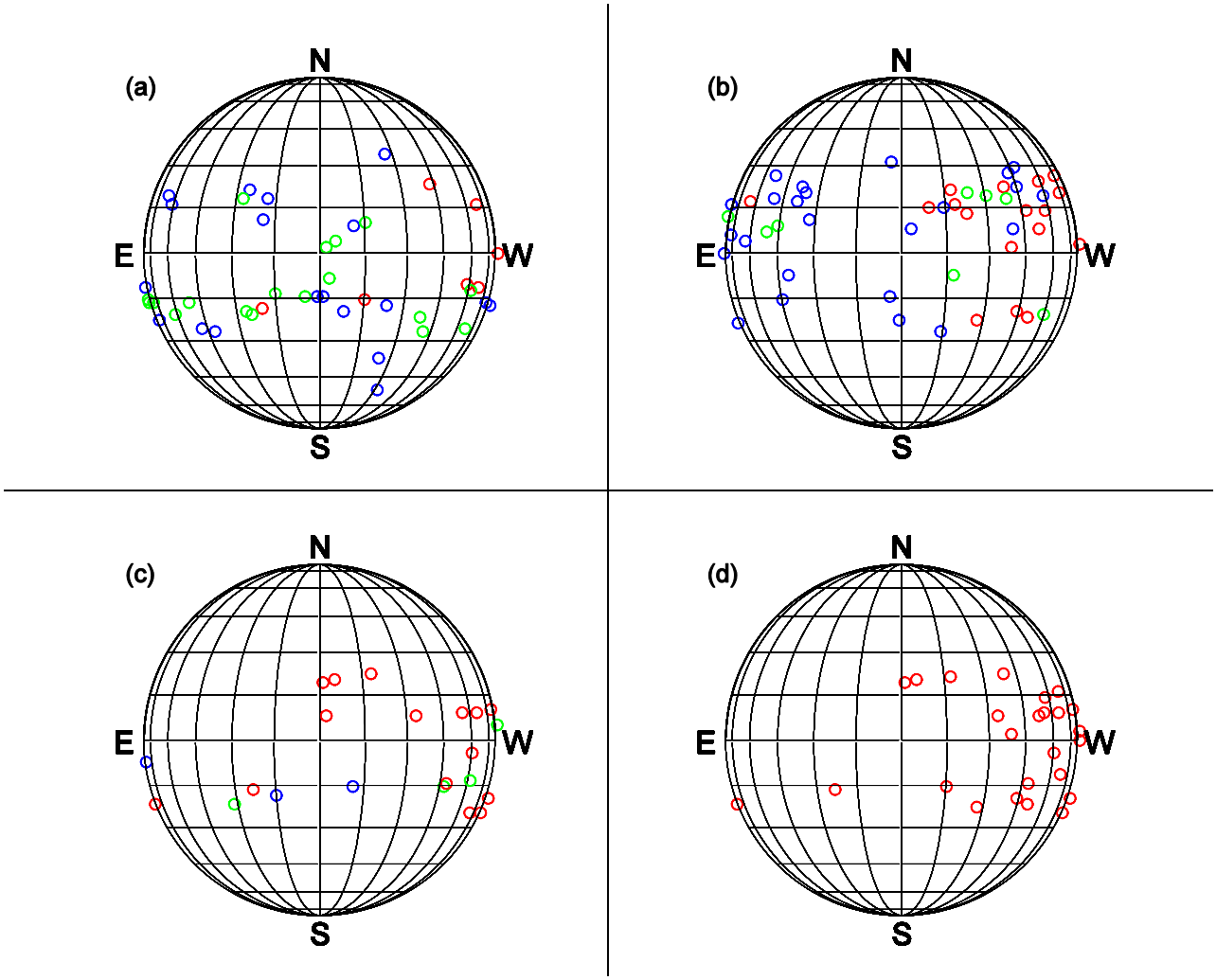

Figure 5.5. The solar source distributions of the pure DH (a), m-DH (b) and DH-km (c) type II associated CMEs. (d) The source locations of the 46 SEP associated CMEs of the combined set of pure DH, m-DH and DH-km type II associated CMEs, respectively. Blue symbols show source locations of CMEs that do not have SEP association, the red symbols are for those associated with SEPs and green symbols are for events with enhanced background. Solar North (N) is at the top and east (E) is to the left. South (S) and west (W) are also indicated.

5.3 Discussion

We studied the speed, width and acceleration distributions together with full-halo fraction, SEP association rate and solar source distributions of the CMEs associated with pure DH, m-DH and DH-km type II radio bursts. We found that the average speed of DH-km type II associated CMEs (1395 km s^{-1}) is the highest compared to the m-DH (1045 km s^{-1}) and pure DH type II associated CMEs (946 km s^{-1}). DH-km type II associated CMEs also span the widest wavelength range among these events. Compared to the previous result (1115 km s^{-1}) of Gopalswamy et al. (2005a) who studied the pure DH, m-DH and DH-km type II associated CMEs as a single group, our average speed of pure DH and m-DH type II associated CMEs is smaller because we exclude the high-speed DH-km type II associated CMEs. We found that the average speed of the DH-km type II associated CMEs is slightly lower than that of the m-km (1490 km s^{-1}) type II associated CMEs. This is consistent with the wider wavelength span of the m-km type II bursts compared to that of the DH-km type II bursts.

The DH-km type II associated CMEs have the highest acceleration (6.2 m s^{-2}) compared to the deceleration of m-DH (–14.1 m s^{-2}) and pure DH (– 4.1 m s^{-2}) type II associated CMEs in the LASCO FOV on average. The acceleration profile in Figure 5.3 (i) peaks at the negative bin centering at –15 m s^{-2}. The average and median values are also different. Therefore, the distribution is skewed and the positive average acceleration is due to the few but high positive acceleration values at the tail of the distribution. The positive acceleration is due the skewness of the distribution and large uncertainty in accelerations. In general, the DH-km type II burst associated CMEs start to drive a shock and accelerate electrons early in the inner corona (in the DH range) and continue driving the shock over large distances extending the type II emission into the km range. The peak of the acceleration distribution of the m-DH type II associated CMEs (51.7%) falls into the bin with –15 m s^{-2}. The next highest bin (24.1%) is the one centering at the acceleration 15 m s^{-2}. The high average deceleration is due to the few CMEs with high negative acceleration at the negative tail of the distribution, which is again seen in the

inequality in the average and median values. Pure DH type II associated CMEs have smaller deceleration (higher acceleration) than found in the previous study of DH type II associated CMEs (Gopalswamy et al. 2005a).

The average non-halo width and the full-halo fraction of DH-km type II associated CMEs (199° and 57%, respectively) are the largest among the three groups of CMEs we considered and those of the combined DH type II group of Gopalswamy et al. (2005a). Pure DH type II associated CMEs (142° and 36.5%, respectively) have the smallest and the m-DH type II associated CMEs (157^0 and 45.8%, respectively) have intermediate values. Consistent with the slightly slower average speeds, the full-halo fraction of the pure DH and m-DH type II associated CMEs are slightly smaller than the value found in the previous study of DH type II associated CMEs by Gopalswamy et al. (2005a). The average non-halo width of pure DH and m-DH type II associated CMEs is slightly higher than their DH type II associated CMEs (139°) but the peak of the width of the pure DH type II associated CMEs occurs at the bin with a central value of 113°. Hence, the difference in the results might be due to projection effects or the uncertainty in the CME width.

We found that DH-km type II associated CMEs are the fastest and widest. The average mass of DH-km type II associated CMEs (~ 1.3×10^{13} kg) is also the largest. The m-DH and pure type II associated CMEs have masses ~ 7.9×10^{12} and ~ 6.7×10^{12} kg, respectively. Combining with the fact that the DH-km type II associated CMEs have the highest average speed, and that the m-DH type II bursts are associated with the next fastest CMEs, we see that the kinetic energy of the CMEs organizes the type II burst wavelength range.

The DH-km type II associated CMEs have the highest SEP association rate (71.4%) compared to that of the m-DH (32.2%) and pure DH (13.5%) type II associated CMEs. High-speed CMEs have high probability of driving a shock and the shock accelerates particles, which can in turn produce the type II bursts and SEPs. We also confirmed that SEP association is the largest for the DH-km type II associated CMEs since they are the widest and have the highest speed

(Gopalswamy et al. 2001d). Compared to the Gopalswamy et al. (2008) 52% SEP association rate with DH type II associated CMEs, the SEP association rate of our pure DH and m-DH type II associated CMEs is lower, but higher in the case of DH-km type II associated CMEs. The SEP association rate of our DH-km type II associated CMEs is slightly smaller than the m-km type II CMEs (78%) of Gopalswamy et al. (2005a). Their speeds are also closer. We measured a smaller average speed of the 46 SEP associated CMEs of our combined set of the pure DH, m-DH and DH-km type II associated CMEs (1163 km s^{-1}) compared to 1448 km s^{-1} Gopalswamy et al. (2005a) because our data set does not include the corresponding high-speed m-km type II associated CMEs. The average speed of the 31 major SEP event producing CMEs (1252 km s^{-1}) is also slightly lower compared to Gopalswamy et al. (2005a). 54.4% of our SEP associated CMEs are found within 60° CMD, so the speed should be highly affected by the projection effects. The SEP associated CMEs are dominated by halo CMEs. Most of the SEP associated CMEs in the three DH type II burst associated CME population are associated with intense flares (M class and above).

Most of the DH-km (80%), m-DH (94.7%) and pure DH (85.7%) type II associated CMEs that have SEPs are located in the western hemisphere. CMEs originating from the western hemisphere are the most likely to produce SEPs, which reach at Earth along the Parker spiral (Reames 1999). The DH-km type II associated CMEs have the smallest percentage of western-hemisphere SEP event consistent with the high-speed and large width. A DH-km type II associated CME originating from the S07E80 (near east limb) speeding at 2053 km s^{-1} does not produce an observable SEP event at Earth. On the other hand, the second highest SEP event (2,560 pfu) associated with the DH-km type II burst is from the east (S16E23). It is a halo CME with a speed of 2402 km s^{-1}, which is the highest speed among the DH-km type II associated CMEs. The CME is associated with an X2.6 class flare. High-speed, wide and disk-center eastern CMEs can also produce SEPs, which can be detected by GOES, because the fast shock flank is magnetically well-connected to Earth. Shock flanks can also produce SEPs. Two minor SEP events of the pure DH and m-DH type II associated CMEs are also from the east.

More than 50% of the CMEs in each category of our CMEs are from the source regions lying within 60° CMD. The pure DH, m-DH and DH-km type II associated CMEs have high association rate with non-limb (close to the disk-center) CMEs consistent with Gopalswamy et al. (2008).

5.4 Conclusion

Gopalswamy et al. (2005a) found a hierarchical relationship between the wavelength range of type II radio bursts and CME kinetic energy. Under „DH Type II bursts" category they have combined pure DH, m-DH and DH-km bursts. In this work, we consider the pure DH, m-DH and DH-km type II associated CMEs separately. We find that DH-km type II associated CMEs are the fastest and widest CMEs with the highest mass on average. The m-DH type II associated CMEs have the next highest average speed and width. m-DH type II associated CMEs have slightly larger mass than the pure DH type II burst associated CMEs. Most of the CMEs of each population are decelerating. Our results are consistent with those of Gopalswamy et al. (2005a) in that the kinetic energy of the CMEs organizes the wavelength of the associated type II bursts. The SEP association rate goes along with the kinematic hierarchy. Most of the SEP associated CMEs originate from the western hemisphere of the Sun, because western sources are magnetically well-connected to GOES due to the Parker spiral structure of the IP magnetic field. SEP association rate increases with the speed of the CME. The more energetic the CME populations have the higher tendency in producing SEPs. SEP associated CMEs are dominated by halo population consistent with Gopalswamy et al. (2008) results.

Chapter 6

Conclusions and Future Work

In this chapter we summarize the conclusions drawn in the thesis. The continuity of the research is presented in short in the future work section.

6.1 Conclusions

The broad goal of this research is to investigate the spectral characteristics and origin of type II bursts, and the kinematics of the associated CMEs. The first part of the research focused on the location of the complex type II radio source relative to the direction of propagation of the 2012 January 19 CME (nose). The second part reported on the identification of a new spectral feature at frequencies below ~14 MHz. This diffuse feature in the dynamic spectrum is associated with a regular type II burst. It is slowly drifting type II (like chains of type I radio emissions), which extend to the interplanetary medium. We called this diffuse interplanetary radio emission or DIRE.

The third part focused on the statistics of the DIREs, and showed that these spectral features are not uncommon. The statistical results suggest that the interplanetary medium with extended shock fronts can support new types of particle acceleration. This takes us beyond the typical one CME – one type II burst scenario. As in the 2012 January 19 event, various combinations of nonthermal electron production, presence of ambient structures, and the presence of large-scale shocks can lead to distinct spectral features. Finally, the last topic dealt with how the CME kinetic energy organizes the wavelength range of type II bursts.

The following subsections are the conclusions drawn from each research component of the thesis.

6.1.1 A Study of the 2012 January 19 Complex Type II Radio Burst Using Wind, SOHO, and STEREO Observations

The complex type II burst on 2012 January 19 was observed by the WAVES on board the Wind spacecraft. White-light images of the associated CMEs are imaged by the LASCO coronagraphs on board the SOHO spacecraft and by the instruments suite of SECCHI on board the STEREO spacecraft. Clear primary CME (PCME) – preceding CME interactions are observed in the white-light images, especially in LASCO/C2, and the corresponding interaction signatures are observable also in the radio dynamic spectra. Comparing the shock and CME speeds, the density inferred from the type II bursts and from the pB images and over-plotting the PCME images onto the iso-density contour density extracted from the pB images, the radio source is determined to be above the flanks for the DH-km and near the nose for the DH bursts. Previously Liu et al (2013) have reported that the source region is the nose, but they overlook the details of the radio dynamic spectrum and the PCME-preceding CMEs interactions in their analysis.

The complexity involved additional spectral features such as a fundamental-harmonic pair of different drift rate compared to the main type II burst and the intensification of the main type II burst. The interactions of the primary and preceding CMEs are found to account for these spectral features. A lesson learned is that the PCME cannot be assumed to be propagating through a smooth corona and interplanetary medium. The inhomogeneities present in the ambient medium can lead to complex spectral features. The inhomogeneities can modify the emission frequency, change the shock strength, and affect the transit time of CMEs from the Sun to Earth. These considerations will help models to understand the deviations from the ideal situation, and hence provide measures of uncertainties in space weather predictions.

6.1.2 A Diffuse Interplanetary Radio Emission Observed by the Wind/WAVES Instrument

On 2001 September 27 a new spectral feature of interplanetary radio emission (DH-km), which we call a diffuse interplanetary radio emission, or DIRE, is observed by WAVES on board the Wind spacecraft. It is accompanied by a regular type II burst. The DIRE and the regular type II burst do not have harmonic relationship rather the DIRE occurs at a frequency of ~ 10 times that of the regular type II burst at the DIRE interval. Using similar analysis methods as in the study of the 2012 January 19 type II radio burst, we come to the conclusions that the western flank of the associated PCME which interacts with a streamer is the source of the DIRE.

This case highlights that there is much to discover by careful examination and analysis. This finding has important implications for the sites of particle acceleration on the shock surface and their escape into the heliosphere. The diffuse feature also requires nonthermal electrons, which may be of slightly lower energy than the ones causing regular type II bursts. This is because the radio emission is weak indicating lower intensity of Langmuir waves produced in the flank region by the lower energy electrons. The different morphology also points to the different magnetic field configuration into which the extended shock propagates.

6.1.3 A Statistical Study of Diffuse Interplanetary Radio Emission Associated with Type II Radio Bursts

The characteristics of 10 DIRE events associated with regular type II bursts detected by Wind/WAVES during 1996–2012 are analyzed. We found that the onset frequencies, onset heights and onset times of diffuse interplanetary radio emissions are higher than those of the associated regular type II burst at the DIRE interval. The drift rates of the DIREs are lower than

the regular type II, if the entire frequency is considered. DIREs are associated with wide and energetic CMEs.

6.1.4 Hierarchical Relationship of pure DH, m-DH and DH-km Type II Bursts Using the Kinematic Properties of the Associated CMEs

We splitted the „DH Type II bursts" category considered by Gopalswamy et al. (2005a) into the pure DH, m-DH and DH-km type II burst categories and found that the DH-km type II associated CMEs are more massive, faster and wider CMEs than the m-DH type II associated CMEs. Pure DH type II burst associated CMEs have the lowest values. For each population, the majority of the CMEs are decelerating. Our result strengthens the result found by Gopalswamy (2005a) that the kinetic energy of the CMEs organizes the wavelength of the associated type II bursts. The DH-km type II associated CMEs have the highest SEP association, followed by m-DH type II associated CMEs. The majority of the SEP associated CMEs originate from the western hemisphere due to the requirement that SEP acceleration region has a good magnetic connectivity to Earth. The speed of the CME is important for SEP production efficiency, because SEP association rate increases with the speed of the CME and wide CMEs with a very high-speed from the eastern hemisphere can also produce SEP events that can be detected at Earth.

The statistical study provided completeness to the previous studies that lumped together some spectral subregions. The statistics confirmed that CMEs are the most energetic and important players in Sun-Earth connection. The most energetic CMEs drive the strongest shocks that propagate far into the interplanetary medium. These are the shocks that are common to the two types of space weather responses, viz. particle acceleration and storm sudden commencement.

6.2 Future Work

The present investigation opened up a new avenue to make further progress in understanding the CME propagation in an inhomogeneous medium and the particle acceleration process in shocks. In particular, progress can be made by introducing large-scale density bumps or dips over limited radial extent representing streamers and preceding CMEs. One can then calculate the variability of the drift rate, which can be related to the variation in shock kinematics. Similarly, the variation in shock properties will be reflected in the intensity variation of the type II bursts.

Another line of investigation that can be pursued is the radio direction finding. The spinning nature of the Wind spacecraft can be effectively used to identify the centroid of the radio source and a size of the radio source (Reiner et al. 1997). Unfortunately, such a technique is possible only at frequencies below 1 MHz because of the sensitivity requirements. By careful searching, one may be able to identify some DIRE events below 1 MHz. Then it is possible to support the flank-emission idea for DIREs using the radio direction finding. An additional possibility is to use triangulation of the radio emission by combining STEREO and Wind radio observations. This needs a careful and patient examination of the radio data to identify spectral features that can be studied using multi spacecraft data.

References

Acuña, M. H., K. W. Ogilvie, D. N. Baker, S. A. Curtis, D. H. Fairfield, and W. H. Mish (1995), The Global Geospace Science Program and Its Investigations*, Space Sci. Rev.,* 71, 5.

Billings, D. E. (1966), A guide to the solar corona, Academic Press, New York.

Bougeret, J.-L. (1985), Observation of shock formation and evolution in the solar atmosphere, in *Collisionless shocks in the heliosphere: Reviews of current research*, p. 13, AGU, Washington, DC Solar Physics, 13.

Bougeret, J.-L. et al. (1995), Waves: The Radio and Plasma Wave Investigation on the Wind Spacecraft, *Space Sci. Rev.,* 71, 231.

Bougeret, J.-L. et al. (2008), S/WAVES: The Radio and Plasma Wave Investigation on the STEREO Mission, *Space Sci. Rev*., 136, 487.

Brueckner, G. E. et al. (1995), The Large Angle Spectroscopic Coronagraph (LASCO), *Sol. Phys*., 162, 357.

Burlaga, L., E. Sittler, F. Mariani, and R. Schwenn (1981), Magnetic loop behind an interplanetary shock: Voyager, Helios, and IMP 8 data, *J. Geophys. Res.*, 86, 6673.

Carley, E. P., H. Reid, N. Vilmer, and P. T. Gallagher (2015), Low frequency radio observations of bi-directional electron beams in the solar corona, *Astron. Astrophys.*, 581, 10.

Cairns, I. H., and D.B. Melrose (1985), A theory for the 2f(p) radiation upstream of the earth‟s bow shock, *J. Geophys. Res.*, 90, 6637.

Cairns, I. H. (1987a), Fundamental plasma emission involving ion sound waves, *J. Plasma Phys.*, 38, 169.

Cairns, I. H. (1987b), Second harmonic plasma emission involving ion sound waves, *J. Plasma Phys.,* 38, 179.

Cane, H. V., D. V. Reams, and T. T. von Rosenvinge (1988), The role of interplanetary shocks in the longitude distribution of solar energetic particles, *J. Geophys. Res.*, 93, 9555.

Cho, K.-S., J. Lee, Y.-J. Moon, M. Dryer, S.-C. Bong, Y.-H. Kim, and Y. D. Park (2007), A study of CME and type II shock kinematics based on coronal density measurement, *Astron. Astrophys.,* 461, 1121.

Cho, K.-S., N. Gopalswamy, R.-Y. Kwon, R.-S. Kim, and S. Yashiro (2013), A High-frequency Type II Solar Radio Burst Associated with the 2011 February 13 Coronal Mass Ejection, *Astrophys. J.,* 765, 9.

Cliver, E. W., S. W. Kahler, P. A. Shea, and D. F. Smart (1982), Injection of ~ 2 GeV, ~ 1 MeV and ~ 100 keV electrons in the solar cosmic ray flares, *Astrophys. J.*, 260, 362.

Cranmer, S. R. (2009), Coronal holes, *Living Reviews in Solar Physics*, 6 (vol).

Delaboudiniere, J.-P., et al. (1995), EIT:Extreme-Ultraviolet Imaging Telescope for the SOHO Mission, *Sol. Phys.,* 162, 291.

Dennis, B. R., and R. A. Schwartz (1989), Solar flares – The impulsive phase, *Sol. Phys.,* 121, 75.

Domingo, V., B. Fleck, and A. I. Poland (1995), The SOHO Mission: an overview, *Sol. Phys.,* 162, 1.

Dulk, G. A., Y. Leblanc, P. A. Robinson, J.-L. Bougeret, and R. P. Lin (1998), Electron beams and radio waves of solar type III bursts, *J. Geophys. Res.,* 103, 17223.

Emslie, A. G., B. R. Dennis, A. Y. Shih, P. C. Chamberlin, R. A. Mewaldt, C. S. Moore, G. H. Share, A. Vourlidas, and B. T. Welsch (2012), Global Energetics of Thirty-eight Large Solar Eruptive Events, *Astrophys. J.*, 759, 71.

Forbush, S. E. (1946), Three unusual cosmic ray increases possibly due to charged particles from the Sun, *Phys. Rev.,* 70, 771.

Foukal, P. (2004), Solar Astrophysics, (2nd edition), edited by Peter V. Foukal, p. 480, Wiley-VCH.

Klein, L. W., and L. Burlaga (1981), Interplanetary magnetic clouds at 1 AU, J. Geophys. Res., 87, 613.

Gabriel, A. H., and H. E. Mason (1982), Solar Physics, in *Applied Atomic Collision Physics*, vol. 1, edited by J. T. Schmelz, J. C. Brown, p. 345, New York and London Academic Press.

Gibson, S. E., Y. Fan, T. Török, B. Kliem, (2006), The Evolving Sigmoid: Evidence for Magnetic Flux Ropes in the Corona Before, During, and After CMEs. *Space Sci. Rev.*, 124:131-144.

Ginzburg, V. L., and V. V. Zhelezniakov (1958), On the Possible Mechanisms of Sporadic Solar Radio Emission (Radiation Isotropic Plasma), *Soviet Astronomy*, 2, 653.

Gold, T. (1962), Magnetic storms, *Space Sci. Rev*., 1, 100.

Goldstein, H. (1983), On the field configuration in magnetic clouds, in *JPL Solar Wind Five*, NASA Conf. Publ., 2280, 731.

Gopalswamy, N. (2000), Type II Solar Radio Bursts, in *Radio Astronomy at Long Wavelengths*, Geophys. Monogr. Ser., vol. 119, edited by R. G. Stone, K. W. Weiler, M. L. Goldstein and J.-L. Bougerot, p. 123, AGU, Washington, D. C.

Gopalswamy, N., S. Yashiro, G. Michalek, M. L. Kaiser, R. A. Howard, D. V. Reams, R. Leske, and T. von Rosenvinge (2002), Interacting Coronal Mass Ejections and Solar Energetic Particles, *Astrophys. J.*, 572, L103.

Gopalswamy, N. (2004a), Interplanetary Radio Bursts, in *Solar and Space Weather Radiophysics*, vol. 314, edited by D. E. Gary, and C. U. Keller, p. 305, Astrophysics and Space Library (Springer Science + Business Media).

Gopalswamy, N. (2004b), Recent advances in the long-wavelength radio physics of the sun, *Planet. Space Sci.,* 52, 1399.

Gopalswamy, N. (2006), Coronal Mass Ejections and Type II Radio Bursts, in *Solar Eruptions and Energetic Particles,* Geophys. Monogr. Ser., vol. 165, edited by N. Gopalswamy, R. Mewaldt, J. Torsti, p. 207, AGU, Washington, D. C.

Gopalswamy, N. (2009), Coronal mass ejections and space weather, in *Climate and Weather of the Sun-Earth System(CAWSES): Selected Papers from the 2007 Kyoto Symposium*, edited by T. Tsuda, R. Fujii, K. Shibata, and M. A. Geller, p. 77, TERRAPUB, Tokyo.

Gopalswamy, N. (2010), Coronal Mass Ejections: a Summary of Recent Results, in *Proc. 20th Slovac Nat. Solar Phys. Meeting*, edited by I. Dorotovic, p. 108, Slovak Central Observatory.

Gopalswamy, N. (2016), History and Development of Coronal Mass Ejections as a Key Player in Solar Terrestrial Relationship, *Geosci. Lett.,* in press, 2016arXiv160203665G7.

Gopalswamy, N., S. Yashiro, M. L. Kaiser, R. A. Howard, and J.-L. Bougeret (2001a), Radio Signatures of Coronal Mass Ejection Interaction: Coronal Mass Ejection Cannibalism?, *Astrophys. J.*, 548, L91.

Gopalswamy, N., A. Lara, S. Yashiro, M. L. Kaiser, and R. A. Howard (2001b), Predicating the 1-AU arrival times of coronal mass ejections, *J. Geophys. Res.*, 106, 29207.

Gopalswamy, N., A. Lara, M. L. Kaiser, and J.-L. Bougeret (2001c), Near-Sun and near-Earth manifestations of solar eruptions, *J. Geophys. Res.*, 106, 25261.

Gopalswamy, N., S. Yashiro, M. L. Kaiser, R. A. Howard, and J.-L. Bougeret (2001d), Characteristics of coronal mass ejections associated with long-wavelength type II radio burst, *J. Geophys. Res.*, 106, 29219.

Gopalswamy, N., M. Shimojo, W. Lu, S. Yashiro, K. Shibasaki, and R. A. Howard (2003), Prominence Eruptions and Coronal Mass Ejection: A statistical Study Using Microwave Observations, *Astrophys. J.*, 586, 562.

Gopalswamy, N., S. Yashiro, S. Akiyama, P. Mäkelä, H. Xie, M. L. Kaiser, R. A. Howard, and J. L. Bougeret (2008), Coronal mass ejections, type II radio bursts, and solar energetic particle events in the SOHO era, *Ann. Geophys.*, 26, 3033.

Gopalswamy, N., S. Yashiro, G. Michalek, G. Stenborg, A. Vourlidas, S. Freeland, and R. Howard (2009), The SOHO/LASCO CME Catalog, *Earth Moon Planets,* 104, 295.

Gopalswamy, N., and S, Yashiro (2011), The Strength and Radial Profile of the Coronal Magnetic Field from the standoff Distance of a Coronal Mass Ejection-driven Shock, *Astrophys. J. Lett.*, 736, L17.

Gopalswamy, N., P. Mäkelä, S. Yashiro, and J. M. Davila (2012), The Relationship Between the Expansion Speed and Radial Speed of CMEs Confined Using Quadrature Observations of the 2011 February 15 CME, *Sun and Geosphere*, 7, 7.

Gopalswamy, N., P. Makela, S. Yashiro, S. Akiyama, and M. J. Reiner (2016), Detection of Nonthermal Radio Emission from a Polar coronal mass ejection, under preparation.

Gopalswamy, N., E. Aguilar-Rodriguez, S. Yashiro, S. Nunes, M. L. Kaiser, and R. A. Howard (2005a), Type II bursts and energetic solar eruptions, *J. Geophys. Res.*, 110, A12S07.

Gopalswamy, N., L. Barbier, E. W. Cliver, G. Lu, S. P. Plunkett, and R. M. Skoug (2005b), Introduction to the special section: Violent Sun-Earth connection events of October-November 2003, *J. Geophys. Res., 110*, A09S00.

Gopalswamy, N., S. Yashiro, G. Michalek, H. Xie, P. Mäkelä, A. Vourlidas, and R. A. Howard (2010a), Catalog of Halo Coronal Mass Ejections from SOHO, *Sun and Geosphere.*, 5, 7.

Gopalswamy, N., S. Akiyama, S. Yashiro, and P. Mäkelä (2010b), Coronal Mass Ejection from Sunspot and Non-Sunspot Regions, in *Magnetic Coupling between the Interior and Atmosphere of the Sun, Proceedings of Astrophysics and Space Science*, edited by S.S. Hasan and R.J. Rutten, p. 289, Springer Berlin Heidelberg.

Gopalswamy, N., H. Xie, P. Mäkelä, S. Akiyama, S. Yashiro, M. L. Kaiser, R. A. Howard, J.-L. Bougeret, (2010c), Interplanetary Shocks Lacking Type II Radio Bursts, *Astrophys. J.*, 710, 1111.

Gopalswamy, N. (2011a) Coronal Mass Ejections and Solar Radio Emissions, in *Proc. 7th Planetary, Solar and Heliospheric Radio Emissions (PRE VII) Workshop*, edited by I. Graz, p. 325, Austrian Academy of Sciences Press.

Gopalswamy, N. (2011b), Coronal mass ejections and their heliospheric consequences, in *First Asia-Pacific Solar Physics Meeting ASI Conference Series*, vol. 2, edited by A. R. Choudhuri and D. Banerjee, p. 241, Bulletin Astro. Soc. India

Gopalswamy, N., P. Mäkelä, S. Akiyama, H. Xie, S. Yashiro, and A. A. Reinard (2013a), The Solar Connection of Enhanced Heavy Ion Charge States in the Interplanetary Medium: Implications for the Flux-Rope of CMEs, *Sol. Phys.*, 284, 17.

Gopalswamy, N., P. Mäkelä, H. Xie, S. Yashiro, (2013b) Testing the empirical shock arrival model using quadrature observations, *Space Weather*, 11, 661.

Gopalswamy, N., P. Mäkelä, S. Akiyama, S. Yashiro, H. Xie, N. Thakur, and S. W. Kahler (2015a), Large Solar Energetic Particle Events Associated with Filament Eruptions Outside of Active Regions, *Astrophys. J.,* 806, 15.

Gopalswamy, N., H. Xie, S. Akiyama, P. Mäkelä, S. Yashiro, and G. Michalek (2015b), The Peculiar Behavior of Halo Coronal Mass Ejections in Solar Cycle 24, *Astrophys. J. Lett.*, 804, 6.

Hansen, R. T., C. J. Garcia, R. J.-M. Grognard, and K. V. Sheridan (1971), A coronal disturbance observed simultaneously with a white-light corona-meter and the 80 MHz Culgoora radioheliograph, *Proc. Astron. Soc. Austr.*, 2, 57.

Harrison, R. A. (1995), The nature of solar flares associated with coronal mass ejection, *Astron. Astrophys.,* 340, 585.

Hudson, H. S., J.-L. Bougeret, and J. Burkepile (2006), Coronal Mass Ejections: Overview of Observations, *Space Sci. Rev.*, 213, 13.

Howard, R. A., D. J. Michels, N. R., Jr. Sheeley, and M. J. Koomen (1982), The observation of a coronal transient directed at earth, *Astrophys. J.,* 263, L101.

Howard, R. A. et al. (2008), Sun Earth Connection and Heliospheric Investigation (SECCHI), *Space Sci. Rev.,* 136, 67-115.

Uwamahoro, J. (2013), Analysis of source and predictability of geomagnetic storms: On the sources and predictability of geomagnetic storms, LAMBERT Academic Publishing, Germany.

Kahler, S. W., (1992), Solar flares and coronal mass ejections, *Annu. Rev. Astron. Astr.*, 30, 113.

Kaiser, M. L., T. A. Kucera, J. M. Davila, O. C.,St. Cyr, M. Guhakurta, E. Christian (2008), The STEREO Mission: An Introduction, *Space Sci. Rev.,* 136, 5.

Koutchmy, N. and M. Livishits (1992), Coronal Streamers, *Space Sci. Rev.,* 61, 393.

Leblanc, Y., G. A. Dulk, and J. Bougeret (1998), Tracing the Electron Density from the Corona to 1 AU, *Sol. Phys.,* 183, 165.

Lemen, J. R., et al. (2012), Atmospheric Imaging Array (AIA) ON THE Solar Dynamic Observatory (SDO), *Sol. Phys.,* 275, 17.

Lin, J., J. C. Raymond, and A. A. van Ballegooijen (2004), The role of Magnetic Reconnection in the Observable Features of Solar Eruptions, *Astrophys. J.*, 602, 422.

Liu, Y. D., J. G. Luhmann, N. Lugaz, C. Möstl, J. A. Davies, S. D., Bale, and R. P. Lin (2013), On Sun-to-Earth Propagation of Coronal Mass Ejections, *Astrophys. J.,* 769, 15.

Longcope, D. W., and C. Beveridge (2007), A Quantitative, Topological Model of Reconnection and Flux Rope Formation in a Two-Ribbon Flare*, Astrophys. J.,* 669, 621.

Low, B. C. (1994), Coronal mass ejections and magnetic helicity, in *Solar Dynamic Phenomena and Solar Wind Consequences, Proceedings of the 3rd SOHO Workshop*, edited by J. J. Hunt, p. 123, ESPA.

Low, B. C. (1997), The role of coronal mass ejections in solar activity, in *Coronal Mass Ejections Geophys. Mono. Ser.,* vol. 99, edited by N. Crooker, J. A. Joselyn, and J. Feynman, p. 39, AGU, Washington D. C.

MacQueen, R. M., J. A. Eddy, J. T. Gosling, E. Hildner, R. H. Munro, G. A., Jr. Newkirk, and A. I. Poland (1974), The Outer Solar Corona as Observed from Skylab: Preliminary Result, *Astrohys. J.,* 187, L85.

Magdalenić, J., C. Marqué, V. Krupar, M. Mierla, A. N. Zhukov, L. Rodriguez, M. Maksimović, and B. Cecconi (2014), Tracking CME-driven Shock Wave on 2012 March 5 and Radio Triangulation of Associated Radio Emission, *Astrophys. J.*, 791, 115.

Mann, G., H. Aurass, A. Klassen, C. Estel, and B. J. Thompson (1999), in *Proc. 8th SOHO Int. Workshop on, Plasma Dynamics and Diagnostics in the Solar Transition Region and Corona*, edited by J.-C. Vial and B. Kaldich-Schümann, p. 477, ESA Special Publications.

Melnik, V. N., H. O. Rucker, A. A. Konovalenko, V. V. Dorovskyy, E. P. Abranin, and A. Lecacheux (2011), Decameter Radio Emission of the Sun: Recent Observations, in *Proc. 7th Int. Workshop on Planetary, Solar and Heliospheric Radio Emissions (PRE VII) Workshop*, edited by I. Graz, p. 343, Austrian Academy of Sciences Press.

Mikic, Z., and M. Lee (2006), An introduction to theory and models of CMEs, shocks and solar energetic particles, *Space Sci. Rev.*, 123, 57.

Minnaert, M. (1930), On the continuous spectrum of the corona and its polarization. With 3 figures. (July 30, 1930), *Z. Astrophys.*, 1, 209.

Nelson, G. J., and D. B. Melrose (1985), Type II Bursts, in *Solar radiophysics: Studies of emission from the sun at metre wavelengths*, edited by D. J. MacLean, N. R. Labrum, p. 333, Cambridge University Press, Cambridge and New York.

Newkirk, G., Jr. (1967), Structure of the Solar Corona, *Annu. Rev. Astron. Astr.,* 5, 213.

Parker, E. N. (1957), Sweet‟s for Merging Magnetic Fields in Conducting Fluids, *J. Geophys Res.,* 62, 509.

Payne-Scott, R., D. E. Yabsley, and J. G. Bolton (1947), Relative Times of Arrival of Bursts of Solar Noise on Different Radio Frequencies, *Nature,* 160, 256.

Pesnell, W. D., B. J. Thompson, and P. C. Chamber (2012), The Solar Dynamics Observatory (SDO), *Sol. Phys.,* 275, 3.

Petrovay, K., and U. R. Christensen (2010), The Magnetic Sun: Reversals and Long-Term Variations, *Space Sci. Rev.,* 155, 371.

Prialnik, D. (2009), An introduction to the Theory of Stellar Structure and Evolution, Cambridge University Press.

Quémerais, E., and P. Lamy (2002), Two-dimensional electron density in the solar corona from inversion of white light images–Application to SOHO/LASCO-C2 observations, *Astron. Astrophys.,* 393, 295.

Reams, D. V., (1990), Acceleration energetic particles by shock waves from large solar flares, *Astrophys. J.,* 358, L63.

Reams, D. V. (1999), Particle acceleration at the Sun and the heliosphere, *Space Sci. Rev.,* 90, 413.

Reiner, M. J., M. L. Kaiser, J. Fainberg, and R. G. Stone (1998), A new method for studying remote type II radio emissions from coronal mass ejection-driven shocks, *J. Geophys. Res.,*103, 29651.

Reiner, M. J., M. L. Kaiser, J. Fainberg, J.-L. Bougeret, and R. G. Stone (1997), Remote Radio Tracking of Interplanetary CMEs, in *Correlated Phenomena at the Sun, in the Heliospheric and Geospace*, *31st ESLAB Symposium held 22-25 September, 1997, at ESTEC, Noordwijk, Netherlands*, edited by A. Wilson, p. 183, European Space Agency.

Saito, K., A. I. Poland, and R. H. Munro (1977), A study of the background corona near solar minimum, *Sol. Phys.*, 55, 121.

Sheeley, N. R., Jr., W. N. Hakala, and Y.-M. Wang (2000), Detection of coronal mass ejection associated shock waves in the outer corona, *J. Geophys. Res.*, 105, 5081.

Schuster, A. (1879), on the polarization of the Solar Corona, *Mon. Not. R. Astron. Soc.*, 40, 35.

Susino, R., A. Bemporad, and S. Mancuso (2015), Physical Conditions of Coronal Plasma at the time of a Shock Driven by a Coronal Mass Ejection, *Astrophys. J.*, 812, 119.

Tandberg-Hanssen, E. (1995), The nature of solar prominences, *Astrophysics and Space Science Library*, vol. 199, Dordrecht: Kluwer Academic Publishers.

Thernisien, A. F., and R. A. Howard (2006), Electron Density Modelling of a Streamer Using LASCO Data of 2004 January and February, *Astrophys. J.,* 642, 523.

Tousey, R. (1973), The Solar Corona. in *Space Research XIII*, vol. 2, edited by M. J. Rycroft and S. K. Runcorn, p. 713, AkademieVerlag, Berlin.

Van de Hulst, H. C. (1950), The electron density of the corona, *Bull. Astron. Inst. Netherlands*, 11, 135.

Veronig, A. M., and W. Polanec (2015), Magnetic Reconnection Rates and Energy Release in a Confined X-class Flare, *Sol. Phys.,* 290, 2923

Vourlidas, A., S. T. Wu, A. H. Wang, P. Subramanian, and R. A. Howard (2003), Direct Detection of a Coronal Mass Ejection-Associated Shock in Large Angle and Spectrometric Coronagraph Experiment White-Light Images, *Astrophys. J.,* 598, 1392.

Wülser, J.-P., et al. (2004), EUVI: the STEREO-SECCHI extreme ultraviolet imager, Telescopes and Instrumentation for Solar Astrophysics, in *Proceedings of the SPIE,* vol. 5171, edited by S. Finesc and M. A. Gummin, p. 111.

Wild, J. P., and L. L. McCready (1950), Observations of the Spectrum of High-Intensity Solar Radiation at Meter Wavelengths. The Apparatus and Spectral Types of Solar Burs Observed, *Austr. J. Sci. Res. A Phys. Sci.*, 3, 387.

Yashiro, S., N. Gopalswamy, G. Michalek, O. C. St. Cyr, S. P. Plunkett, N. B. Rich, and R. A. Howard (2004), A catalog of white light coronal mass ejections observed by the SOHO spacecraft, *J. Geophys. Res.,* 109, A07105.

Publications

1. Teklu, T., N. Gopalswamy, A. V. Gholap, P. Mäkelä, S. Yashiro, S. Akiyama, N. Thakur, and H. Xie (2016), A study case of the 2012 January 19 Complex Type II Radio Burst Using Wind, SOHO, and STEREO Observations, *Asia-pacific Radio Science Conference in Seoul,* in press, 2016arXiv1605.09644.

Presentations

1. SHINE Conference, June 2014, Telluride, Colorado, Teklu, T., N. Gopalswamy, A. V. Gholap, P. Mäkelä, S. Yashiro, S. Akiyama, N. Thakur, and H. Xie , "A study of the 2012 January 19 Complex Type II Radio Burst Using Wind, SOHO, and STEREO Observations" (Poster Presentation)
2. SHINE Conference, 2015, Stowe, Vermont, Teklu, T., N. Gopalswamy, A. V. Gholap, P. Mäkelä, S. Yashiro, S. Akiyama, and H. Xie, "Hierarchical relationship of DH, m-DH and DH-km type II bursts using the kinematic properties of the associated CMEs" (Poster Presentation).
3. AGUFALL Meeting 2015, San Francisco, California, Teklu, T., N. Gopalswamy, A. V. Gholap, P. Mäkelä, S. Yashiro, S. Akiyama, and H. Xie, "A Diffuse Interplanetary Radio Emission Observed by the Wind/WAVES Instrument" (Poster Presentation).
4. 8th Annual Sciences an Exploration Directorate New Year‟s Poster Party, January 2016, Goddard Space Flight Center (NASA), Teklu, T., N. Gopalswamy, A. V. Gholap, P. Mäkelä, S. Yashiro, S. Akiyama, and H. Xie, "A Diffuse Interplanetary Radio Emission Observed by the Wind/WAVES Instrument".
5. 8th Annual Sciences an Exploration Directorate New Year‟s Poster Party, January 2016, Goddard Space Flight Center (NASA), Teklu, T., N. Gopalswamy, A. V. Gholap, P. Mäkelä, S. Yashiro, S. Akiyama, and H. Xie, "Statistical Study on Diffuse Interplanetary Radio Emissions Associated with type II Bursts".

Certificate

Certified that the work incorporated in the thesis entitled "*New Insights into the Relation between Coronal Mass Ejections and Nonthermal Radio Emissions*", submitted by Tsega Berhane Teklu was carried out by the candidate, under my supervision. The work presented here or any part of it has not been included in any other thesis submitted previously for the award of any degree or diploma from any other University or institution.

Dr. Natchimuthuk Gopalswamy

Name of Advisor Signature Date

Prof. Ashok Vasudeo Gholap

Name of Advisor Signature Date

Declaration

I declare that this written submission represents my ideas in my own words and where others‟ ideas have been included; I have adequately cited and referenced the original sources. I also declare that I have adhered to all principles of academic honesty and integrity and have not misrepresented or fabricated or falsified any idea/data/fact/source in my submission. I understand that violation of the above will be cause for discrepancy action by the University and can also evoke penal action from the sources which have thus not been properly cited or from whom proper permission has not been taken when needed.

Tsega Berhane Teklu

Student Name Signature Date